LA-13958-T
Thesis


# A Numerical and Experimental Study of a Shock-Accelerated Heavy Gas Cylinder

Los Alamos
NATIONAL LABORATORY

This thesis was accepted by the Applied Mathematics and Statistics Department, State University of New York, Stony Brook, New York, in partial fulfillment of the requirements for the degree of Doctor of Philosophy. The text and illustrations are the independent work of the author and only the front matter has been edited by the IM-1 Writing and Editing Staff to conform with Department of Energy and Los Alamos National Laboratory publication policies.

LA-13958-T
Thesis
Issued: July 2002

# A Numerical and Experimental Study of a Shock-Accelerated Heavy Gas Cylinder

Cindy Anne Zoldi

Los Alamos
NATIONAL LABORATORY

Abstract of the Dissertation

A Numerical and Experimental Study of a Shock-Accelerated Heavy Gas Cylinder

by

Cindy Anne Zoldi
Doctor of Philosophy

in

Applied Mathematics and Statistics

State University of New York
at Stony Brook

2002

In this thesis we study the evolution of an $SF_6$ gas cylinder surrounded by air when accelerated by a planar Mach 1.2 shock wave. Vorticity generated by the interaction of the shock wave's pressure gradient with the density gradient at the air/$SF_6$ interface drives the evolution of the cylinder into a vortex pair.

This thesis contains two interrelated parts; the first part concerns the acquisition of experimental data and the second part concerns the use of this data to benchmark simulations of the experiment with the hydrodynamics

code RAGE. RAGE, an adaptive-mesh Eulerian code, has had previous success in simulating shocked interfaces.

Improved experimental diagnostics were used to acquire data, which allowed us to perform a more stringent test of the code's capabilities. From each shock tube experiment, we obtained one image of the experimental initial conditions and six images of the time evolution of the cylinder. Moreover, the implementation of Particle Image Velocimetry (PIV) also allowed us to determine the velocity field at the last experimental time. This thesis is the first code validation study of a shocked flow to use two-dimensional velocity field data for comparison.

Simulations incorporating the two-dimensional image of the experimental initial conditions led to good qualitative agreement with the experimental images. Comparing length measurements of the evolving cylinder and velocity vectors at the last experimental time led to quantitative differences, particularly between the measured and computed velocity magnitudes. The computational study carried out in this thesis showed that agreement between the measured and the computed velocities could be achieved by decreasing the peak $SF_6$ concentration and diffusing the air/$SF_6$ interface in the experimental initial conditions. These modifications are consistent with the observation that the $SF_6$ gas diffuses faster than the glycol droplets used to track the gas. Further experimental improvements, including a better characterization of the experimental initial conditions, are discussed.

This thesis demonstrates that quantitative measurements, in addition

to qualitative images, should be examined when comparing experimental data and computational results. The quantitative differences between the measured and the computed velocity magnitudes led to the conclusion that the experimental initial conditions were not well characterized.

*To my parents, who have been by my side throughout this journey*

# Table of Contents

# List of Figures

# List of Tables

# Acknowledgments

I am extremely grateful for the advise, support, and guidance of my dissertation advisor James Glimm. I thank him for giving me the opportunity to perform my thesis research at Los Alamos National Laboratory. I am also grateful for the support of David Sharp, who was willing to serve as my on-site thesis advisor at Los Alamos. He was always there for me when I needed him. I would like to thank Kathy Prestridge, Chris Tomkins, Mark Marr-Lyons, Paul Rightley, and Bob Benjamin for their help in the acquisition and analysis of the experimental data presented in this thesis. I would also like to thank James Kamm and Bill Rider for many insightful conversations. I also wish to acknowledge the members of my dissertation defense committee, especially John Grove and Bob Benjamin who agreed to make the trip to Stony Brook to serve on my committee.

The time I have spent at Los Alamos has been a test of my strength, perseverance, and dedication. Thanks to the constant support of friends and family I have succeeded despite the adversity encountered during this

journey. I would like to thank Kathy Prestridge for her friendship during some of the darkest times in my life. I will never forgot what she has done and continues to do for me. I would also like to thank Avneet Sood who taught me how to trust again. My outlook on life has greatly improved with him by my side.

Last, but not least, I would like to thank my parents and my brother for their undying love and support throughout the years. I couldn't have reached this point in my life without them.

# Chapter 1

# Introduction

An instability induced by a shock wave colliding with an interface between two materials of different density is a fundamental problem in fluid mechanics. This instability, known as the Richtmyer-Meshkov instability, is driven by baroclinic vorticity deposition, which causes perturbations on the interface to grow with time.

In this thesis, we examine the evolution of a heavy gas cylinder when accelerated by a Mach 1.2 shock wave using experimental and computational techniques. A qualitative comparison of the simulations and the experiments shows good visual agreement, but a quantitative comparison initially shows considerable disagreement between the measured and computed velocity magnitudes. Through computational and experimental analyses we determine that the observed quantitative disagreement is caused by an inaccurate representation of the experimental initial conditions. This thesis

demonstrates the importance of using quantitative measurements in addition to qualitative images to test a code's ability to accurately model nature. Note this thesis is the first code validation study of a shocked flow that uses two-dimensional velocity field data for comparison. We believe this is a major advance in code validation.

## 1.1 Motivation

This research is motivated by the verification and validation effort at Los Alamos National Laboratory, by improved computational and experimental capabilities, and by the scientific interest in understanding fluid instabilities. We present our view of the verification and validation process and then present the computational and experimental advancements, which have allowed for a more stringent test of our computational capability, as represented by the RAGE code.

### 1.1.1 Verification and Validation

Our goal here is to understand the behavior of fluid instabilities as they occur in nature. This is accomplished by performing successive approximations of nature using theoretical, computational, and experimental techniques. Figure 1.1 shows the model we have chosen to follow in our attempt to understand the nature of fluid instabilities. The process is composed of four elements: nature, theory, computation, and experiment. Note

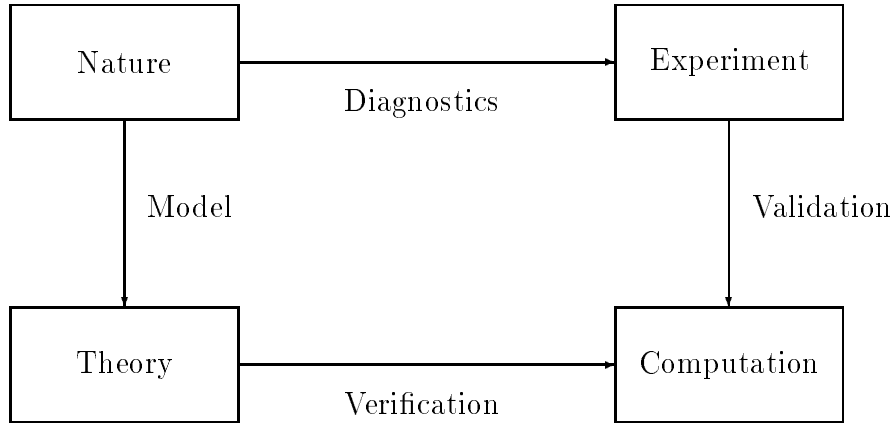


Figure 1.1: A personal view of scientific modeling

the locations of verification and validation.

The process begins by modelling the physics of nature in terms of mathematical equations. The Euler equations are taken as the model of fluid flow in this study. These equations can not be solved analytically for most cases of interest, including the experimental flow configuration examined in this thesis. Hence we develop computer codes that solve these equations numerically, allowing one to obtain an approximate space-time solution. The process of verification is necessary at this stage to confirm that the intended equations are implemented properly and solved accurately by the code. It is important to notice that there is no direct line between nature and computation in Figure 1.1, although the goal is to use codes to describe nature. We note that mathematical equations approximate nature and computer codes are only a further approximation.

Another way to approximate nature is by performing experiments. Experiments exhibit the physics we are interested in, but the information obtained is limited by diagnostics. For example in our experiment, CCD (charge-coupled device) cameras are used to obtain discrete snapshots of the evolving cylinder as opposed to a continuous observation. Even with this limitation, experimental results have proven to be extremely useful in developing intuition about the evolution of fluid instabilities. Experiments have also helped to verify the algorithms and to validate the physics models implemented in a code [2]. Comparison with experimental data is essential to determine how well a simulation is modeling nature.

**Viewpoints**

As shown in Figure 1.1, verification and validation are both necessary to evaluate the accuracy of a code. Note that verification and validation are performed on models, which are constructed using approximations and assumptions. It is important to recognize all approximations made in a code to prevent erroneous conclusions from being drawn based on the verification and validation process.

The conclusions in this thesis are based on knowing and understanding the approximations used in the code. In our study we approximate nature by assuming that all aspects of fluid flow can be modeled by the conservation of mass, momentum, and energy. Further we simplify these equations by assuming that heat conduction and viscosity can be neglected; the resulting expressions are the Euler equations. These equations are implemented numerically using a finite difference scheme, which is only accurate up to a certain order. For example, the RAGE code used in this study employs a directionally-split second-order Godunov scheme to solve the Euler equations.

It is important to realize that agreement with analytical or experimental results does not automatically imply agreement with other problems outside the time-space realm of these results. For example, previous validation of RAGE using the "gas curtain" experiments led to good qualitative agreement with experiment data [2]. Our research shows that the computational and experimental advances made after this validation effort expose differences

between the experiment and the simulation. These differences could not be realized in the previous code validation effort because of computational and experimental limitations.

We must keep in mind that computations are only a tool to approximate reality. All approximations in a computer code should be recognized and no computational results should be taken as truth. We will never be able to develop the perfect code, but we should always use experimental data, when available, to help validate and improve computer codes. Continuous improvements in codes, theories, and experiments will allow our computations to asymptotically approach reality.

### 1.1.2 Computational and Experimental Advances

With advances in experimental and computational capabilities, we can now do a more thorough job of code validation in some cases. Previous code validation has been performed for the RAGE code using shock tube experiments examining a "curtain" perturbation [2]. Since this effort,the RAGE code has been transformed from a Fortran 77 vector code into a Fortran 90 parallel code. Also as more powerful computer resources became available, time and memory were no longer as severe a constraint as they once were. These improvements now allow us to perform higher resolution simulations with larger computational domain, which enables us to obtain a better characterization the flow.

The shock tube used in this study has also seen many improvements.

The imaging system has been upgraded from direct Rayleigh scattering, which directly measures the $SF_6$ gas concentration to a system that images the $SF_6$ gas by illuminating tracer particles added the flow. This system allows us to obtain multiple high resolution images. A total of seven experimental images, one of the initial conditions and six of the time evolution of the cylinder, is now possible compared to the one dynamic image previously obtained. Particle Image Velocimetry has also been implemented, allowing us to determine velocity vectors of the dynamic image at the last experimental time. This is a major advance in quantitative data available for code validation. The improved diagnostics provide a more complete picture of the experimental flow. These computational and experimental advances have prompted us to reinvestigate the accuracy of the RAGE code, since a more stringent test can now be performed for Richtmyer-Meshkov problems.

## 1.2 Rayleigh-Taylor Instability

The Rayleigh-Taylor instability is named for the independent efforts of Lord Rayleigh [43] and G. I. Taylor [55]. The Rayleigh-Taylor instability occurs when a light fluid pushes a heavy fluid causing perturbations on the light-heavy interface to grow. An overview of this instability can be found in [50]. We note that the converse case of a heavy fluid pushing a light fluid is stable. The effects of the Rayleigh-Taylor instability on the development of supernovas and on the implosion of an Inertial Confinement Fusion pellet

is discussed in Section 1.4.

Extensive research has been performed to quantify the growth of the mixing zone by approximating the penetration of the bubbles into the heavy fluid and the spikes into the light fluid. Initially for small amplitude perturbations, the growth is exponential with time. Then as the perturbations become larger, the growth becomes nonlinear with the bubble and spike front growing as:

$$h_s = \alpha_s A g t^2 \tag{1.1}$$

$$h_b = \alpha_b A g t^2 \tag{1.2}$$

where g is the acceleration of gravity, $\alpha_s$ and $\alpha_b$ are constants, and A is the Atwood number defined by:

$$A = \frac{\rho_1 - \rho_2}{\rho_1 + \rho_2}. \tag{1.3}$$

The subscripts $s$ and $b$ refer to the spike and bubble, respectively. Considerable research has been performed to determine the value of the constant $\alpha_b$. The value determined numerically, theoretically, and experimentally lie in the range between 0.02 and 0.07. Research continues to be performed to try to determine one value for the constant $\alpha_b$.

## 1.3 Richtmyer-Meshkov Instability

The focus of this thesis is on the shock induced fluid instability known as the Richtmyer-Meshkov instability. The Richtmyer-Meshkov instability is

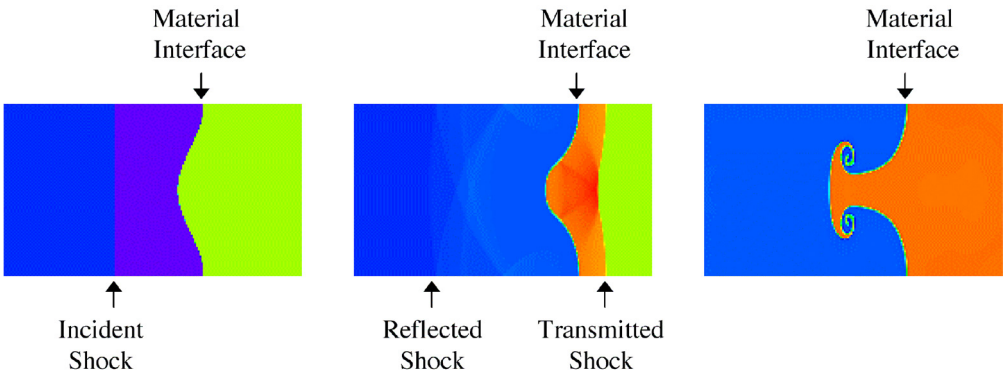


Figure 1.2: Richtmyer-Meshkov Instability for a light to heavy transition

named for the combined efforts of Richtmyer [45] and Meshkov [27].

Richtmyer is responsible for predicting the instability and deriving two models to estimate the growth of perturbations on the interface after shock passage. The first model, also called the impulsive model, was derived by examining the theory of the Rayleigh-Taylor instability and approximating the shock wave as an impulsive acceleration. Richtmyer also derived a linear theory for the case of a shock moving from a light material into a heavy material by linearizing the Euler equations and assuming incompressible flow.

Meshkov experimentally observed the phenomena predicted by Richtmyer. He also considered the complementary case of a shock moving from a heavy material into a light material and found that this configuration was also unstable. This experiment demonstrated that the Richtmyer-Meshkov instability occurs for both signs of the density gradient, unlike the Rayleigh-Taylor instability.

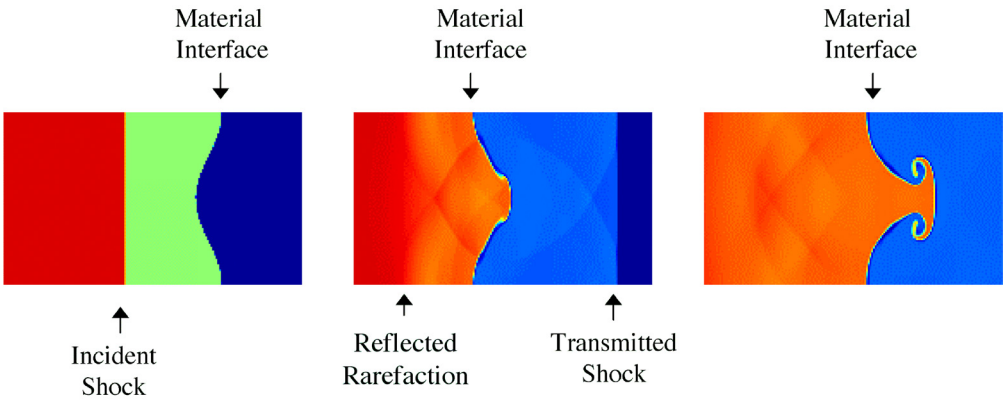


Figure 1.3: Richtmyer-Meshkov Instability for a heavy to light transition

Figures 1.2 and 1.3 illustrate the interaction of a shock wave with a perturbed interface between two materials of different densities. For the majority of real gases, a light to heavy transition produces a reflected shock at the material interface, and a heavy to light transition produces a reflected rarefaction at the material interface [59]. The determination of the type of reflected wave is made by analyzing the incident shock strength and the acoustic impedance of the wave.

In Figure 1.2, we consider the case of a shock moving from a low density material into a high density material. Blue corresponds to the shocked light material, purple to the unshocked light material, green to the the unshocked heavy material, and orange to the shocked heavy material. The incident shock is moving from left to right in the figure. When the incident shock hits the interface between the two materials, a transmitted shock and a

reflected shock are produced at the interface. The shock/interface interaction also deposits vorticity on the interface due to a misalignment between the pressure and density gradients. The deposited vorticity causes perturbations on the interface to grow with time.

Figure 1.3 shows the interface evolution for the case of a shock moving from a high density material into a lower density material. Red corresponds to the shocked heavy material, green to the unshocked heavy material, blue to the unshocked light material, and orange to the shocked light material. Again the shock is moving from left to right in the figure. At the material interface, the incident shock bifurcates into a transmitted shock and a reflected rarefaction wave. Phase inversion of the interface occurs, since the shock wave travels faster in the lighter material. The interface again grows with time due to the deposition of vorticity. The phase inversion and perturbation growth is shown in Figure 1.3.

Theories have been developed to quantify the interface growth as a function of time. Richtmyer derived the impulsive model and the linear theory to estimate the perturbation growth [45]. The linear theory derived by Richtmyer only considered the case of a reflected shock resulting from a light to heavy transition. Yang *et al.* [59] developed a small amplitude theory, which includes the case of a reflected rarefaction resulting from a shock moving from a heavy material into a light material. The small amplitude theory was derived by considering the one-dimensional Riemann problem for a shock-interface configuration and then linearizing the Euler equations

around the solution of this Riemann problem.

A nonlinear theory derived by Zhang and Sohn [61] is based on the observation that the flow is approximately linear and compressible at early time, and nonlinear and incompressible at late time. Zhang and Sohn constructed series expansions for the growth rate of the interface perturbations and applied Pade approximations to extend the range of validity of these expansions. The linear compressible solution valid at early time was matched with the nonlinear incompressible solution valid at late times to obtain the composite nonlinear theory valid for all times. The growth rate of the interface perturbations given by this nonlinear theory is:

$$\frac{da}{dt} = \frac{\nu_{linear}}{1 + \nu_{linear} k^2 t + max(0, a_0{}^2 k^2 - A^2 + 0.5)\nu_{linear}^2 k^2 t^2} \qquad (1.4)$$

where $\nu_{linear}$ is the growth rate given by linear theory, k is the wavenumber, and A is the Atwood number. This model has been compared with experimental data and numerical simulations of the single-mode Richtmyer-Meshkov instability and has showed good agreement for the growth rate for both early and late times.

## 1.4 Applications

The Rayleigh-Taylor instability and the Richtmyer-Meshkov instability have been studied extensively. It has been shown that these instabilities may be responsible for the degraded performance of a Inertial Confinement Fusion (ICF) pellet, and may also effect the evolution of a supernova.

### 1.4.1 Inertial Confinement Fusion

Inertial confinement fusion (ICF) is a process that is intended to create large amounts of energy by imploding a spherical pellet containing thermonuclear fuel. An ICF pellet is composed of a core of deuterium and tritium gas surrounded by a dense ablative shell [29]. There are two different methods that can be used to drive the implosion of the pellet: direct drive and indirect drive. Direct drive uses laser beams to heat the surface of the spherical pellet. Indirect drive uses x-rays instead of laser beams to drive the implosion of the pellet. The heating of the outer shell causes the shell to ablate and in turn cause a rapid increase in its volume. The resulting pressure gradient creates a shock wave that causes the remainder of the pellet to move inward toward its center. This inward motion heats and compresses the deuterium-tritium (DT) fuel in the center of the pellet. DT fusions occurs when the temperature and density are high enough, resulting in the production of large amounts of energy.

Richtmyer-Meshkov instability and Rayleigh-Taylor instability can degrade the performance of the ICF pellet. The Richtmyer-Meshkov instability is induced by the inward moving shock wave and the Rayleigh-Taylor instability is induced by the large pressure and density gradients between the DT fuel and the outer shell, when imperfections in the target fabrication and/or non-uniform laser penetration are present. The nonlinear evolution of the instabilities can cause the dense outer shell to crack allowing the shell and the DT fuel to mix. This mixing will reduce the compression of the DT

fuel and also decrease the DT temperature. If the temperature is too low, DT fusion will not occur, thus rendering the pellet inoperable. Therefore efforts are made to minimize the effect of the Richtmyer-Meshkov and the Rayleigh-Taylor instabilities.

### 1.4.2 Type II Supernovas

The explosion of a dying star produces a strong shock wave, which propagates outward from the core of the star [26] [32]. The "death" of a star results when its fuel is depleted. Without fuel, gravity pushes the star inward, increasing the star's temperature. A high enough temperature causes fusion to occur between hydrogen atoms, producing helium and energy. Fusion continues producing denser layers in the star. The layers in decreasing radius are: hydrogen, helium, carbon, oxygen, silicon, and iron. When iron is formed, further fusion ceases. Gravity then compresses the star further inward, making the star's core very dense. The high temperature and the high density of the core causes the collapse of the star. This collapse creates an outwardly expanding shock wave that races through the layers of the star, tearing the star apart.

Finger-like protrusions observed in supernova remnants are believed to be caused by hydrodynamical instabilities [8, 24, 25, 54] . Kane *et al.* have examined the effects of both the Richtmyer-Meshkov and the Rayleigh-Taylor instability on the supernova remnant formation [25]. It was computationally observed that any perturbations between the layers of the star will grow

due to the Richtmyer-Meshkov instability, which is produced by the outwardly moving shock and also by the inwardly moving reflected shock. It is believed that the Rayleigh-Taylor instability, produced by the light outer layers pushing on the heavy inner layers, acts to further increase the perturbation growth, creating fingers in the supernova remnant. Some researchers believe that the fingers are due to an asymmetric explosion [8] or fragmentation of the dense shell [54] caused by early-time Rayleigh-Taylor instability growth. Research continues to try to understand how fingers in supernova remnants are actually formed.

## 1.5 Thesis Overview

This thesis describes a numerical and experimental study of a shock-accelerated $SF_6$ gas cylinder performed at Los Alamos National Laboratory. This work is motivated by code validation efforts that must include comparisons with experimental data. This thesis will show that the shock-accelerated cylinder is a valuable test bed for validation. We achieve good visual agreement between the experiment and simulation, but a quantitative comparison initially shows considerable disagreement. Further computational and experimental analyses lead to the conclusion that the experimental initial conditions are not well characterized.

In Chapter 2, we present previous research relevant to our study of a shock-accelerated heavy gas cylinder. The shock tube used in the exper-

iments is discussed in Chapter 3. Chapter 4 contains an overview of the RAGE code used for the simulations, and Chapter 5 discusses the computational setup of the simulation. Chapter 6 examines the evolution of the shock-accelerated heavy gas cylinder and presents theoretical estimates for the amount of circulation after shock passage. In Chapter 7, we qualitatively and quantitatively compare the simulation results and the experimental data. We present a computational study examining variations in the initial conditions and new experimental images of the initial $SF_6$ gas cylinder, which lead us conclude that the experimental initial conditions are not well characterized. We conclude with Chapter 8, which summarizes our results.

# Chapter 2

# Previous Research

Since the pioneering efforts of Richtmyer [45] and Meshkov [27], extensive research has been performed to try to understand the dynamics of the Richtmyer-Meshkov instability. We review previous theoretical, experimental, and numerical efforts relevant to the subject of this thesis. We divide these research efforts into four areas: 1) analysis of a shock-accelerated heavy gas cylinder, 2) evolution of the Los Alamos gas shock tube, 3) RAGE code validation efforts, and 4) velocity measurements of a shock-accelerated flow.

## 2.1 Analysis of a Shock-Accelerated Heavy Gas Cylinder

There have been previous experiments and simulations performed that explore the dynamics of a shock-accelerated heavy gas cylinder. These stud-

ies are discussed in chronological order in this section.

### 2.1.1 Rudinger and Somers

In 1960 Rudinger and Somers experimentally and theoretically studied the behavior of spherical and cylindrical gas bubbles in accelerated flow [48]. The experiments were performed using a gas shock tube, and the pressure gradient between the test section and the driver section was varied to create the desired shock strength, which varied between Mach 1.12 and Mach 1.28. The interaction of the shock wave with three different density bubbles-hydrogen (H), helium (He), and Sulfur-hexafluoride ($SF_6$)-surrounded by air, were examined and imaged using a Schlieren system. The bubbles were created using a fine jet, which was discharged horizontally across the shock tube. The displacement of the bubble and the surrounding gas were measured after shock passage. It was experimentally observed that for weak shock speeds, the light gas (H or He) bubble had a larger displacement than the surrounding air, and in contrast the heavy gas ($SF_6$) bubble had a smaller displacement than the surrounding air. This fact is due to the density gradient between the ambient air and the gas bubble.

Rudinger and Somers also derived an expression relating the bubble velocity to the surrounding gas velocity. The interaction with the shock wave initially accelerates the bubble to a velocity $u_p$. At late-time the bubble velocity decreases to a velocity $u_b$, which occurs when the bubble absorbs energy from its initial acceleration and transforms into a vortex. In deriving

the expression, Rudinger and Somers assumed that the cylindrical bubble evolves into a vortex pair after shock passage. For a cylindrical bubble, the expressions for the velocity ratio of the initial bubble velocity $u_p$ and the final bubble velocity $u_b$ to the velocity of the surrounding gas $u_g$ are:

$$\frac{u_p}{u_g} = \frac{2}{\sigma + 1} \tag{2.1}$$

$$\frac{u_b}{u_g} = \left(1 + 0.203\frac{1-\sigma}{1+\sigma}\right) \tag{2.2}$$

where:

$$\sigma = \frac{\rho_{bubble}}{\rho_{gas}} \tag{2.3}$$

These expressions are dependent on the density ratio of the bubble and the surrounding gas, but are independent of the applied acceleration due to the shock wave. A comparison of the theoretical estimate of the velocity ratio with experimental values yielded good agreement.

### 2.1.2 Haas and Sturtevant

Close to 25 years later, Haas and Sturtevant experimentally studied the interaction of a weak planar shock wave with spherical and cylindrical volumes of gas [18]. Four configurations were examined: a helium cylinder, a helium soap bubble, a Refrigerant 22 (R22) cylinder, and a R22 soap bubble. In each case the ambient gas was air, the bubble/cylinder diameter was 5.0 centimeters, and the shock strength was approximately Mach 1.2. The experiments were performed in the GALCIT shock tube, which has a 8.9

cm square test section [52]. The deformation of the spherical or cylindrical volume of gas, and the motion of wavefronts were imaged using a spark shadowgraph optical system. Only one image was obtained per experiment. Piezoelectric pressure transducers were also used to measure the pressure field at the horizontal axis of symmetry for the volume of gas. Since this thesis involves the study of a heavy gas cylinder, we only discuss the results related to this configuration. To create the cylindrical column of gas, two circular 3 mm thick Pyrex disks were used to form the ends of the cylinder, and then a 0.5 $\mu$m thick nitrocellulose membrane was wrapped around the circumference of the disks.

The interaction of the incident shock wave with the R22 cylinder, which is heavier than the surrounding air, resulted in reflected, refracted, and diffracted wavefronts. When the incident shock hit the air/R22 interface, a reflected shock wave was produced. Part of the incident shock wave refracted inside the cylinder, while the remaining part diffracted around the outside of the cylinder. The refracted wave converged at the focus of the cylinder, producing a large pressure gradient and a high velocity, which caused a wedge to form on the horizontal axis of the cylinder. After shock passage, the cylinder evolved into a vortex pair. The effects of waves reflecting off the side walls on the cylinder evolution were also observed early in the experiment.

The strengths of the wavefronts and their velocities were estimated using the pressure profiles and the shadowgraph images, respectively. The Mach number of the refracted (diffracted) wave determined using the pres-

sure jumps was larger (smaller) than the value calculated using the one-dimensional equations of gas dynamics. This is expected, since the one-dimensional calculations do not account for the curvature of the refracted wave through the cylinder. Using the values of the wave positions and times, the velocities of the wave fronts i.e., the transmitted, diffracted and refracted waves, and the velocities of the interface, upstream and downstream, were estimated and compared with one-dimensional gas dynamics calculations. The predicted initial velocity of the upstream and downstream edges of the cylinder were larger than observed in the experiment. The velocity of the refracted (transmitted) wave was also larger (smaller) than the predicted value obtained from one-dimensional calculations. Again this is due to the flow not being accurately represented by the one-dimensional equations of gas dynamics. The velocity calculations also showed that there was little contamination of air inside the R22 cylinder.

The initial velocity of the bubble after shock passage and the final velocity of the bubble after vortex formation were compared with existing theories. The values were compared with the bubble velocity predictions by Rudinger and Somers, discussed in the previous section, and with the linear stability analysis of the Richtmyer-Meshkov instability. The experimentally observed velocities were larger than the predicted values. One reason cited for the differences was the effect of the side walls on the cylinder evolution.

### 2.1.3 Picone and Boris

The experiments performed by Haas and Sturtevant provided a good database for studying the evolution of a cylindrical or spherical volume of gas after the passage of a planar shock wave. Picone and Boris studied the early and late time phenomena of these experiments numerically and examined the vorticity generated by the shock/bubble interaction [34]. This study was performed to verify the non-linear theory derived by Picone for the late-time vorticity, which is discussed in Chapter 6. The simulations were performed using the FAST2D code [33], which is an inviscid, compressible fluid dynamics code. The code neglects surface tension and physical viscosity, and solves the Euler equations using a flux-corrected transport method. The code employs adaptive-mesh refinement and allows fine zones to move with specified structures in the flow field. The initial conditions used in the simulations were chosen to closely match the experimental setup. All four configurations of the Haas and Sturtevant experiments were simulated, but we focus only on the results relating to the R22 cylinder evolution.

Picone and Boris examined the interaction of a Mach 1.23 shock wave with a R22 cylinder of diameter 5.1 cm. Only the upper half of the cylinder was simulated, since the lower half is just a mirror image of the upper half. The simulations were performed in Cartesian coordinates and the initial fine grid surrounding the cylinder boundary was set to follow the cylinder throughout the calculation. Good qualitative agreement was achieved between the density images obtained from the simulation and the experi-

ment. Quantitative agreement was also achieved between the experimental and computational velocities of the upstream and downstream edges of the evolved cylinder.

Negative vorticity was initially generated on the upper half of the cylinder due to the misalignment between the density gradient of the cylinder and the pressure gradient of the shock wave. It was observed that this vorticity deposition drove the late-time evolution of the cylinder into a vortex pair. The circulation predicted from Picone's late-time vorticity theory was larger than the value computed from the simulation. This difference is due to the complicated distortion and interaction of waves that occurs in the simulation.

### 2.1.4 Quirk and Karni

Quirk and Karni [41] also simulated the experiments performed by Haas and Sturtevant. Unlike Picone and Boris, Quirk and Karni concentrated on the early stages of the shock/cylinder interaction and compared their results with those obtained experimentally. The interaction of a Mach 1.22 shock wave with a cylindrical bubble of R22 and a cylindrical bubble of helium were both examined. Again, we only concentrate on the results related to the R22 cylindrical bubble.

This numerical study allowed for a better comparison with experimental data than the previous simulations of Picone and Boris. The previous simulations employed a single-gas flow model, while a two-gas flow model was used in this simulation. The flow model used was derived using the two-

dimensional two-fluid compressible Euler equations. The simulation also contained a shock-capturing scheme, which employed correction terms to mimic a "viscous" shock profile. An adaptive mesh refinement scheme was also used to refine the problem in both time and space based on gradients in the flow field. The scheme was implemented in parallel using a Single Program Multiple Data model.

The parameters in the simulation were chosen to closely match the experimental setup. The side walls of the experimental shock tube were modeled using reflecting boundary conditions. The cylinder was assumed to be in thermal equilibrium with the surrounding air, and the R22 cylinder and surrounding air were both modeled as perfect gases.

Comparisons with the experimental shadowgraph images, velocity measurements, and pressure traces were performed. The simulated images reproduced the features of the shock/cylinder interaction visible in the experimental images. A prong-like feature was evident in the simulations along the cylinder's horizontal axis of symmetry; this feature was less evident in the experiment. The prominence of this feature was hypothesized to be caused by the lack of viscosity in the simulation. The velocities of the wavefronts and the cylinder interface were determined using positions and corresponding times. The values of the computational and experimental velocities were within the experimental error of 11%. Variations in the refracted wave velocity as it passed through the cylinder could not be quantified in the experiment; this led to a large disagreement between the computational and

experimental values of this velocity. The pressure tracer measurements were not used for comparison, since the measurements were not deemed accurate due to the intrusive procedure used to make the measurements.

The initial deposition of vorticity was also examined and the circulation calculated. It was found that the circulation grew linearly during the transversal of the shock through the cylinder. This linear growth was attributed to the fairly constant velocity observed on the horizonal axis of symmetry of the cylinder. This result showed weaknesses in the theories used to predict the circulation generated by the shock/cylinder interaction [34, 49].

### 2.1.5 Jacobs

Additional experiments were performed by Jacobs to examine the mixing induced by the shock/cylinder interaction [21, 23]. The interaction of a Mach 1.095 shock wave with a cylinder of $SF_6$ gas and with a cylinder of helium were both considered. The experiments were performed using the 17 inch Galcit shock tube. The 26.67 cm square test section, compared to the 8.9 cm square test section of the shock tube used in the Haas and Sturtevant experiments, resulted in a smaller effect of the side walls on the cylinder development. The evolution of the cylinder was imaged using planar laser-induced fluorescence (PLIF). The gas was seeded with the tracer biacetyl and made to fluoresce using a sheet of laser light. Only one image was obtained per experiment, so a composite time evolution was created using data from

different experiments. A laminar jet was used to create the cylinder, which prevented the presence of a membrane from effecting the cylinder evolution. The diameter of the cylinder was approximately 0.8 cm, significantly smaller than the 5 cm cylinder diameter examined by Haas and Sturtevant. The experimental results for the $SF_6$ cylinder configuration are presented here, since the current study also examines a shock-accelerated $SF_6$ cylinder. A detailed description of the interaction of the helium cylinder with the shock wave can be found in [6].

The experimental PLIF images were similar to the shadowgraphs obtained by Haas and and Sturtevant. Vorticity was generated on the cylinder boundary by the shock/cylinder interaction. The cylinder deformed into a crescent shape with a small protrusion visible at the downstream edge of the cylinder, which resulted from shock focussing. The vorticity deposited on the boundary of the cylinder separated from the gas and formed a pair of vortices; the strong centripetal acceleration then caused the heavy gas to wrap around the vortices. An instability, resulting from either the Rayleigh-Taylor instability or the Kelvin-Helmholtz instability, was observed as small waves on the downstream edge of the vortex pair. This instability caused the the vortex pair to "breakup" and dominate the late-time dynamics of the cylinder evolution. An initially symmetric $SF_6$ cylinder was not obtained in this experiment and the effect of this asymmetry was visible in the experimental images.

The initial and final velocities of the cylinder after shock passage and

the vortex displacement were compared with the theory of Rudinger and Somers discussed in Section 2.1.1. The experimental value of the initial cylinder velocity agreed well with theory, but it was found that the theory underpredicted the final velocity of the cylinder after its evolution into a vortex pair. The vortex displacement $d$ in the experiment was also larger than the predicted value of d $=\pi/4$ D, where D in the initial diameter of the cylinder. The differences between the experiment and the theory may be due to the assumptions of an incompressible, inviscid flow and a uniform density distribution, made in the derivation of the theory. These experiments serve as a basis for comparison with the data obtained in our current experiment.

## 2.2 Evolution of the Los Alamos Gas Shock Tube

We present the evolution of the Los Alamos gas shock tube, since its original construction in 1984. The improvements and modifications made to the shock tube are presented in chronological order to show how the shock tube has evolved into its present configuration.

### 2.2.1 Early Experiments

Early shock tube experiments were performed by Benjamin to analyze the growth of the Richtmyer-Meshkov instability [3]. Benjamin considered

a single-mode perturbed interface between air and $SF_6$, and between air and helium to examine the growth of a light-to-heavy and heavy-to-light configuration, respectively. A membrane composed of cellulose nitrate was used to create the initial sinusoidal perturbation, which had a wavelength of 37.5 mm and an amplitude of 2.4 mm. The imaging diagnostics consisted of two shadowgraph systems; the first was used to obtain one high-resolution image of the interface and the second was used to obtain 12 low-resolution frames, which enabled growth rate measurements. The interface growth due to a Mach 1.24 shock and one reshock was examined.

Qualitative agreement with Meshkov's shock tube data was achieved, but differences were observed in the quantitative measurements of the growth rate. Benjamin observed linear growth of the amplitude, which was somewhat larger than the results of Meshkov's experiments, but significant smaller than predicted by Richtmyer's linear theory. This experiment was subsequently simulated using front tracking [17]. This was the first simulation of the Richtmyer-Meshkov instability to give quantitative agreement with the experimental growth rate.

### 2.2.2 PLIF Imaging System

A few years later the evolution of a shock-accelerated thin fluid layer was studied using the gas shock tube. The thin fluid layer, denoted by the "gas curtain", contained perturbations on the upstream and downstream edges of the $SF_6$ layer [23], so two interfaces, light-to-heavy and the heavy-

to-light, existed in this experiment. In contrast to the earlier shadowgraph system, the cross-section of the $SF_6$ curtain was observed using planar laser-induced fluorescence(PLIF). The $SF_6$ gas was seeded with diacetyl, which is a fluorescent dye used to track the $SF_6$ flow. Only one image was captured per experiment, which was one drawback of the new imaging technique.

The thin fluid layer was not constructed using a membrane as in previous experiments. A laminar gas jet was used to produce the "gas curtain" configuration. The jet flowed through a contoured nozzle at the top of the test section and a suction was used at the bottom of the test section to remove the $SF_6$ gas. This technique avoided the effect of membrane fragments on the evolving flow.

It was observed that the thin fluid layer was very sensitive to small variations in the initial conditions. Three resulting flows, upstream mushrooms, downstream mushrooms, and sinusoidal patterns, were observed. A theoretical model was developed to quantify the mixing width of the evolving thin fluid layer [22]. The model was based on the assumption that the initial vorticity deposition on the boundary of the thin fluid layer could be represented by a row of line vortices. The model predicted logarithmically growth of the layer at late time. Even though scatter was observed in the experimental plot of the mixing width versus time due to the three different observed flow patterns, the experimental measurements of the layer thickness compared well with the theoretical prediction. This provided confidence in the PLIF imaging system.

### 2.2.3 Rayleigh Scattering

As discussed above the shock tube experiments of the "gas curtain" resulted in three observed morphologies: upstream mushrooms, downstream mushrooms, and a sinuous pattern. With the PLIF imaging technique used, only one image was obtained per experiment. This limitation led to the implementation of a new imaging system, which used planar laser Rayleigh scattering to obtain two images per experiment, one of the initial conditions and one of the dynamic evolution [7].

Obtaining two images per experimental run allowed for a correlation to be made between the initial conditions and the three observed flow patterns. It was found that if the upstream perturbation was slightly larger than the downstream perturbation in the initial conditions, upstream mushrooms would evolve. Similarly, if the downstream perturbation was larger than the upstream perturbation, downstream mushrooms would evolve. The sinuous pattern would occur if the initial upstream and downstream perturbations were nearly equal in amplitude. This correlation could not be observed with the PLIF imaging technique used previously. These experments was used for RAGE code validation [2], as discussed in Section 2.3.1.

### 2.2.4 Multiple Dynamics Images

Further improvements were made to the imaging system, which allowed multiple images of the flow evolution to be obtained [46]. Unlike the Rayleigh

scattering of the $SF_6$ gas performed previously, this system added tracer fog to the gas to enhance the light scattered from the $SF_6$ layer. This decreased the necessary laser intensity and the acquisition of new CCD cameras increased the dynamic range of the images; this resulted in the availability of multiple high-resolution images per experiment. Nine images in total were obtained, one image of the initial conditions and eight images of the evolution of the $SF_6$ gas layer. It was shown using Stokes' drag analysis that the fog particles accurately followed the flow of the $SF_6$ gas. Also images obtained from this experiment closely resembled images obtained previously with direct Rayleigh scattering. One drawback of this new imaging technique is that the peak $SF_6$ concentration can not be determined as it was with direct Rayleigh scattering.

With the multiple images per experiment, the growth rate of the "gas curtain" was determined. The mixing width of the layer was measured using the images obtained at the eight experimental times. It was found that for all three observed flow patterns, the layer initially grew and then asymptotically approached a constant value. This result was consistent with the estimates of the mixing width growth derived using the vortex blob approach [30] and the point vortex model [22].

### 2.2.5 Evidence of Turbulent Mixing

Additional experiments were performed with multimode perturbations to quantify the mixing transition and the onset of turbulence observed in the

evolution of the thin fluid layer [47, 57]. The flow was initially dominated by the shock-induced vorticity deposited on the boundary of the layer. This vorticity produced both large and small scale structures, before the flow evolved into a highly distorted state.

Three analysis techniques, histograms, wavelets, and structure functions, were used to quantify the mixing transition. The histogram approach measured the intensity of the light scattered from the thin fluid layer. An abrupt decrease in the air or $SF_6$ intensity i.e., the presence of mixed material, indicted a mixing transition [47]. This transition was observed in the analysis of the multimode configurations. The wavelet analysis was used to quantify the size and location of observed structures. Using wavelet transforms described by Farge [12], scales larger and smaller than the initial perturbations were observed. This signified a transition to turbulence. Structure functions were also examined. Vorobieff *et al.* constructed second-order structure functions of the light intensity scattered off the thin fluid layer [57]. Evidence of a power-law behavior was observed, which again implied a transition to turbulence.

### 2.2.6 Particle Image Velocimetry

The need for more quantitative measurements of the experimental flow resulted in the implementation of Particle Image Velocimetry (PIV) [39]. The fog particles initially added to the flow for visualization purposes were also necessary for the implementation of PIV. The velocity field at one experimen-

tal time was determined under the assumption that the added fog particles accurately follow the flow of the $SF_6$ gas. A double-pulsed high-resolution image showing individual particles was obtained from the experiment and then interrogated to determine the velocity of the flow. The mean convective velocity and the fluctuating velocity of the flow were both determined. Therefore, velocity and the computed quantities of vorticity and circulation were available from this experiment. More details of PIV can be found in the discussion of the experimental diagnostics in Section 3.3.

The circulation derived from PIV measurements of the evolving "gas curtain" was used to validate the model for the mixing width growth derived by Jacobs *et al.*, in which the shock-accelerated layer is modeled by a row of counterrotating point vortices [40]. This model for the mixing width growth depends on the circulation value. Curve fits of the mixing width versus time were performed to determine the predicted circulation value. The experimental circulation value was then determined from the velocity field data. Good agreement was achieved between the value derived from the model and the value determined from the experimental velocity measurements.

This configuration of the shock tube is used in the present study. Chapter 3 explains the shock tube apparatus in greater detail, including the initial conditions, the diagnostics, and the limitations associated with this configuration. As will be discussed, the current study also led to a redesign of the flow system to obtain a more laminar flow. The shock tube continues to be improved to provide a more complete picture of the experimental flow.

## 2.3 RAGE Code Validation Efforts

The RAGE code used in this study has been validated for the single-mode Richtmyer-Meshkov instability using experimental data and analytic test problems. Here we present two extensive RAGE code validation efforts, which examine experimental data obtained from the DX-3 shock tube experiments at Los Alamos National Laboratory (LANL) and from the Nova Laser at Lawrence Livermore National Laboratory (LLNL).

### 2.3.1 Shock Tube Experiments

Experimental data from the shock tube was compared with computational results from the the RAGE code[2]. RAGE is a multi-dimensional adaptive mesh Eulerian hydrodynamics code; it is described in detail in Chapter 4. Baltrusaitis *et al.* examined the "gas curtain" experiments discussed in the previous section. At the time of this code validation effort, the evolution of the "gas curtain" was imaged using direct Rayleigh scattering. Only two images, one of the initial conditions and one dynamic image of the evolving curtain, were obtained per experiment.

As previously discussed, the experiments examined the interaction of a thin fluid layer of $SF_6$ gas, the "gas curtain", with a planar Mach 1.2 shock wave. The "gas curtain" cross-section resembled a sinusoidal perturbation of wavelength 6 mm with a mean layer thickness of 3 mm. Three evolutionary patterns were observed showing the sensitivity to the experimental initial

conditions. It was noted that upstream mushrooms developed if the initial perturbations resided primarily on the upstream side of the layer. Likewise downstream mushrooms resulted when the initial conditions contained a predominant downstream perturbation. A sinusoidal pattern was observed when the initial upstream and downstream perturbations were nearly equal in amplitude.

Three types of simulations were performed to examine the sensitivity of the initial conditions to the density gradient and to small differences in the amplitude of the initial perturbation. Baltrusaitis *et al.* examined three cases: 1) pure air and $SF_6$ gas, 2) initially mixed air and $SF_6$ gas, and 3) the imaged experimental initial conditions. The initial perturbations on the upstream and downstream sides of the "curtain" were varied so that all three flow patterns were observed for each case. Good visual agreement was achieved between the experimental and computational density images. Additional analysis was performed to examine the mass distribution in a square area of the resulting flow. A comparison of the experimental and computational mass distributions also shows good agreement.

Baltrusaitis *et al.* concluded from these results that RAGE was able to accurately capture the flow of the evolving "gas curtain". This conclusion was based on the comparison of integral measures, which were the only diagnostics available at the time of this experiment. The present study contains improved diagnostics which allow for a more stringent test of the RAGE code.

### 2.3.2 Nova Laser Experiments

A comparison of experimental, theoretical, and computational results for the Richtmyer-Meshkov single-mode perturbation was also performed. Dimonte *et al.* [10] experimentally examined a perturbed interface between Beryllium and foam in planar geometry for large Mach numbers and high compressibility. These experiments were modeled computationally using three different hydrodynamics codes. The density images, and the amplitude and growth rate of the perturbation were all used for comparison.

The single-mode Richtmyer-Meshkov experiments were performed on the Nova laser using radiatively driven shock waves [10]. An indirect drive was used in this experiment; laser beams were directed into a hohlraum to create a quasi-Planckian x-ray spectrum. The target consisted of a beryllium ablator and a foam tamper with a single-mode interface perturbation. The dense beryllium was transparent to the diagnostic x-rays, while an x-ray dopant had to be added to the foam to adjust its opacity. The x-rays in the hohlraum heated the target, producing an expanding ablation plasma and creating a planar shock wave which moved through the target.

The imaging diagnostics used in this experiment were side-on and face-on radiography. Face-on radiography was used to quantify small amplitudes at early time, which could not be well-detected with side-on radiography. The side-on radiography was then used to measure the shock characteristics and the interface evolution after shock passage. The resulting images allowed for the measurement of the amplitude and growth rate of the interface.

The experiments were modeled with three hydrodynamics codes: FronTier, RAGE, and PROMETHEUS. FronTier [15, 16] is a front tracking code, which keeps shocks as true discontinuities. The flow is represented by a fixed, rectangular grid with the addition of a lower-dimensional grid that tracks fronts in the flow, such as contact discontinuities, shock waves, and refracted waves. The code also employs an operator-split second-order Godunov scheme. The code PROMETHEUS [13] employs an operator-split piece-wise parabolic method (PPM), which is part of the family of higher-order Godunov methods. This method accurately follows shocks by reducing the diffusion present at the discontinuity. The RAGE code [14, 58] is the adaptive-mesh Eulerian code, which has no front-tracking capability. The code employs a directionally split second-order Godunov scheme. In all simulations, a pressure drive was used as opposed to a radiation drive, and a perfect gas was assumed for the beryllium and the foam.

The experiments and the simulations were performed for the following initial conditions: 1) a Mach 15.3 shock with interface perturbation $\lambda = 100\mu m$, $a_0 = 10\mu m$, 2) a Mach 15.3 shock with interface perturbation $\lambda = 100\mu m$, $a_0 = 4\mu m$, and 3) a Mach 10.8 shock with interface perturbation $\lambda = 100\mu m$ $a_0 = 4\mu m$. Additional simulations were performed to examine the effect of varying the initial perturbation amplitude $a_0$, and the Mach number of the incident shock wave.

The amplitude of the interface, which is defined as half the mix width, and the growth-rate of the interface amplitude were determined from the

experiments, the simulations, and the theories [20]. The impulsive model of Richtmyer, the linear theory of Yang *et al.*, and the nonlinear theory of Zhang and Sohn were all used for comparison. Good agreement was achieved between the experimental data, the three simulations, and the nonlinear theory. The linear theory correctly predicted the growth at early times, but overpredicted the growth at later times. The non-linear theory predicted growth that was consistent with the experiment and the simulations at both early and late time.

The density images obtained using side-on radiography in the experiment were also compared with the density images from the three simulations. A phase inversion of the interface and growth of the initial perturbation were observed in all cases. There was good agreement of the large scale structures, but differences were observed in the small scale structures. For example, the effect of the Kelvin-Helmholtz instability was more pronounced in the PROMETHEUS simulations, then in either the RAGE or FronTier simulations. Unfortunately the experimental resolution was insufficient to resolve any small scale structures that could have been used for a more detailed validation.

Additional experiments have been performed with the Nova laser, which provide even more data [11, 44]. These experiments explore the effect of strong shocks and compressibility, which distinguishes them from small-scale shock tube experiments.

## 2.4 Velocity Measurements of Shocked Flow

A group of researchers from the Commissariat á l'Energie Atomique in France have gathered one-dimensional velocity measurements from shock tube experiments using Laser Doppler anemometry (LDA) [36]. The vertical shock tube used in these experiments has a square 8 cm x 8 cm cross section with an end wall placed 30 cm from the initial interface. Poggi *et al.* created a multimode perturbation between an air and $SF_6$ interface using a wire mesh membrane in the shock tube. The evolution of the interface resulting from its interaction with a Mach 1.45 shock wave and two reshocks from the end wall were examined. The mixing zone was imaged using Schlieren visualization.

The air and $SF_6$ gas were seeded with incense and olive oil, respectively, so that velocity measurements could be obtained. The instantaneous velocity in the axial direction was measured using laser Doppler anemometry (LDA) at five locations downstream from the initial interface. The velocity variations due to the passage of the incident shock and reshocks were observed. It was concluded from the experimental data that a turbulent mixing zone was generated by the incident shock wave. The velocity measurements were used to characterize this turbulent mixing zone.

Using this extensive experimental data, one-dimensional numerical simulations were performed to compare the mixing zone growth and the turbulent kinetic energy with the experimental data [56]. The simulations were

performed with a one-dimensional Lagrangian hydrodynamics code, containing the BHR mix model [4]. This model has 17 coefficients which were set based on previous theoretical and experiment analyses [5]. Good agreement was achieved between the experimental and computational mixing zone widths, but large disagreements were observed between the turbulent kinetic energies. The calculated turbulent kinetic energy was a factor of 10 larger than the value determined from the LDA measurements in the experiment. From these results, it was determined that the coefficients for the BHR mix model must be initialized for each different experiment, since agreement was not achieved using coefficients derived from previous theoretical and experimental analyses.

Two-dimensional simulations were then performed of the same shock tube experiments [28]. The main focus of these simulations was to study the growth of the turbulent mixing zone and to show that the simulations exhibited a turbulent regime comparable to the experiment. The CAD-MEE code, which solves the two-dimensional unsteady Naiver-Stoke's equations using an Arbitrary Lagrangian-Eulerian (ALE) approach, was used for the simulations. The initial multimode perturbation was composed of eight wavelengths on the order of the experimental mesh size. Good agreement was achieved when comparing the computational turbulent mixing zone with experimental data. As in the previous one-dimensional simulations, the calculated values of the turbulent kinetic energy were larger than the values obtained in the experiment. Full three-dimensional simulations need to be

performed before making any conclusions based on these differences; this is necessary due to the different nature of two-dimensional turbulence and three-dimensional turbulence.

# Chapter 3

# Shock Tube Facility

Our experiments were performed using the shock tube at Los Alamos National Laboratory. As discussed in the previous chapter, extensive improvements to the diagnostic capabilities have been made through the years, which provides a more complete picture of the experimental flow. Numerous experimental, theoretical, and computational analyses have been performed using the data obtained from these shock tube experiments [2, 39, 40, 46, 47]. This chapter will describe the shock tube apparatus and the diagnostics used to acquire data. More experimental details can be found in [39].

## 3.1 Apparatus

The apparatus used in the experiment is the gas shock tube shown in Figure 3.1. The shock tube is approximately 5.4 m long with a 7.5 cm

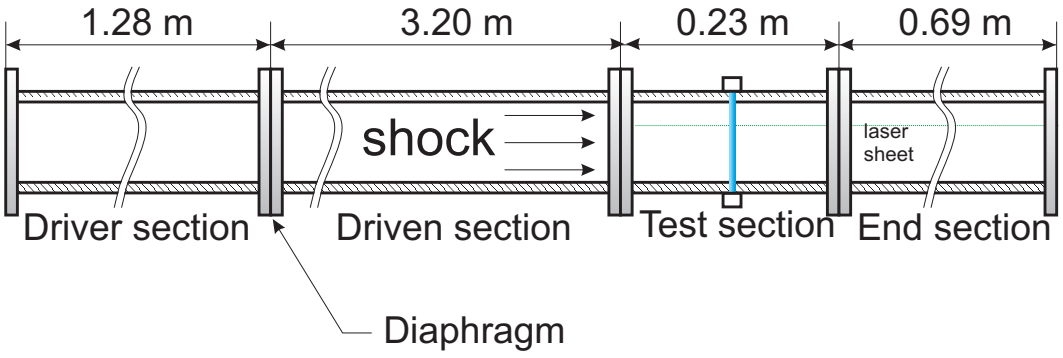


Figure 3.1: Schematic of the gas shock tube

square cross-section. It is divided into four sections: the driver section, the driven section, the test section, and the end section. The driver section and the driven section are separated by a diaphragm consisting of four thin polypropylene sheets. The driver section, which contains nitrogen gas, is pressurized to 20 psi above local atmospheric pressure. This pressure difference is set to produce the desired speed of the shock wave. A "solenoid-actuated diaphragm burster" is used to puncture the membrane between the driver and driven sections. This produces a Mach 1.2 shock wave, which is ragged at first and then becomes planar due to the stable fluid dynamical structure of a shock wave. The shock travels down the driven section and hits a vertical cylinder of sulphur-hexafluoride ($SF_6$) in the test section. The creation of the $SF_6$ gas cylinder is discussed in the next section.

The test section, shown enlarged in Figure 3.2, is the main area of interest. Diagnostics are added in this section to observe the interaction of the

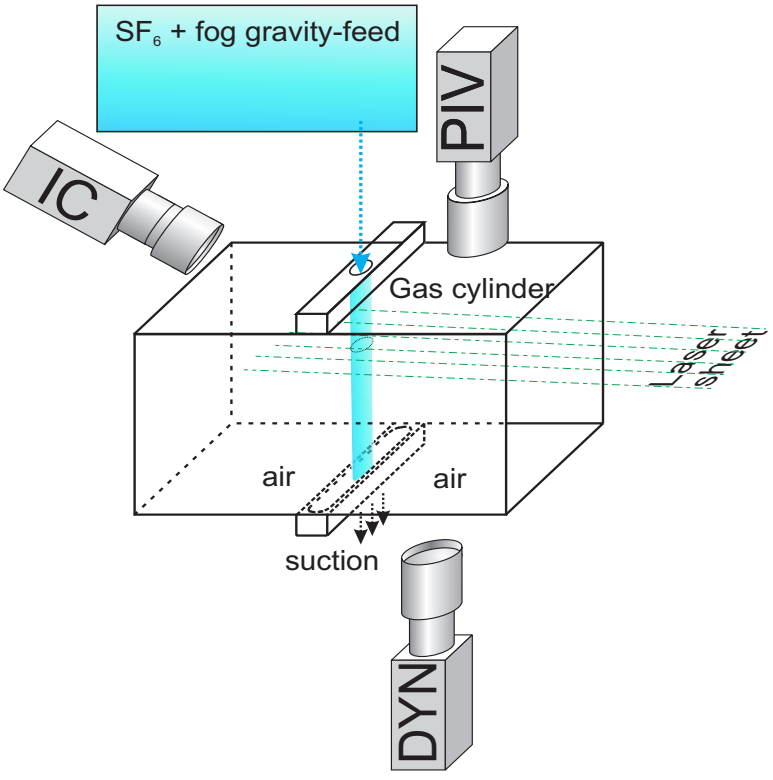


Figure 3.2: Test section of the shock tube

shock wave with the $SF_6$ gas cylinder. After the shock/cylinder interaction, the shock wave travels down the shock tube into the end section and reflects off the end wall. This reflected wave returns to the test section in about 3.5 ms, which is after the experimental observation time of interest. New hardware designs are being considered to capture the effects of reshock by moving the end wall closer to the test section. Present imaging diagnostics limit this capability. We do not consider the shock wave reflected from the end wall in this study.

## 3.2 Gas Cylinder Creation

We create the gas cylinder of diameter 0.8 cm by flowing a mixture of sulphur-hexafluoride ($SF_6$) and glycol droplets through a cylindrical contoured nozzle atop the test section of the gas shock tube, which is described in the following section. A modified fog generator is used to produce glycol droplets that seed the $SF_6$ gas. These droplets allow for visualization of the flow and for Particle Image Velocimetry, which is discussed in Section 3.3.1. Previous analysis has shown that the glycol droplets accurately track the flow of the $SF_6$ gas [39, 47].

Initial attempts to generate the $SF_6$ cylinder failed, because small vortices developed on the circumference of the cylinder. This led to a redesign of the flow system to create a more laminar flow. The new system is a gravity-driven flow system as opposed to a pressure-driven flow system used

in previous "gas-curtain" experiments. The $SF_6$-glycol mixture is created inside a settling tank. A fog generator is placed inside the tank and "puffed" to create glycol droplets. The tank is then infused with $SF_6$ gas to produce a mixture of $SF_6$ gas and glycol droplets. An air monitoring system is used to confirm that the amount of air present in the settling tank is insignificant. The $SF_6$-glycol mixture is then gravity-driven into the test section through a nozzle containing the perturbation for the gas cylinder. Because $SF_6$ gas is over five times as dense as air, it easily displaces air and produces a "column" of $SF_6$ gas, much like water falling from a faucet produces a column of water. Suction is used at the bottom of the test section to remove the $SF_6$-glycol mixture. Various nozzles, including the present cylinder configuration, have been constructed to examine different perturbations.

## 3.3 Diagnostics

We use photographic diagnostics to monitor the evolution of the $SF_6$ cylinder. The diagnostics are located in the test section of the shock tube and capture the interaction of the shock wave with the $SF_6$ cylinder.

Two lasers are used in this experiment to image the evolution of the cylinder. The lasers illuminate a horizontal slice through the gas cylinder, allowing CCD cameras to capture images of the cylinder development. The first laser is a customized frequency-doubled ND:YAG laser, which is configured to send seven pulses separated by 140 $\mu$s. The second laser is a

commercial 10-Hertz "New Wave" laser, which is pulsed once to obtain Particle Image Velocimetry (PIV) data. Three single-frame, intensified CCD cameras at fixed, preset fields of view, shown in Figure 3.2, image the slice of the cylinder illuminated by the horizontal laser sheet. The Initial Condition (IC) camera takes a picture of the initial state of the gas cylinder before shock passage. This image has a resolution of 55 $\mu$m/pixel. The Dynamic (DYN) camera records six images of the time evolution of the gas cylinder at a resolution of 100 $\mu$m/pixel. The Particle Image Velocimetry (PIV) camera is used to obtain a double pulsed image at a resolution of 16 $\mu$m/pixel. This double-pulsed image is used to determine the velocity field at the time corresponding to the last dynamic image. The current hardware configuration limits the PIV capability to only the last time of observation.

### 3.3.1 Particle Image Velocimetry (PIV)

The quantitative measurement of velocities, in addition to the qualitative flow field, is achieved through Particle Image Velocimetry (PIV) [42]. Particle Image Velocimetry is a optical technique which tracks the flow of the gas by measuring the flow of the tracer particles. This technique allows for a better characterization of the experimental flow and also allows for a more stringent comparison with numerical simulations.

In this experiment, we add glycol droplets to the $SF_6$ gas and use this mixture to form the initial cylinder. Two closely spaced laser pulses are used to obtain two images of the cylinder separated by a small time difference.

The resulting double-pulsed image is then interrogated using the VISIFLOW PIV analysis software to determine the velocity of the particles [1]. The PIV image is divided into small square boxes where the box size depends on the time difference between the two images and the amount of particles added to the flow. Note each interrogation box roughly contains eight to ten particles. The PIV software interrogates each box using single frame cross-correlation. The software also calculates the mean convective velocity, which we subtract from the flow field in our analysis to show fluctuations of velocity in the cylinder frame of reference. The ability of the tracer particles to accurately follow the flow is crucial for the application of PIV, since we equate the velocity of the flow with the velocity of the particles. The ability of the glycol droplets to accurately follow the $SF_6$ gas in this experiment has been extensively investigated [39]. In one study, Prestridge *et al.* theoretically examined how velocity fluctuations in the $SF_6$ gas would affect the glycol droplets contained in the flow. This was performed by analyzing the balance between Stoke's drag and inertia, which dominates the motion of the droplets. It was found that the glycol droplets are able to follow 99% of the velocity fluctuations in the flow.

## 3.4 Reproducibility

For each experimental run, we obtain one image of the initial conditions, six images of the dynamical evolution of the cylinder, and one double-pulsed

image used for PIV. Figure 3.3 shows the cylinder evolution for six different experiments performed on the same day. The shock and the flow move from left to right in the figure. The initial condition image is the left most image and the next six dynamic images are taken at 140 $\mu$s intervals.

Examining the cylinder evolution, we observe the same features in each of the experiments. We see that after shock passage, the cylinder evolves into a vortex pair. The presence of a secondary instability is also evident on the right edge of the cylinder at late time. Although small variations are detected between data gathered on different days by different people, the characteristic evolution of the cylinder into a vortex pair is observed in all of the experiments. The reproducibility between experiments is believed to be due to the new flow system developed for the introduction of the $SF_6$-glycol mixture into the test section. Earlier gas-curtain experiments performed using the same shock tube lacked reproducibility. Depending on the relative amplitudes of the left and the right perturbation in the initial conditions, three possible flow evolutions were observed.

## 3.5 Limitations

There are a few experimental limitations that we must be aware of to correctly interpret the experimental data. Due to the present imaging technique, the peak concentration of $SF_6$ gas in the initial conditions is not known; we only know the relative intensities of the pixels in the initial condi-

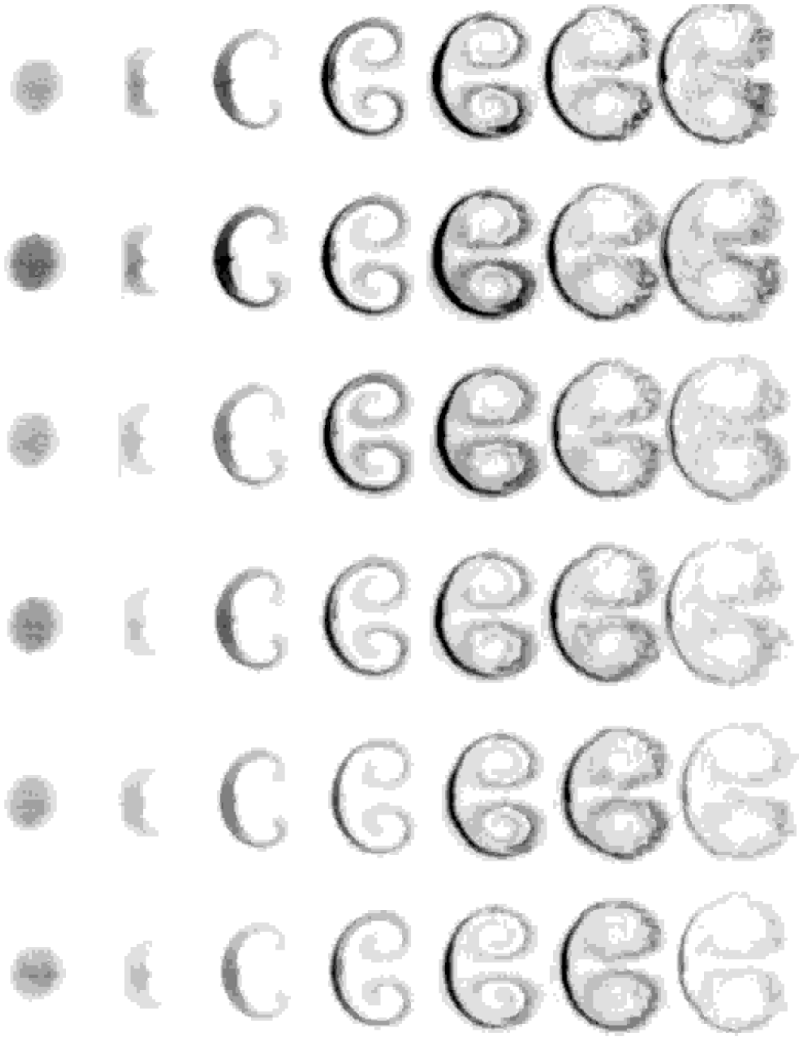

Figure 3.3: Experimental images of the cylinder's evolution

tions image. Therefore a series of simulations varying the peak concentration of the $SF_6$ gas in the initial conditions are performed to examine the effect of different initial concentrations.

The current hardware configuration of the shock tube also limits the information we can gather from the experiment. We would like to obtain PIV at an earlier time, but this is not possible with the current experimental configuration, since an unobstructed view of the evolving cylinder can not be obtained. The experimenters are examining the possibility of redesigning the shock tube to achieve this capability.

# Chapter 4

# The RAGE Code

The simulations shown in this thesis were performed using the Radiation Adaptive Grid Eulerian (RAGE) code, which is a multi-dimensional compressible hydrodynamics code. As discussed in Chapter 2, validation studies of the Cray Fortran 77 version of this code have been performed using analytic test problems and experimental data of the single-mode Richtmyer-Meshkov instability. Over the past two years, the RAGE code has been rewritten from its original Cray Fortran 77 version into a parallel Fortran 90 version [58]. Validation studies run on the Cray version are presently being rerun on the new parallel version of RAGE. The results from both versions are being compared.

This present study aids code validation efforts by comparing RAGE simulations with high-resolution experimental data of a shock-accelerated heavy gas cylinder that was presented in the previous chapter. Note this is

the first code validation study of a shocked flow that uses two-dimensional velocity field data for comparison. The velocity measurements allow us to perform a more stringent test of the code's capability to accurately model the Richtmyer-Meshkov instability.

## 4.1 Overview

RAGE is developed by Michael Gittings at Science Applications International Corporation (SAIC) and is presently being used extensively at Los Alamos National Laboratory for a variety of hydrodynamics and radiation-hydrodynamics problems. The main features and assumptions of the RAGE code, relevant to our study of hydrodynamics, are listed below. The RAGE code:

- Is a one, two, and three dimensional, compressible hydrodynamics code
- Supports Cartesian (1D,2D,3D), cylindrical (1D, 2D), and spherical (1D) coordinate systems
- Employs continuous adaptive mesh refinement (CAMR)
- Solves the Euler equations derived from the conservation of mass, momentum, and energy
- Uses a second-order piecewise linear Godunov numerical scheme
- Neglects molecular diffusion and physical viscosity

- Assumes temperature and pressure equilibrium in each cell
- Allows for mixed material cells
- Outputs hierarchal data files (HDF) and/or scientific data sets (SDS)
- Uses domain decomposition and MPI (Message Passing Interface) for parallelization.

## 4.2 Continuous Adaptive Mesh Refinement (CAMR)

One of the main features of the RAGE code is its CAMR capability. CAMR allows the grid to adapt, as necessary, to follow gradients in the flow-field, such as shocks, material interfaces, and contact discontinuities. Since a uniform high-resolution grid is generally not necessary to refine important small scale structures, the amount of computational time needed to perform a simulation is greatly decreased.

Here we present the methodology of CAMR used in the RAGE code. Note that zones in RAGE are square in two dimensions and cubic in three dimensions. RAGE defines zone sizes by levels; level one corresponds to the coarse zone size of the top grid. Each subsequent level corresponds to the previous level's zone size refined by a factor of two. For example if the level one zone size is 0.1 cm, the level two zone size will be 0.05 cm, and likewise the level four zone size will be 0.00125 cm (i.e., 0.1 cm/$2^3$). Initially the

computational domain is covered by a uniform grid of level one zones. During initialization of the simulation, grid refinement is repeated until gradients in the flowfield are resolved to the requested degree of accuracy. All adaptive mesh refinement decisions are subject to the following two constraints: 1) each zone can be coarsened or refined by a factor of two i.e., one level, during each time step, and 2) adjacent cells can differ by at most one level of refinement.

A sequence of adaptive mesh refinement steps occurring during the initialization of a simulation is illustrated in Figure 4.1. In this example, we assume that three levels of refinement are possible; the maximum level of refinement is set in the RAGE input file. Suppose that a feature requiring refinement exists in the bottom right corner of the domain and that the computational domain is initially divided into four level one zones. In the first refinement step cell four subdivides into four level two zones. Neighboring cells are not allowed to differ by more that one level of refinement, so cells five, six, and seven will not be refined further. Since cell eight is surrounded by level two cells, it is refined further into four level three zones. In this example, further adaption does not occur, since the maximum level of refinement was limited to three levels.

As a further example of CAMR, Figure 4.2 shows the grid refinement performed by RAGE for a planar shock wave. This simulation allows seven levels of refinement, which can be seen by the seven different square zone sizes. In accordance with the CAMR conditions, adjacent cells differ by at

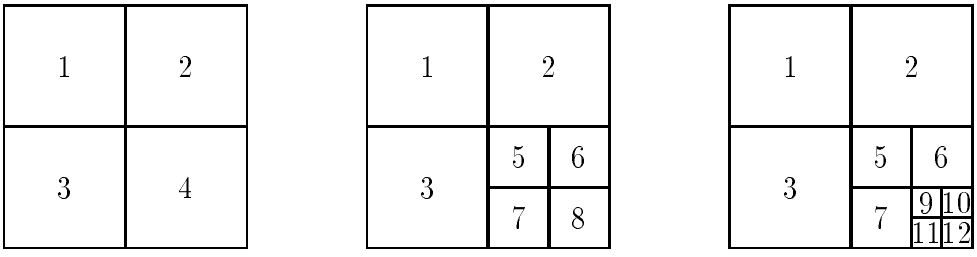


Figure 4.1: Adaptive mesh refinement process

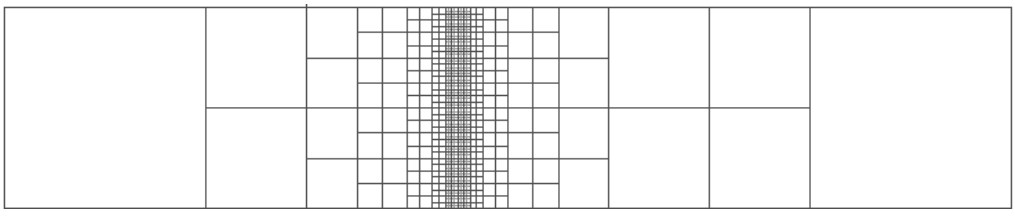

Figure 4.2: Grid refinement for a planar shock wave

most one level of refinement i.e., neighboring zone sizes differ by at most a factor of two. As we move away from the location of the shock, the zone size decreases to the coarsest zone size. This occurs because there is constant density, pressure, and material in these regions i.e., no gradients are present.

## 4.3 Problem Setup

During initialization, the RAGE code reads an input file containing all of the parameters necessary to setup a specific problem, including the material regions, the grid refinement, and the computational domain. The following four sections discuss some of the important RAGE input parameters necessary to setup a problem in a two-dimensional cartesian coordinate system.

### 4.3.1 Zoning

The zone size of the level one mesh and the maximum level of refinement are specified in the RAGE input file. The coarsest zone size, level one, is set by the parameters *dxset* and *dyset*. These two parameters must be equal since zones in RAGE are square. The level of refinement is set by specifying the fine zone size for each material. The parameter *sizemat(n)* sets the fine zone size possible for material n, and *sizebnd(n)* sets the fine zone size possible for the boundary between the materials n and n+1. These values do not need to be equal. Note that the values of *sizebnd* and *sizemat* should

equal *dxset* divided by some power of two i.e, the zone size for a certain level of refinement.

### 4.3.2 Computational Domain

The computational domain size is specified by setting the number of coarse zones in the x and y directions. The parameters *imxset* and *jmxset*, which must be even integers, are chosen such that $dxset * imxset$ is equal to the length, and $dyset * jmxset$ is equal to the width of the computational domain. Note that the size of the computational domain is dependent on the zone size used in the simulation.

### 4.3.3 Regions

RAGE allows the user to easily define different geometrical regions and interfacial perturbations. In two dimensions, circular, elliptic, triangular, and quadrilateral regions can be defined. The parameter *typereg(n)* is used to define the geometrical type of region n. Coordinate values must also be specified to define the location and the shape of the region. Note that region one is always defined as the entire computational domain. Sinusoidal perturbations on the boundary between two materials can also be constructed. The user specifies the amplitude, period, and phase offset of the perturbation. This capability allows for easy problem generation for the single-mode and multi-mode Richtmyer-Meshkov instability.

### 4.3.4 Material Parameters

Based on the low pressure and temperature regime examined in the experiment, the simulations performed in this thesis assume ideal gases. The parameter *keo* specifies the equation of state used in a simulation. The ideal gas equation of state is achieved by setting the parameter *keo* to zero. The gamma,$\gamma$, along with the specific heat, $C_v$, must be specified for each gas.

Two independent material parameters must also be set for each region; possible combinations are density and internal energy, density and temperature, and pressure and temperature. The parameters *rhoreg(n)*, *prsreg(n)*, and *tevreg(n)* are used to set the density, pressure, and temperature of region n, respectively. The x and y initial velocities are set by the parameters *xdreg(n)* and *ydreg(n)*, respectively. Note that RAGE uses cgs (centimeter/gram/second) units, except for temperature which has the units of electron-volts (eV).

## 4.4 HDF and SDS Output Files

RAGE has the capability to output two types of data files, Hierarchical Data Format (HDF) files and Scientific Data Sets (SDS) [31]. Each non-ASCII file contains cell-centered values on a uniform mesh. Table 4.1 shows some of the parameters available to specify when creating HDF and/or SDS files. The size and domain of these files are set in the RAGE input file. The user specifics the number of pixels in the x and y direction using the

| Parameter | RAGE abbreviation | Units |
|---|---|---|
| density | rho | $g/cm^3$ |
| pressure | prs | $dynes/cm^2$ |
| temperature | tem | eV |
| x velocity | xdt | cm/s |
| y velocity | ydt | cm/s |
| volume fraction | v01 or v02 | dimensionless |
| vorticity | omg | 1/s |

Table 4.1: RAGE abbreviations for parameters output to SDS and HDF files

parameters *hdfimx* and *hdfjmx*. The x and y range of the domain are specified using the parameters *hdfxmn*, *hdfxmx* and *hdfymn*, *hdfymx*, respectively.

HDF files are viewed as colored images defined by an eight bit color scheme. The values 0 and 255 correspond to the minimum and maximum material values specified by the RAGE parameters *hdfmn* and *hdfmx*. Cell-centered values in the HDF file are described by a number between 0 and 255, corresponding to the cell's value relative to the minimum and maximum values.

If no values are specified for the parameters *hdfmn* and *hdfmx*, SDS files are created. SDS files differ from HDF files in that the physical value of a parameter in a cell is stored as opposed to its relative color value. The SDS

file contains an array of data, for example density, and one, two, or three arrays of coordinate values, depending on the dimensionality of the problem. We extract the value of each cell-center along a uniform mesh using HDF commands and the SDS file structure found in [31].

A post-processing C program reads and analyzes the data in the SDS files. The data attributes, including the name, dimensions, and numerical type of each array is determined using the command *SDgetinfo* and then all or part of the data array is read using the command *SDSreaddata*. We note the numerical type of each data array in the SDS file is 32-bit floating-point. Postprocessing SDS files produced by RAGE is necessary to determine the velocity field in the simulation.

## 4.5 Computing Platform

The RAGE simulations are performed on the Advanced Computing Laboratory (ACL) Nirvana machine at Los Alamos National Laboratory. This machine is composed of 16 Silicon Graphics origin 2000 multiprocessor "boxes"; each box contains 128, 250 MHz processors and 32 GBytes of memory. The 16 boxes are interconnected using HIPPI ports, which allow high communication bandwidth to be achieved. If all 2048 processors are utilized, the machine has a peak capacity of 1 TeraOps i.e., 1 trillion floating point mathematical operations per second. Parallel runs are queued using LSF (load sharing facility) and the command *bsub* submits a batch job to LSF

with the requested queue, number of processors, and maximum computing time. The RAGE code was modified from its Cray Fortran 77 version into a parallel Fortran 90 version to exploit this new computing capability. The parallel version of RAGE employs domain decomposition, load leveling, and message passage interface (MPI).

## 4.6 Limitations

To correctly interpret the simulation results, we must be aware of the methodology and limitations of the RAGE code. For example, by solving the Euler equations RAGE neglects physical viscosity and heat conduction in all calculations. Molecular diffusion is also not modeled in the code. These neglected quantities, along with numerical diffusion and artificial viscosity, will affect the development of the cylinder and need to be recognized when analyzing the computational results. Work is presently being performed to implement a mix model in the RAGE code [53]. The mix model will allow us to examine the possible role of turbulent mixing on the cylinder evolution.

To help understand the limitations of the RAGE code, we are running the current problem with other codes, which employ different numerical methods, solve the Naiver-Stokes equations, and/or contain a mix model. These computational results are being compared with experimental data and RAGE simulations results. We note that code-to-code comparisons also play a role in the RAGE code validation effort.

# Chapter 5

# Simulation Setup

This chapter describes the setup for the two-dimensional RAGE simulation of a planar Mach 1.2 shock wave interacting with a cylinder of $SF_6$ gas surrounded by air. Included are all the parameters necessary to reproduce this problem with RAGE or with another hydrodynamics code. The simulation models the experimental setup as accurately as possible within the framework of the RAGE code; this allows a close comparison to be made between the experimental data and the computational results.

## 5.1 Material Parameters

The material parameters used for the air and the $SF_6$ gas are given in Table 5.1. Ideal gases are assumed with $\gamma_{air} = 1.4$ and $\gamma_{SF_6} = 1.09$. The pressure is set to the local atmospheric pressure at Los Alamos, which is 0.8

| | Shocked Air | Unshocked Air | Unshocked $SF_6$ |
|---|---|---|---|
| density ($g/cm^3$) | 1.2745 x $10^{-3}$ | 0.95 x $10^{-3}$ | 4.84 x $10^{-3}$ |
| pressure ($dynes/cm^2$) | 1.211 x $10^6$ | 8.0 x $10^5$ | 8.0 x $10^5$ |
| x velocity (cm/s) | 0 | -1.049 x $10^4$ | -1.049 x $10^4$ |
| y velocity (cm/s) | 0 | 0 | 0 |

Table 5.1: Air and $SF_6$ parameters

bar. The densities of the unshocked air and the $SF_6$ gas are set accordingly. We note that the pre-shock Atwood number is equal to 0.6718. The Rankine-Hugnoit relations are used to determine the parameters of the shocked air. The velocities given in Table 5.1 are for the simulation in the "center of mass" frame. In this frame, the cylinder and the surrounding air are initially moving and then become approximately stationary after shock passage. The simulation was run in this frame to reduce the effects of numerical advection that were observed in the laboratory frame of reference. In the laboratory frame, the cylinder is initially stationary and then travels downstream after shock passage.

## 5.2 Zoning

The fine zone size in the simulation is set to equal the pixel resolution of the dynamic CCD camera used in the experiment, which is 0.01 cm/pixel. Note the fine zone size in the simulations of the gas curtain experiments was

0.01125 cm [2]. We set the coarse zone size (level one) to 0.64 cm and allow for seven levels of refinement, which corresponds to a fine zone size of 0.01 cm (i.e., 0.64 cm/$2^6$). The coarse zone size was chosen to obtain at least 10 coarse zones across the width of the computational domain. It was also chosen so that the simulation would run to completion in a reasonable amount of time. The level seven simulations shown in this work took approximately 20-25 hours on eight processors. We note that these simulations produced equivalent results as simulations performed with a uniform fine mesh of 0.01 cm.

### 5.2.1 Convergence

We examine the variation in the height, width, and circulation of the evolving cylinder for four levels of refinement. We consider the fine zone sizes of 0.04 cm, 0.02 cm, 0.01 cm, and 0.005 cm corresponding to levels 5, 6, 7, and 8, respectively. The length and circulation comparison is necessary to show that our calculations are converged for the fine zone size of 0.01 cm. Figure 5.2 shows the height and width of the evolving cylinder measured from the simulations initialized with the image of the experimental initial conditions; this is discussed further in Section 5.4. All simulations were run to a final time of 750 $\mu$s corresponding to the last experimental time. We observe sufficiently small differences in the length measures of the cylinder for levels seven and higher. Differences at late time are due to small scale structures that form on the edges of the cylinder, defining the length measures. Also

in all of the simulations the cylinder "rolls over" around 600 $\mu$s causing the height to increase slower and the width to increase faster than before. This phenomena occurs at slightly different times in the four simulations, creating some variations in the length measures at late time.

The circulation over the lower half of the cylinder for the four levels of refinement is shown in Figure 5.1. We find that the circulation after shock passage differs by less than 1% between two consecutive levels of refinement. This shows that the vorticity deposition due to the shock/cylinder interaction is relatively unaffected by mesh refinement. The late time circulation, which is dependent on the interaction of pressure waves behind the incident shock wave with the evolving cylinder, differs by less than 10% between two consecutive levels of refinement. We assert based on the the above measures of height, width, and circulation that convergence is achieved for our simulations, which have a fine zone size of 0.01 cm.

## 5.3 Computational Domain

### 5.3.1 Domain Size

The size of the computation domain is defined using the dimensions of the shock tube given in Chapter 3. As stated in Chapter 4, the computational domain is dependent on the zoning used in the simulation. Therefore based on the zoning set in the previous section, the length and width of the computational domain must equal some integer multiple of the coarse zone

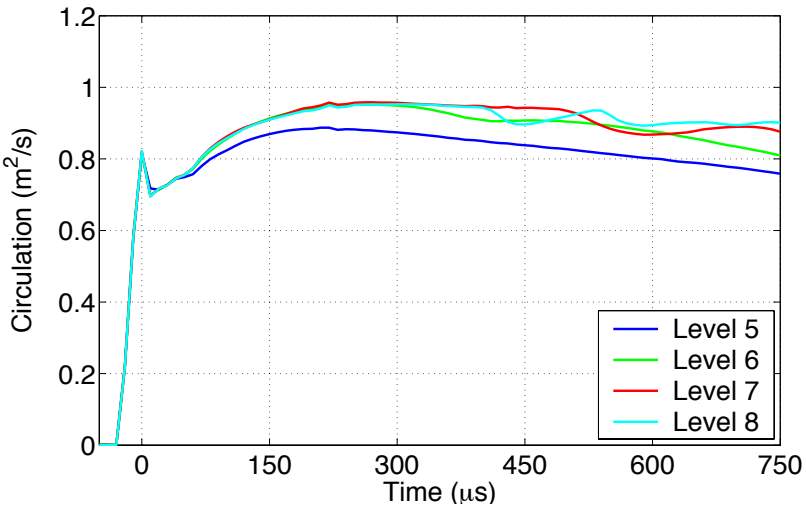


Figure 5.1: Circulation evolution for four levels of refinement

size of 0.64 cm. We set the length to 64 cm and the width to 7.68 cm, which is close to the shock tube width of 7.5 cm. These dimensions result in 12 coarse zones across the width and 100 coarse zones across the length of the computational domain. We place the incident shock front 20 cm from the left boundary of the domain. The cylinder center is located 5 cm to the right of the shock front. Note the shock wave travels from left to right in the simulation.

The large length of the computational domain and the location of the incident shock wave were chosen to prevent the left and right boundaries of the computational domain from influencing the development of the $SF_6$ cylinder. The width of the computational domain was chosen to closely match the width of the actual shock tube. This was necessary because waves reflect off

a)

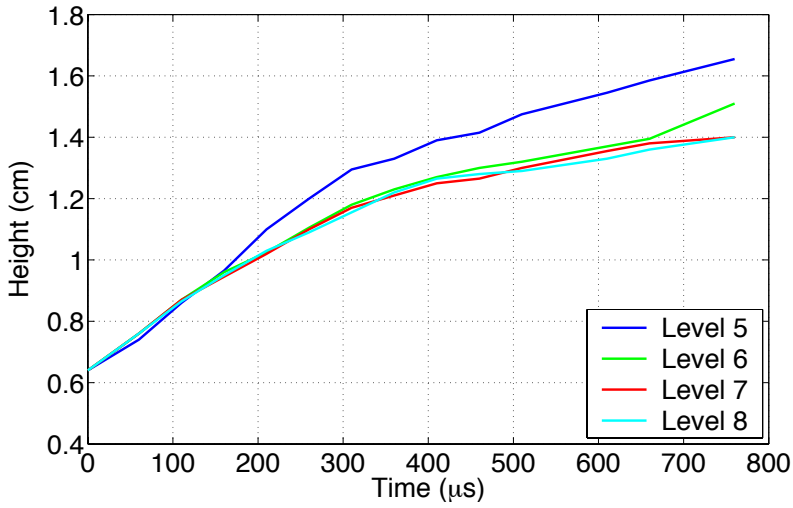


b)

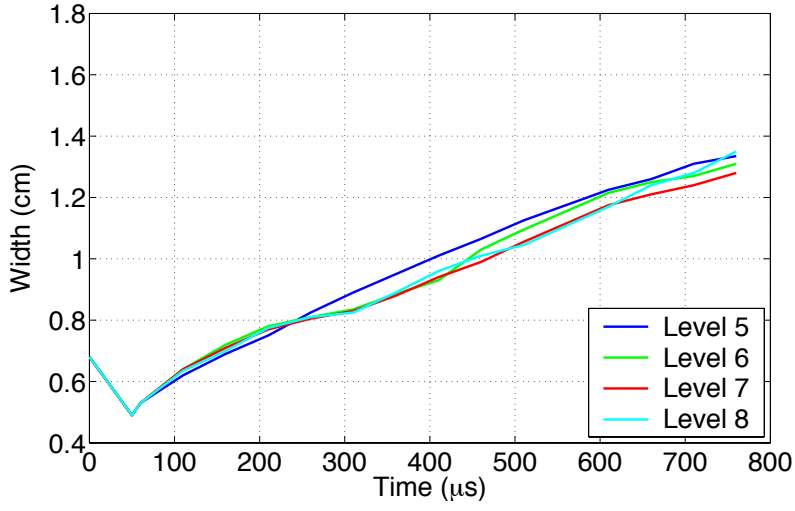


Figure 5.2: Height and width of the evolving cylinder for four levels of refinement

the side walls in the experiment and interact with the evolving cylinder during the experimental observation time. Matching the computational width with the experimental width allows the reflected waves from the side walls to interact with the cylinder at the same time as in the experiment.

### 5.3.2 Boundary Conditions

The boundary conditions are set based on the actual experimental apparatus. Reflected boundary conditions are used for the top and bottom of the computational domain, which models the reflective side walls of the shock tube. An inflow boundary condition is used for the left end of the domain and similarly an outflow boundary condition is used for the right end of the domain. To avoid any adverse effects of the inflow/outflow boundary conditions, we set a large length for the computational domain and locate the shock and cylinder in the middle of this domain. We note that a reflective end wall actually exists in the experiment and is located approximately 80 cm from the $SF_6$ jet. The wall is not modeled in the simulation, since reshock is not examined in this study.

## 5.4 Initial Conditions

The first round of simulations were initialized using a two-dimensional image of the experimental initial conditions. Additional simulations were later performed to test the sensitivity of the computational results to varia-

tions in the peak $SF_6$ concentration and in the initial air/$SF_6$ density gradient. These simulations are discussed in Sections 7.5.1 and 7.5.2.

We obtain a two-dimensional image of the initial conditions from each experiment. The image is rendered to produce location and concentration data that can be imported into the RAGE code. A speckle filter is first applied to the image to eliminate outlying particles caused by noise in the imaging system. The image is then digitalized to create a file containing coordinate values and relative concentration values of the air and the $SF_6$ gas. The concentrations are interpreted as volume fractions and converted into mass fractions using pre-processing software; the mass fractions are then directly imported into the RAGE code.

The image of the experimental initial conditions used in our initial simulation and the corresponding concentration profile is shown in Figure 5.3. The concentration profile is created by taking a horizontal slice through the center of the initial conditions image as shown in Figure 5.3a. The resulting profile in Figure 5.3b shows the presence of asymmetric initial conditions, which is caused by the the lack of a membrane surrounding the $SF_6$ gas jet. Also the imaging technique used in the experiment prevents us from ascertaining the peak $SF_6$ concentration in the initial conditions image. Only the relative intensity of each pixel is known. We initially assume a peak $SF_6$ concentration of 100% in our simulation. The effect of the varying the peak concentration is examined in Section 7.5.1.

a)

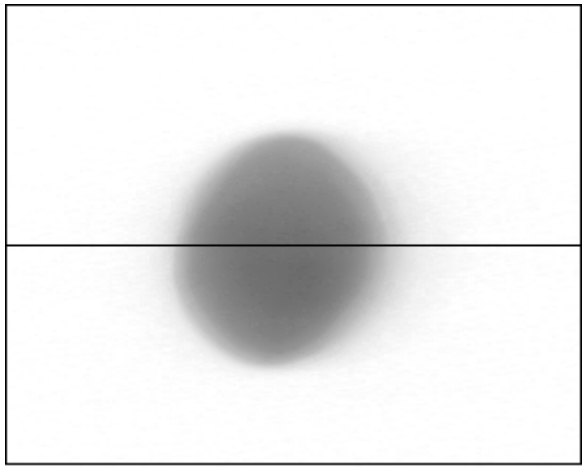

b)

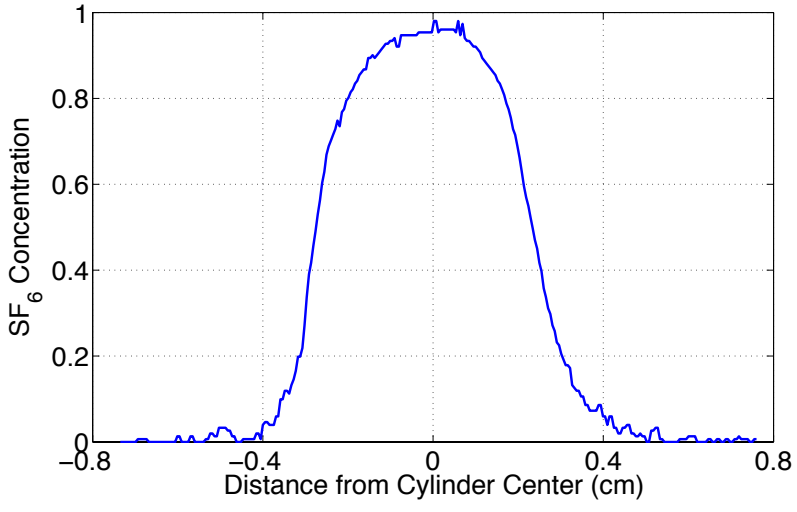


Figure 5.3: a) Image of the experimental initial conditions and b) the corresponding $SF_6$ concentration profile

## 5.5 Initial Grid Refinement

Figure 5.4 shows the initial adapted mesh for the simulation initialized with the experimental initial conditions. The mesh is colored by density to show the location and shape of the initial conditions relative to the location of mesh refinement. Seven levels of refinement are possible in this simulation. Figure 5.4a shows the initial refinement of the shock wave and the $SF_6$ gas cylinder. The seven levels of refinement are observed by the seven different sized square zones. The cylinder and the shock are both refined to the finest zone size as expected. A detailed version of the cylinder refinement is shown in Figure 5.4b. The figure shows a boxed structure surrounding the cylinder that is zoned to the finest level. This zoning is due to the technique in which the experimental initial conditions are imported into RAGE. A rectangular overlay corresponding to the size of the experimental image is constructed. The overlay is then imported into RAGE as a distinct region and placed upon the background region composed of unshocked air. Based on the adaptive mesh refinement conditions, the boundary of the region is zoned to the finest level of refinement.

a)

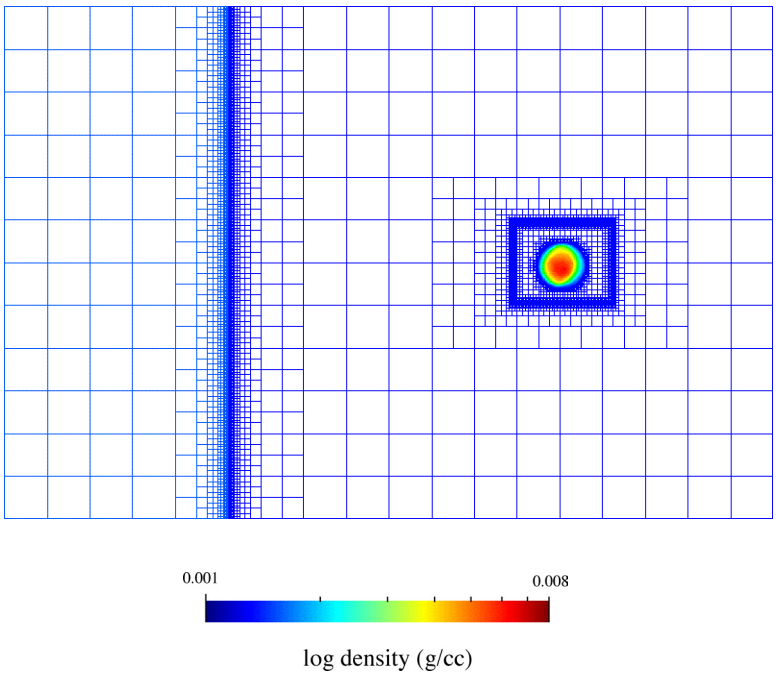


b)

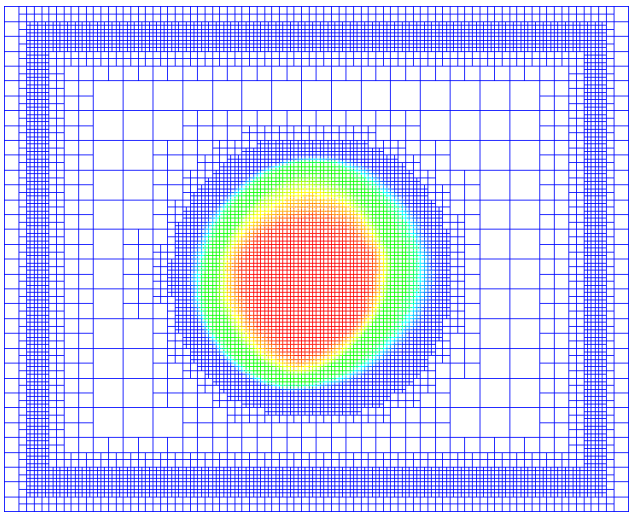

Figure 5.4: a) Initial grid refinement of the shock and the cylinder colored by density and b) a zoomed-in view of the cylinder refinement.

# Chapter 6

# Shocked Cylinder Evolution

This chapter discusses the interaction of a shock wave with a heavy gas cylinder and the cylinder's subsequent evolution into a vortex pair. The shock/cylinder interaction is not captured in our experiment, but is key to understanding the late-time evolution of the cylinder. We first discuss vorticity deposition on the cylinder interface and theoretical, computational, and experimental estimates of circulation. Then we use the concept of vorticity to explain the qualitative evolution of the heavy gas cylinder.

## 6.1 Vorticity Deposition

The deposition and evolution of vorticity in a two-dimensional, inviscid, compressible flow is governed by the equation:

$$\frac{\partial \omega}{\partial t} + (\omega \cdot \nabla) V = \frac{\nabla \rho \times \nabla P}{\rho^2} \tag{6.1}$$

where $\omega$ is the vorticity, $\rho$ is the density, $P$ is the pressure, and $V = (u, v)$ is the two-dimensional velocity vector. This equation can also be rewritten in terms of the material derivative, $D/Dt$, such that:

$$\rho \frac{D}{Dt}\left(\frac{\omega}{\rho}\right) = \frac{\nabla\rho \times \nabla P}{\rho^2}. \tag{6.2}$$

We note from this equation that the amount of vorticity generated will be dependent on the baroclinic source term, S, given by:

$$S = \frac{\nabla\rho \times \nabla P}{\rho^2}. \tag{6.3}$$

This expression shows that a misalignment between the density and pressure gradients will generate vorticity.

The generation and evolution of vorticity for the shock-accelerated cylinder problem can be divided into two stages [19]. In the first stage, the interaction of the incident shock wave with the cylinder deposits vorticity on the boundary of the cylinder. In the second stage, secondary vorticity is deposited after shock passage by the interaction of pressure waves behind the incident shock wave with the density gradient of the evolving cylinder. The vorticity evolution in this second stage drives the development of the shock-accelerated cylinder into a vortex pair at late time.

Figure 6.1 shows a schematic adapted from Jacobs [21] of the vorticity production on the boundary of a heavy gas cylinder. Since the heavy gas cylinder is more dense than the surrounding lighter gas, the density gradient is directed radially inward toward the center of the cylinder. The cross product of the density and pressure gradients in the baroclinic source term

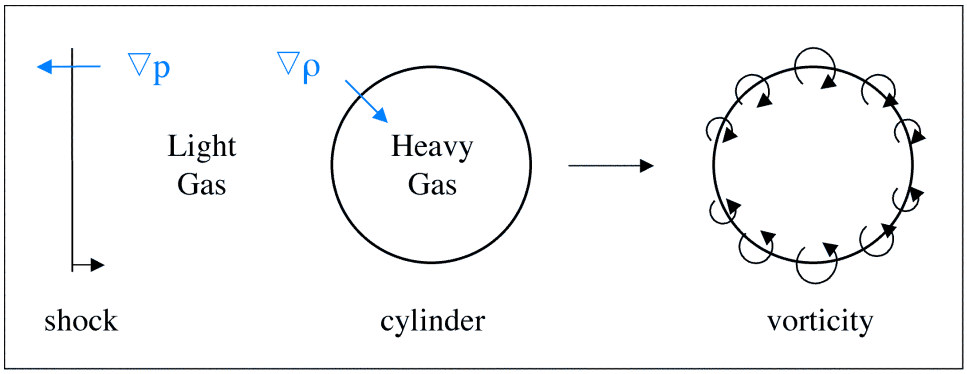


Figure 6.1: Vorticity deposition on a shocked heavy gas cylinder

results in the production of negative vorticity on the upper half of the cylinder and positive vorticity on the lower half of the cylinder. The direction and the size of the arrows in Figure 6.1 represent the direction and the vorticity magnitude, respectively. The largest amount of vorticity is produced at the top and bottom edges of the cylinder, where the pressure and density gradients are most misaligned. No vorticity will be generated at the leftmost or rightmost edge of the cylinder, since here the density and pressures gradients are aligned.

In the RAGE code, vorticity is determined by calculating the curl of the velocity field. This relationship for a two-dimensional flow is:

$$\omega = \nabla \times V = \frac{\partial v}{\partial x} - \frac{\partial u}{\partial y} \tag{6.4}$$

where $V$ is the two-dimensional velocity vector, and $u$ and $v$ are the x and y components of the velocity, respectively. Since vorticity is a derived quantity, its initial value can not be specified directly in the RAGE input file. This

limits our ability to examine vortex flows using the RAGE code.

## 6.2 Circulation

The circulation generated after shock passage is also examined theoretically, computationally, and experimentally. Circulation is a measure of the average vorticity over an area A or equivalently the average velocity around a contour C. Mathematically circulation is defined as:

$$\Gamma(t) = \int_A \omega(t) \cdot dA = \oint_C V(t) \cdot dl \tag{6.5}$$

where $\omega(t)$ and $V(t)$ are the vorticity and velocity, respectively, at time t. Note the circulation calculated over a perfectly symmetric cylinder will be zero, since the cylinder evolves into two vortex cores with equal and opposite vorticity. Without loss of generality we consider the circulation over the lower half of the cylinder, which corresponds to a positive circulation value.

We begin this section by presenting three theories that approximate the amount of circulation produced by the interaction of a planar shock wave with a heavy gas cylinder.

The theoretical expressions are given relative to our study of an $SF_6$ gas cylinder surrounded by air. We note that the three theories only estimate the circulation at the precise time after shock passage i.e., after the first stage of vorticity deposition. We also discuss the calculation of circulation in the experiment and in the simulation. The experimental circulation can only be determined at the last experimental time where velocity measurements are

available. In contrast the computational circulation can be determined over the complete range of experimental times. The theoretical, computational, and experimental circulation values provide us with an additional quantitative measurement to use for comparison in our study. This will be discussed in Section 7.5.3.

### 6.2.1 Theory

#### Rudinger and Somers

Rudinger and Somers considered the impulsive acceleration of an infinite lamina of width $2r_0$, which models the cylinder, and its subsequent evolution into a vortex pair [48]. By matching the impulse and kinetic energy of the impulsively accelerated lamina with the impulse and kinetic energy of a vortex pair, the circulation over the lower vortex core is approximated by:

$$\Gamma = 2ur_0 \left(\frac{\sigma - 1}{\sigma + 1}\right) \tag{6.6}$$

where $u$ is the velocity of the air behind the shock wave, $r_0$ is the initial radius of the cylinder, and:

$$\sigma = \frac{\rho_{SF_6}}{\rho_{air}}. \tag{6.7}$$

This approximation is only valid for weak shock waves and assumes a sharp interface between the cylinder and the surrounding gas.

**Picone et al.**

Picone *et al.* examined the vorticity generation due to the interaction of a weak shock wave with a cylindrical flame [35]. Using the fact that the cylinder evolves into a pair of vortices, the two-dimensional vorticity equation was analytically integrated over the upper half of the bubble and over the elapsed time of the shock/cylinder interaction. The derived expression for the circulation over the lower vortex core is:

$$\Gamma = 2ur_0 \left(1 - \frac{u}{2c_{air}M}\right) ln \left(\frac{\rho_{SF_6}}{\rho_{air}}\right) \tag{6.8}$$

where $u$ is the velocity of the air behind the shock wave, $c_{air}$ is the sound speed of air, $M$ is the Mach number of the incident shock wave, and $r_0$ is the initial radius of the cylinder. This approximation treats the shock wave as a planar discontinuity and does not account for the curvature of the shock wave as it passes through the cylinder. This theory also assumes a weak shock wave and a symmetric gas cylinder with a sharp interface.

**Samtaney and Zabusky**

Samtaney and Zabusky used shock polar analysis to derive an expression for the circulation deposited on a planar interface [49]. These results were generalized for non-planar interfaces, including circular and sinusoidal interfaces. For the cylinder configuration, the circulation is calculated by considering the left and right halves of the shocked cylinder separately. Note for this analysis the shock wave is moving from left to right. The circula-

tion corresponding to the left half of the cylinder is determined by analyzing the generalized result for a fast-slow gas interface, and noting the angle between the shock wave and the cylinder interface ranges from 0 to $\pi/2$. The circulation on the right half of the cylinder is determined by applying the 'near normality hypothesis', which says that "the primary density and pressure gradients are nearly perpendicular to each other" [49] over the right half of the cylinder. Combining these results, the derived expression for the circulation is:

$$\Gamma = ur_0 \left(1 + \frac{\pi}{2}\right) \left(1 - \sqrt{\frac{\rho_{air}}{\rho_{SF_6}}}\right) \left(1 + \frac{2}{M(M+1)}\right) \tag{6.9}$$

where $u$ is the velocity of the air behind the shock wave, $M$ is the Mach number of the incident shock wave, and $r_0$ is the initial radius of the cylinder. This approximation also assumes a weak shock wave and a symmetric gas cylinder with a sharp interface.

### 6.2.2 Simulation

The computational circulation as a function of time, $\Gamma(t)$, is calculated using the relationship between vorticity and circulation. Circulation can be defined as the average vorticity over an area $A$ i.e.,

$$\Gamma(t) = \int_A \omega(t) \cdot dA \tag{6.10}$$

where $\omega(t)$ is the vorticity at time t. For the cylinder configuration, we calculate the vorticity integral over the area enclosed by the contour BCDE,

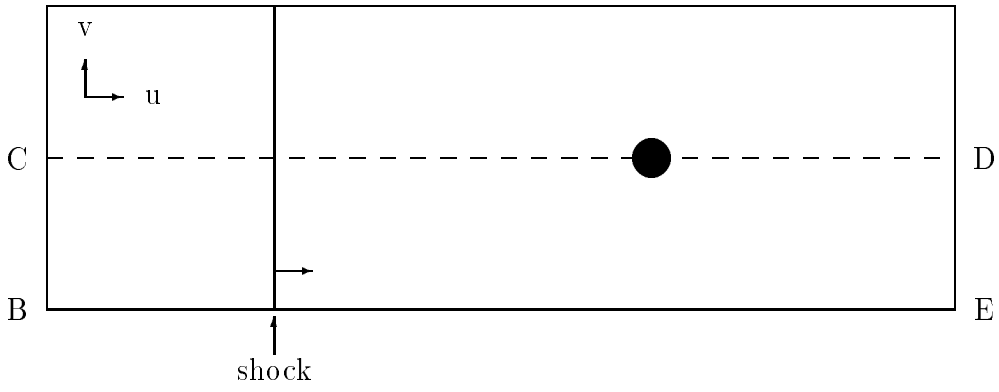


Figure 6.2: Domain used for vorticity calculation

shown in Figure 6.2. The vorticity values are determined by post-processing the SDS files output from the RAGE code. The SDS files contain vorticity values on a uniform mesh; the resolution of the mesh is set in the RAGE input file. Using these values, we calculate the computational circulation by approximating the integral by a summation i.e.,

$$\Gamma(t) = \int_A \omega(t) \cdot dA = \approx \sum_A \omega(x, y, t) \Delta x \Delta y \tag{6.11}$$

where $\Delta x$ and $\Delta y$ are equal to the resolution of the uniform mesh contained in the SDS file.

### 6.2.3 Experiment

Since we only have velocity field data at the last experimental time of 750 $\mu$s, we can only determine the experimental circulation value at this time.

This value can not be compared directly with the theoretical predictions because the theories only predict the circulation value at the precise time after shock passage.

The experimental value of circulation is calculated by first determining the velocity vectors using Particle Image Velocimetry (PIV). Vorticity is then calculated by computing the curl of the velocity field. The vorticity values are subsequently summed over the lower half of the cylinder to determine the circulation. The lower half of the cylinder is used, since the complete upper half of the cylinder is not contained in the PIV image. Note the resulting circulation value is dependent on the resolution of the CCD cameras and the PIV manipulation used to determine the velocity vectors.

## 6.3 Qualitative Early-Time Evolution

Two-dimensional density and vorticity images are presented in Figure 6.3, which show the early-time interaction of a shock wave with a heavy gas cylinder. The heavy gas cylinder is composed of pure gas and forms a sharp interface with the surrounding lighter gas. We assume the heavy gas is $SF_6$ and the surrounding gas is air. The left column of Figure 6.3 shows density images, in which orange corresponds to the $SF_6$ gas cylinder, dark blue to the unshocked air, and turquoise to the shocked air. The shock wave is traveling from left to right in the figure. The right column of Figure 6.3 shows the vorticity for the initial shock/cylinder interaction at the same

times as the density images. Note blue corresponds to negative vorticity and red corresponds to positive vorticity.

The shock/cylinder interaction begins when the planar incident shock wave hits the left edge of the heavy gas cylinder. Figure 6.3a shows the initial conditions prior to shock impact. In Figure 6.3b, we observe the curved reflected shock wave produced at the air/$SF_6$ interface. We also note that part of the incident shock wave diffracts around the cylinder, while the remaining part of the incident shock wave refracts through the cylinder. The diffracted and refracted waves are connected by internal diffracted wave fronts located at the boundary of the cylinder [18]. As seen in Figure 6.3c, the convergent refracted wave travels slower than the diffracted wave, since the cylinder is heavier than the surrounding gas.

The top and bottom parts of the diffracted wave cross at the right edge of the cylinder as shown in Figure 6.3d. A short time later the refracted wave converges to a point, creating a large pressure gradient at the focus of the $SF_6$/air interface. This phenomena is known as shock focusing. At this interface, a radially outward expanding transmitted shock wave and reflected rarefaction wave are produced. The transmitted wave shown in Figure 6.3e eventually catches up to the diffracted wave front, since it has a higher velocity.

As the incident shock wave interacts with the cylinder, vorticity is deposited on the boundary of the cylinder. The right column of Figure 6.3 shows that negative vorticity is deposited on the upper half of the cylinder

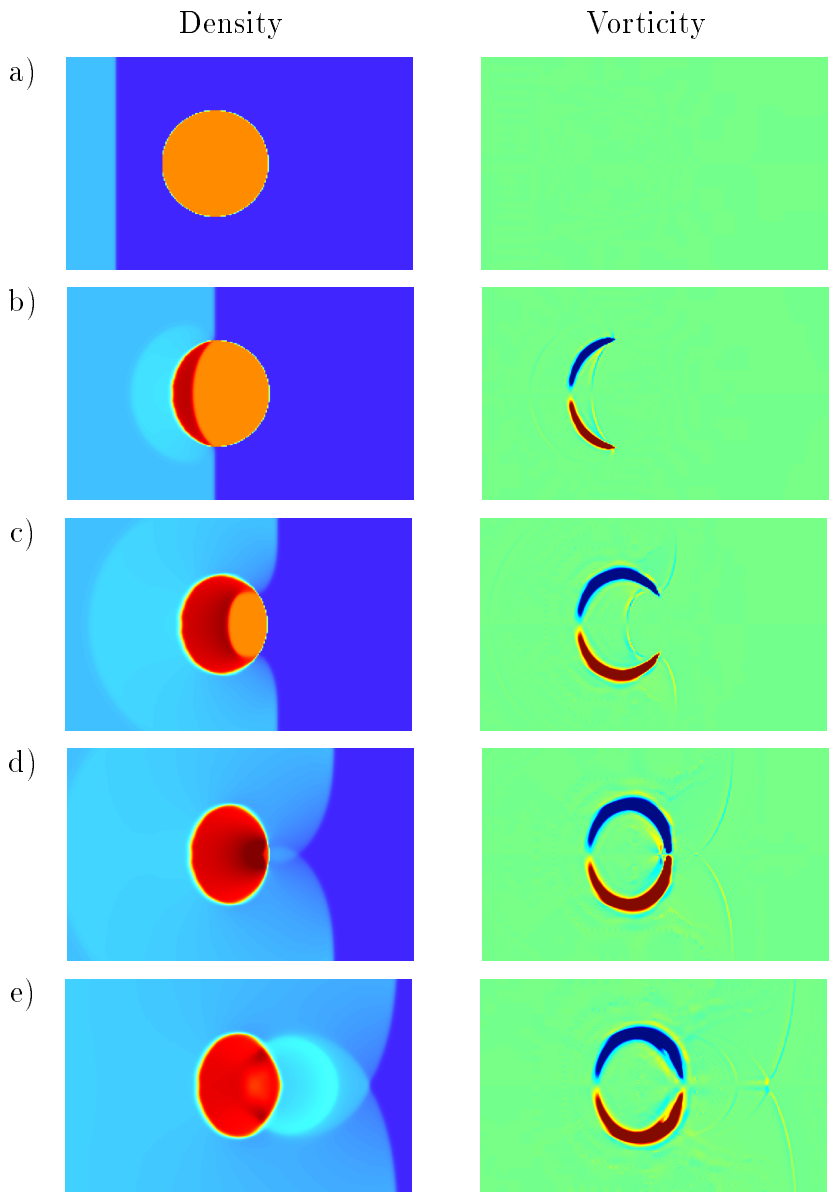


Figure 6.3: Density and vorticity images of the interaction of a shock wave with a heavy gas cylinder at five successive times

and positive vorticity is deposited on the lower half of the cylinder. We note that this is consistent with the baroclinic source term found in Equation 6.1.

## 6.4 Qualitative Late-Time Evolution

Two-dimensional density and vorticity images are presented in Figure 6.4, which show the evolution of the cylinder at late time. Again we assume the heavy gas is $SF_6$ and the surrounding gas is air. The left column of Figure 6.4 shows density images, in which orange corresponds to the $SF_6$ cylinder and turquoise to the shocked air. The right column of Figure 6.4 shows the vorticity at the same times as the density images. Note blue corresponds to negative vorticity and red corresponds to positive vorticity.

The shock-accelerated $SF_6$ gas cylinder evolves into a vortex pair due to the deposition of vorticity on the cylinder interface. As previously discussed the deposition is composed of two stages; the first stage occurs due to the incident shock/cylinder interaction and the second stage occurs due to the interaction of pressure waves behind the incident shock wave with the evolving cylinder. We now examine the evolution that occurs after the first stage of vorticity deposition. Figure 6.4a shows a notch that forms on the downstream edge of the cylinder due to the high velocity produced by shock focussing. In Figure 6.4b, we observe the presence of opposite signed vorticity that forms on the downstream side of the cylinder; this is due to interactions that occur during the second stage of vorticity deposition.

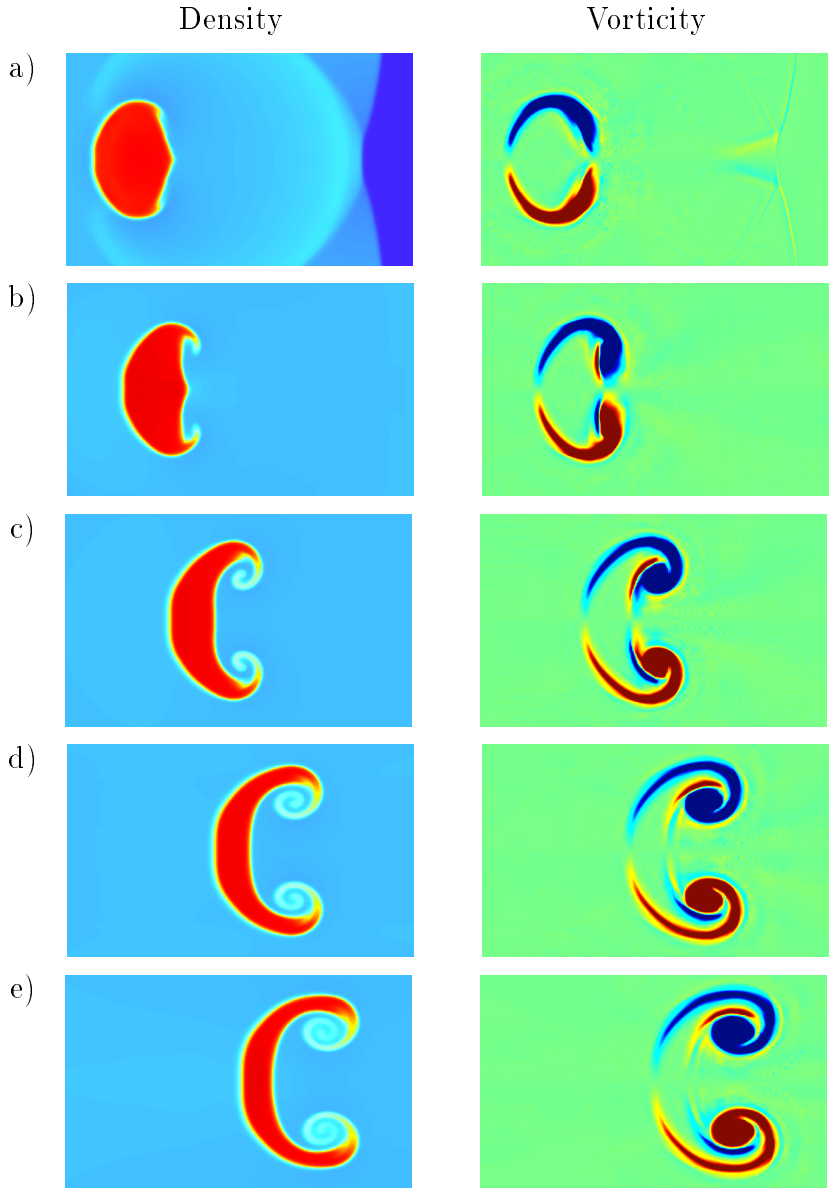


Figure 6.4: Density and vorticity images of the late time evolution of a shock-accelerated heavy gas cylinder at five successive times

By examining the vorticity images, we note that the vorticity is slowly dissipating into the surrounding air. The dissipation rate of vorticity is dependent on the kinematic viscosity of the gas. For example, the kinematic viscosities $\nu$ (defined by $\nu=\mu/\rho$) for $SF_6$ and air are 0.032 $cm^2/s$ and 0.196 $cm^2/s$, respectively. Therefore since the kinematic viscosity of air is greater than the kinematic viscosity of $SF_6$, the vorticity will tend to diffuse into the surrounding air. This phenomena is observed in the vorticity images. Centripetal acceleration has also been cited as another possible reason for the migration of vorticity into the lighter gas [21]. In Figure 6.4c, a vortex double layer [60] is observed in the vorticity plots as the $SF_6$ gas begins to wrap around the vortex core. This vortex double layer persists with time. Figures 6.4d and 6.4e show the continued rollup of the $SF_6$ gas around the vortex core. At late time the evolving cylinder is characterized by a vortex pair.

The variation in the vorticity deposition with time is best observed by examining circulation. Figure 6.5 shows a representative plot of the circulation over time for the lower half of the cylinder. The negative, positive, and total circulation values are all shown. The actual timing and circulation values will be dependent on the radius and density gradient of the heavy gas cylinder, and on the strength of the incident shock wave. The time and circulation values have been normalized, since we are only interested in showing the shape of the circulation curves as the cylinder evolves.

Since we are calculating the circulation over the lower half of the cylin-

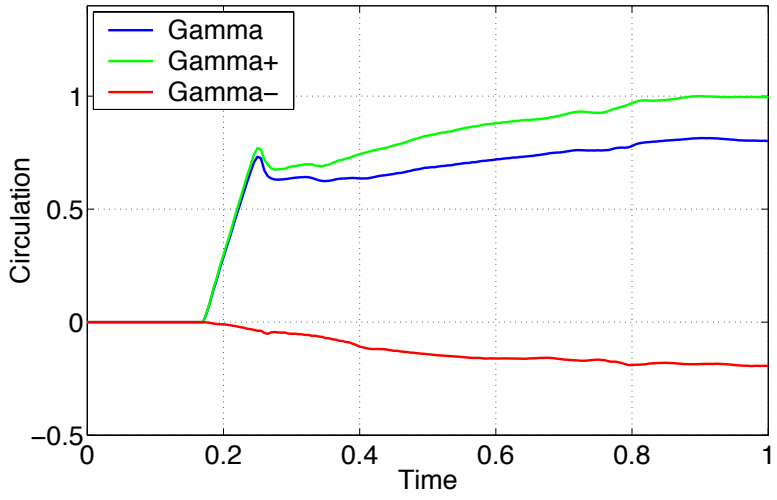


Figure 6.5: Representative plot of circulation versus time

der, the majority of the deposited vorticity is positive. We observe a nearly linear rise in positive circulation due to the interaction of the incident shock wave with the heavy gas cylinder. After the passage of the incident shock wave, small amounts of negative and positive circulation are produced due to the interaction of waves behind the incident shock wave with the evolving cylinder. We note that the maximum negative circulation is approximately 20% of the maximum positive circulation observed in this problem. We also note that at late time the total circulation tends to level out to a constant value as we would expect. We compare theoretical, experimental, and computational circulations in Chapter 7.

## 6.5 Analytical Theory of a Vortex Pair

As in the previous analyses of Rudinger and Somers [48] and Picone and Boris [34], we approximate the cylinder evolution by a vortex pair at late time. This enables us to estimate the relative velocity distribution of the evolving cylinder using an analytical model of a vortex pair. We determine an analytic expression for the center velocity between the two vortex cores. This approximation will help in our comparison of the measured and computed velocities at the last experimental time.

We model the evolving cylinder as a vortex pair composed of two idealized incompressible rectilinear vortices with equal and opposite circulations [37]. A diagram of this configuration is shown in Figure 6.6. The parameter $a$ is equal to the distance between the two vortex cores and $\Gamma$ is equal to the circulation of each vortex. The vortex pair interaction causes each vortex to induce a velocity on the other vortex; this velocity is dependent on the circulation and the distance between the two vortex cores. The induced velocity at each vortex will be:

$$U_{vortex} = \frac{\Gamma}{2\pi a}. \tag{6.12}$$

The velocity at the midpoint between the two vortices can be calculated by determining the contribution of each vortex and then applying the properties of superposition. The velocity between the vortex cores will be equal to:

$$U_{center} = \frac{\Gamma}{2\pi \frac{a}{2}} + \frac{\Gamma}{2\pi \frac{a}{2}} = \frac{2\Gamma}{\pi a}. \tag{6.13}$$

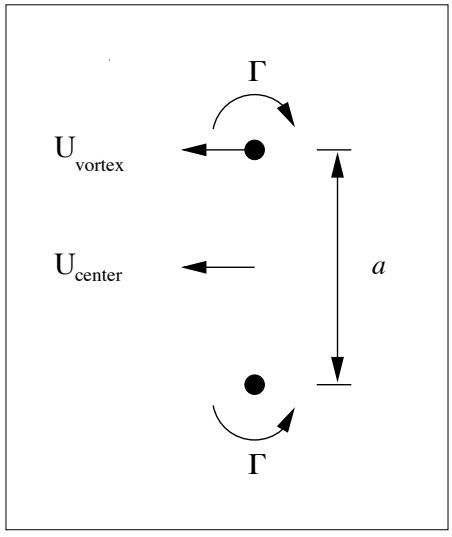


Figure 6.6: Analytic vortex pair model

As will be discussed in Chapter 7, the experiment and computational velocity fields are compared in the rest frame of the vortex core. So for steady state flow, in which the vortices are stationary, the center velocity will be equal to:

$$U_{center} = \frac{3\Gamma}{2\pi a}. \tag{6.14}$$

This expression shows that the center velocity of the vortex pair has a strong dependence on the circulation and the vortex spacing. Since both of these parameters can be determined from the experiment and the simulation, we will compare this analytical expression with the observed computational and experimental center velocities.

# Chapter 7

# Comparison of Experimental Data and Computational Results

We perform simulations of a shock-accelerated heavy gas cylinder using the RAGE code and compare the computational results with experimental data. We discuss the qualitative features of the cylinder evolution observed in the two-dimensional experimental and computational images. Then we compare the simulation to the quantitative measurements of height, width, and vortex spacing recorded at seven times during the experiment. Velocity vectors measured at the last experimental time of 750 $\mu$s are also compared. Our initial investigation uses the image of the experimental initial conditions as the initial conditions in the simulation. A qualitative comparison

of this simulation with the experiment results in good visual agreement, but a quantitative comparison shows considerable disagreement in the velocity magnitudes.

We consider possible computational and experimental causes for the differences. A computational study is performed to examine the effect of varying the initial conditions used in the simulation. Also additional experiments are carried out, in which both the air and $SF_6$ gas are seeded with glycol droplets. These experiments result in higher resolution velocity measurements that turn out to be in better agreement with the computed values. The importance of comparing the measured and computed velocity fields in a systemic manner is also discussed. We present the progression of this study, which has led us to assert that decreasing the peak $SF_6$ concentration and diffusing the air/$SF_6$ interface in the experimental initial conditions lead to better agreement between the measured and computed velocities. This assertion is based on our computational study and on the observation that the $SF_6$ gas diffuses faster than the glycol droplets used to track the gas. Preliminary Rayleigh scattering images of the initial conditions, which directly measure the concentration of $SF_6$ gas, support this claim.

## 7.1 Summary of Comparison

The comparison of the experimental data and the computational results can be divided into three stages. The first stage corresponds to the initial

comparison of the experiment with the RAGE simulation initialized with the image of the experimental initial conditions. The second stage corresponds to the computational study, which examines the effect of variations in the peak $SF_6$ concentration and the air/$SF_6$ gradient in the experiment initial conditions. Also the second stage includes the acquisition of improved velocities in the experiment resulting from higher resolution PIV where both the $SF_6$ gas and the air are seeded. In the third stage the RAGE simulation is initialized based on the findings of the second stage and then the computational results are compared with the improved experimental data.

We summarize our stage one and stage three comparisons of the experimental data with the computational results. A detailed analysis of the stage one comparison is given in Sections 7.2 and 7.3, and a detailed analysis of the stage three comparison is given in Section 7.9. In our stage one comparison, the image of the experimental initial conditions was used to initialize the simulation and a peak $SF_6$ concentration of 100% was assumed. Figures 7.1a and 7.1b show the experimental and computational images, respectively. We achieved qualitative agreement in the large scale structures of the evolving cylinder, although differences existed in the small scale structures. Figure 7.2a shows histograms of the measured and computed velocity magnitudes at 750 $\mu$s. We observed that average peak velocity magnitude was three times larger in the simulation than in the experiment. Also the maximum velocity magnitude in the simulation was approximately five times larger than the maximum velocity magnitude observed in the experiment.

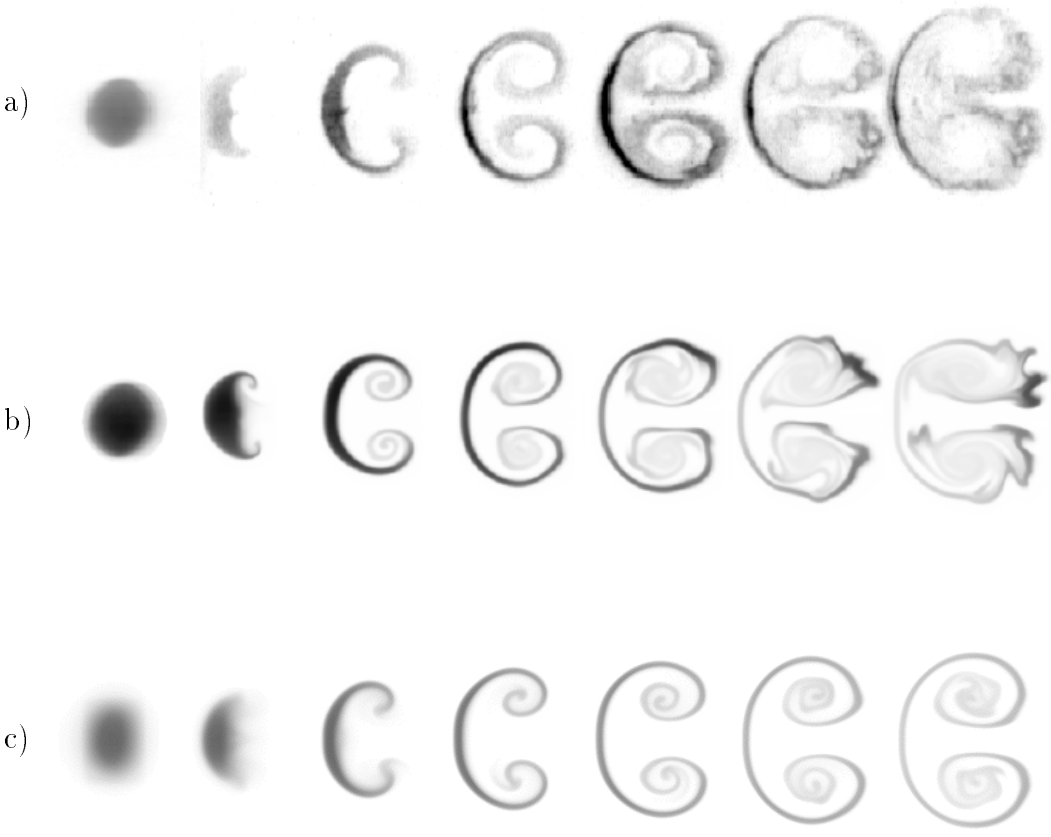


Figure 7.1: Images of the initial conditions and dynamic images at t= 50, 190, 330, 470, 610, and 750 $\mu$s after shock passage for a) the experiment, b) the simulation in stage one, and c) the simulation in stage three

After incorporating the findings of our computational study and making improvements to the experimental diagnostics, we are able to achieve good qualitative and *quantitative* agreement between the experimental data and the computational results. Figure 7.1c shows the stage three computational images at the same times as the other images. Note these results correspond to a different experimental initial condition, but exhibit the same evolution of the cylinder. Again we observe qualitative agreement in the large scale structures of the cylinder. We also achieve agreement with the rate of the vortex roll-up observed in the experimental images, which was not the case previously. Figure 7.2b shows a histogram of the measured and computed velocity magnitudes corresponding to the new computational results and improved experimental data. A larger number of occurrences are observed in the histograms than before because the velocity field is more resolved with high resolution PIV. We note that the histograms are remarkably similar in shape and show good agreement between the measured and computed values. We observe that the average peak velocity magnitude is 3 m/s or 7% larger in the simulation than the experiment. Also the maximum velocity magnitude is only about 4 m/s or 10% larger in the simulation than in the experiment, compared to a difference of 56 m/s observed in the stage one comparison.

In summary, qualitative and quantitative agreement was achieved in stage three based on the following modifications of the experimental initial conditions and improvements in the velocity field comparison:

- Set the peak concentration of $SF_6$ gas in the experimental initial condi-

a)

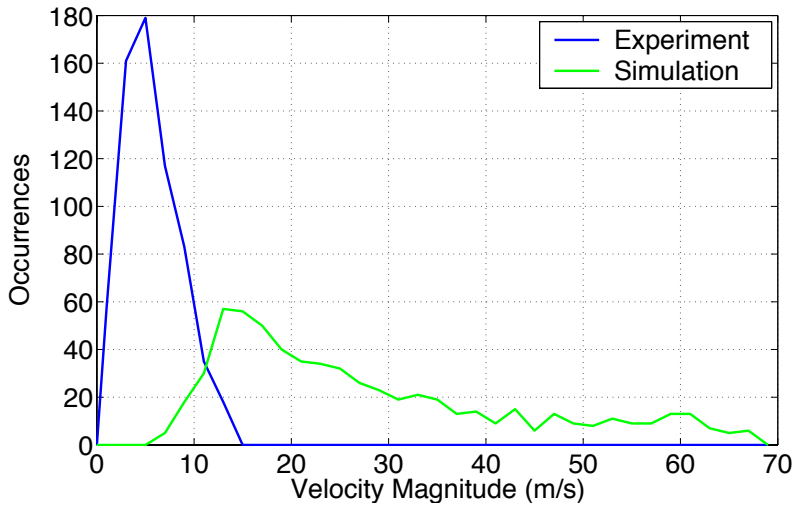


b)

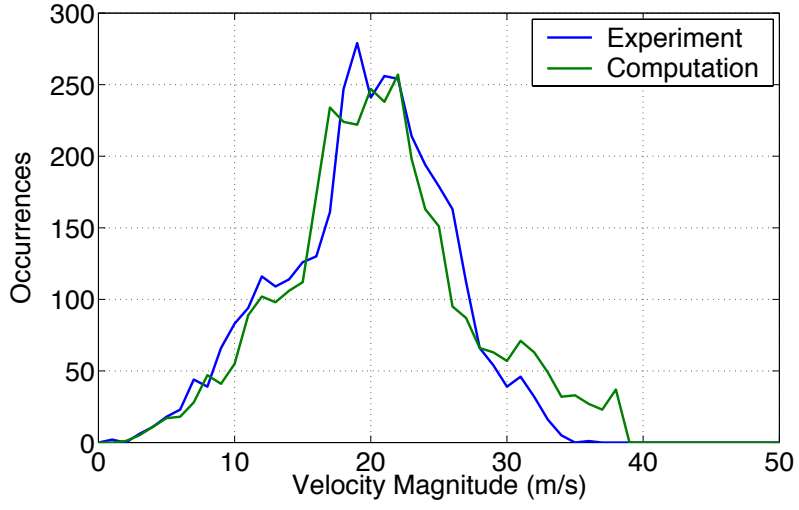


Figure 7.2: Computational and experimental histograms of the velocity magnitudes in a) stage one and b) stage three

tions to 60%, which is consistent with earlier gas curtain experiments

- Diffused the experimental initial conditions to match the dimensions of the first experimental image at 50 $\mu$s
- Obtained larger experimental velocities due to the implementation of high resolution PIV, in which both the $SF_6$ gas and the background air were seeded
- Compared the computed and measured velocities in a consistent frame of reference
- Obtained additional images of the initial $SF_6$ gas cylinder using planar laser Rayleigh scattering, which confirmed the amount of diffusion applied in the simulation.

The remainder of this chapter presents the historical progression, which led us to achieve agreement between the experimental data and the computational results. Sections 7.2 and 7.3 discuss the initial qualitative and quantitative comparisons of the experiment and the simulation. We discuss possible causes of the observed differences in Section 7.4. Section 7.5 presents the computational study that examines the effect of varying the peak $SF_6$ concentration and the air/$SF_6$ gradient in the experimental initial conditions. Section 7.6 discusses the implementation of high resolution PIV, which produces larger experimental velocities. We discuss a better methodology for the comparison of the measured and computed velocity fields in Section 7.7. The

comparison of the improved experimental data and the new computational results that incorporate the findings of the computational study is presented in Sections 7.8 and 7.9. In Section 7.10 we present images of the experimental initial conditions obtained using planar laser Rayleigh scattering, which leads to a better characterization of the initial $SF_6$ gas cylinder.

## 7.2 Initial Qualitative Comparison of Images

As described in Chapter 6, the interaction of an $SF_6$ cylinder with a planar Mach 1.2 shock wave produces strong vorticity that drives the evolution of the cylinder into a vortex pair at late time. This evolution is observed in the experimental and computational images shown in Figures 7.3 and 7.4, respectively. Note the incident shock wave is traveling from left to right in both figures. As discussed in Chapter 3, the experimental images correspond to the concentration of glycol droplets, which track the motion of the $SF_6$ gas. The intensity of each image is dependent on the amount of laser light available during each of the seven laser pulses; we note the amount of laser light is not equivalent for each pulse. Therefore we focus on the structure and the relative intensity of each individual image. For an accurate comparison with the experimental images, the computational images shown correspond to volume fraction, not density. The times specified correspond to the times after the shock has passed through the entire cylinder. The experimental time of the first image, 50 $\mu$s, is determined using fiducials; each subsequent

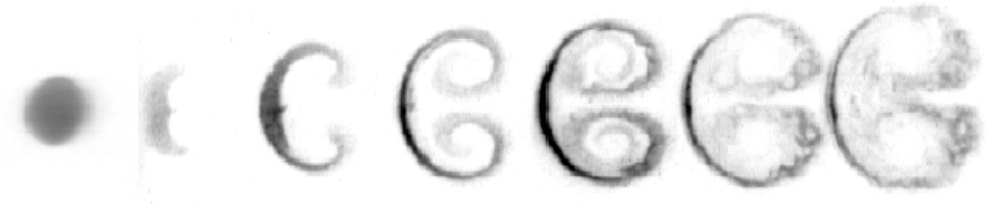

Figure 7.3: Experimental initial conditions and dynamic images at t= 50, 190, 330, 470, 610, and 750 $\mu$s after shock passage

Figure 7.4: Corresponding initial conditions and dynamic images obtained from the simulation

image is separated by 140 $\mu$s. The computational images are at the same times as the experimental images. As discussed in Chapter 5, the image of the experimental initial conditions is used to initialize the simulation, so the first image in Figures 7.3 and 7.4 are the same, although the intensities differ. Assuming that the imported image is a good representation of the actual experimental initial conditions, we expect good agreement to exist between the experimental data and the computational results.

The cylinder's evolution into a vortex pair is evident in both the computational and experimental images. We observe that after shock passage, the compressed cylinder becomes crescent-shaped; this is observed in the first image at 50 $\mu$s. A notch at the center of the downstream edge of the cylinder is also visible in the experimental images, which is caused by the focussing of the incident shock wave at the right edge of the cylinder; this notch is actually observed in the computational images at an earlier time. This observation suggests that the cylinder may be evolving faster in the simulation than in the experiment. As time progresses, the $SF_6$ gas rolls up into spirals due to the vorticity deposition on the cylinder interface. We note that at t=470 $\mu$s the presence of a secondary instability is visible on the downstream edge of the cylinder in both the experimental and computational images. Jacobs observed similar features in his shock tube experiments, which examined the interaction of a Mach 1.095 shock wave with an $SF_6$ gas cylinder [21]. Jacobs speculated that the observed secondary instability is the result of the Rayleigh-Taylor instability, the Kelvin-Helmholtz

instability, or a combination of both.

Although the large scale structures of the experimental and computational images agree, differences exist between the small scale structures. The cylinder in the simulation evolves much faster than in the experiment and exhibits more roll-up inside the vortices. The structure of the secondary instability observed in the computational and experimental images also differs; the instability in experimental images takes the form of small vortices on the downstream edge of the cylinder. The computational images exhibit perturbations inconsistent with the experimental structure. In addition, we note due to the asymmetry present in the experimental initial conditions imported into the simulation, each computed vortex exhibits slightly different structure as time progresses. The effect of the asymmetry is less evident in the experimental images. Even with these variations, a comparison of the large scale structures in the experimental and the computational images results in good qualitative agreement.

## 7.3 Initial Quantitative Comparison

Quantitative measurements allow us to perform a more rigorous comparison than can be made on the basis of a visual inspection of evolutionary images. We compare length measurements of the evolving cylinder at each experimental time and velocity measurements at the last experimental time for the experiment shown in Figure 7.3.

### 7.3.1 Length Measurements

The height and width of the evolving cylinder are measured using the seven experimental and computational images. Note the experimental height and width value are determined from the images obtained from one experiment. We define the height as the vertical length or the spanwise dimension of the evolving cylinder, and likewise the width as the horizontal length or the streamwise dimension of the evolving cylinder. Plots of the height and width are shown in Figure 7.5.

The experimental and computational height and width values at t=0 $\mu$s are equal, since the experimental initial conditions were imported into the simulation. Looking at the other six data points, we find that the height and width are consistently 15% larger in the experiment than in the simulation. Note the error bars for the experimental and computational height and width values are $\pm$ 0.01 cm.

### 7.3.2 Vortex Spacing

We also measure the spacing between the vortex cores in the experiment and the simulation. We assume that the vortex cores are located at the center of the spirals observed in the experimental concentration images. The computational pressure images are used to determine the location of the vortex cores in the simulation. Figure 7.6 shows the vortex spacing of the evolving cylinder. Experimental vortex spacings prior to 330 $\mu$s could not

a)

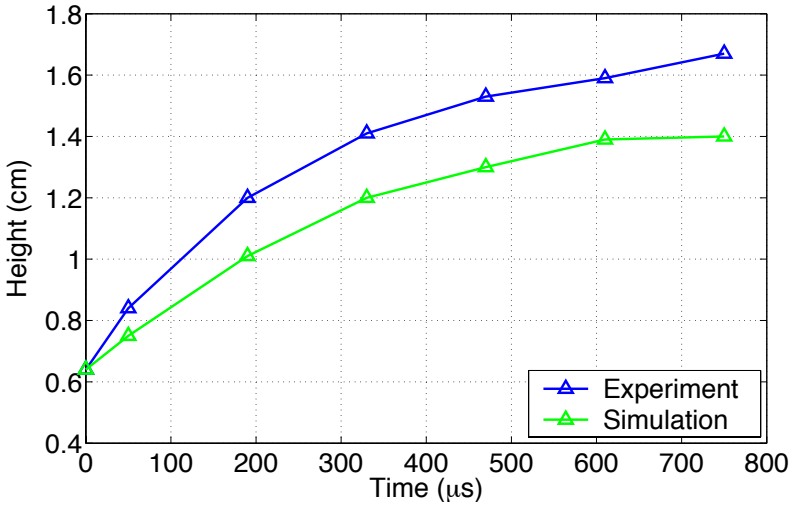


b)

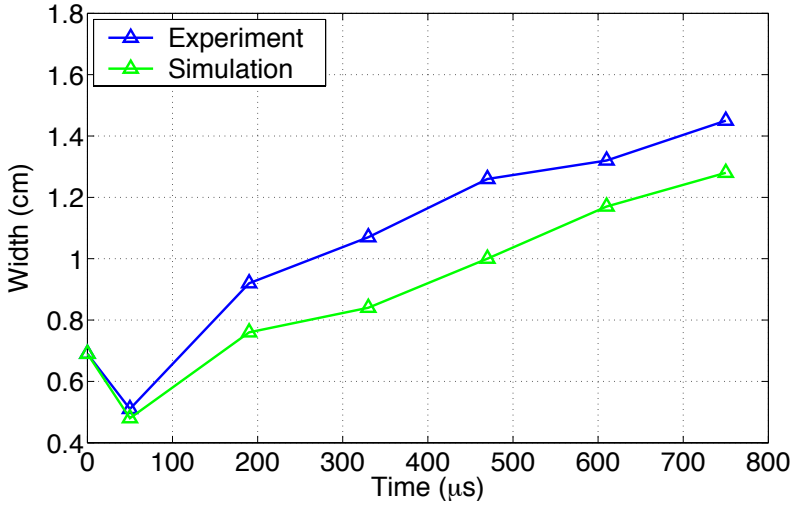


Figure 7.5: a) Height and b) width measurements of the evolving cylinder

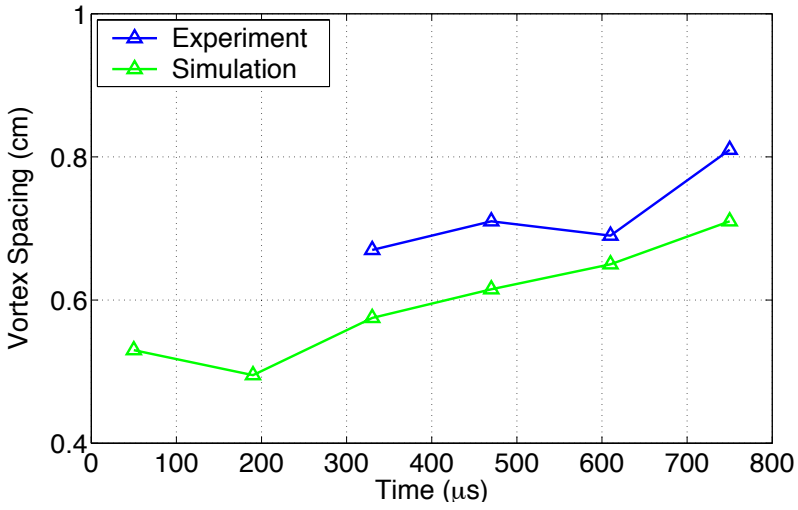


Figure 7.6: Vortex spacing of the evolving cylinder

be determined because the vortex core is not well-defined. We note that the vortex spacings are approximately 15% larger in the experiment, which is consistent with the larger dimensions of the experimental cylinder.

### 7.3.3 Velocity Field

As discussed in Chapter 3, Particle Image Velocimetry (PIV) was implemented in the shock tube experiments to examine the velocities of the shock-accelerated $SF_6$ cylinder. A double-pulsed PIV image at a resolution of 16 $\mu$m/pixel and dimensions 1.4 cm by 1.4 cm is taken 750 $\mu$s after shock passage; this time corresponds to the time of the last dynamic image. The PIV image is interrogated using single-frame cross-correlation [1] to produce

a velocity vector every 537 $\mu$m. This results in a total of 25 velocity vectors in both the x and y coordinate directions. A mean convective velocity of 96 m/s is determined by the cross-correlation software and subtracted from the velocity field. We note this convective velocity corresponds to the mean velocity of the PIV frame, which is not equal to the mean convective velocity of the surrounding air.

Using the RAGE SDS files containing the x and y velocities, we determine the computational velocity field at the same time as the experimental velocity field. We align the left edge of the cylinder and the vertical center of the cylinder with the experimental image to obtain the computational velocity field at the same physical location. Since the computational image has a resolution of 0.01 cm, velocities are averaged to produce a velocity vector every 537 $\mu$m corresponding to the experimental velocity field. Care is taken to reproduce the methodology used in the experimental analysis.

Figure 7.7 shows the measured and computed velocity fields at 750 $\mu$s. Note both of these fields are in the rest frame of the cylinder. The arrow size in the measured velocity field corresponds to 10 m/s and the same arrow size corresponds to 50 m/s in the computed velocity field. The directions of the velocity vectors are similar in both fields, with each exhibiting a large back flow velocity through the center of the cylinder and also the characteristic structure of roll-up inside each vortex core. In addition, we note that in both fields the smallest velocities occur in the vortex core region and the largest velocities occur in the back-flow region.

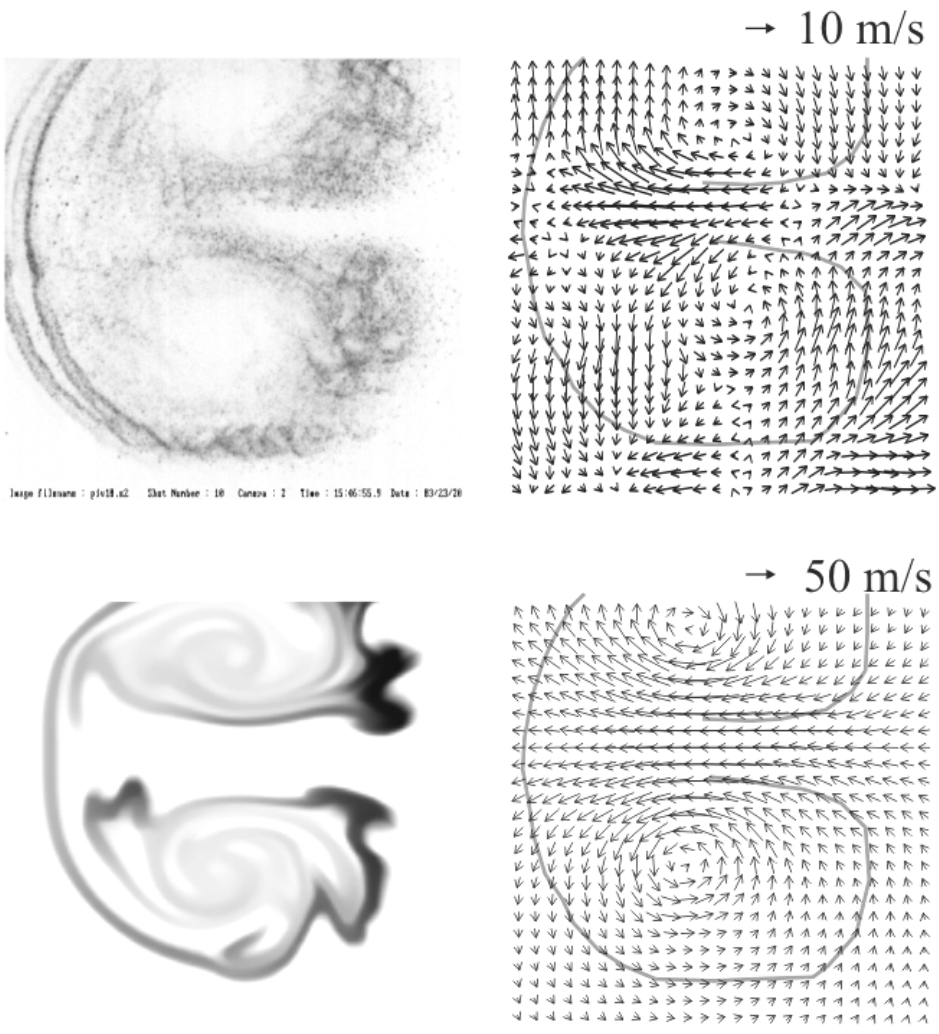


Figure 7.7: Velocity field comparison at t=750 $\mu$s with the experimental field on the top and the computational field on the bottom.

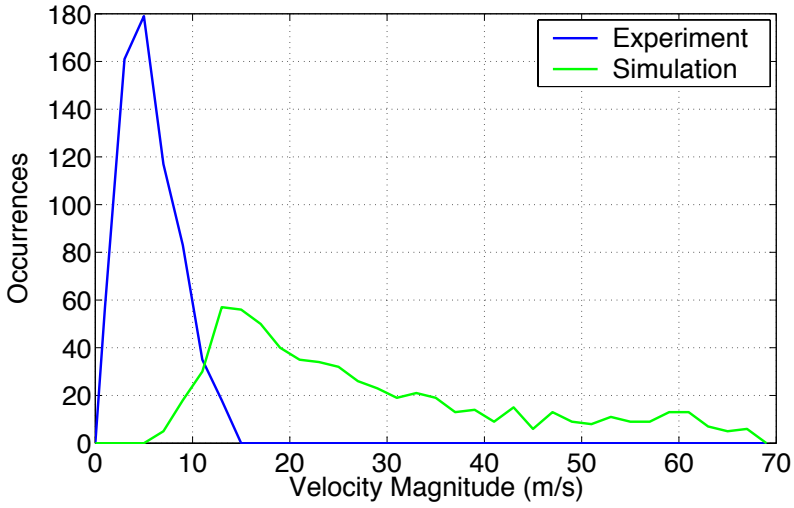


Figure 7.8: Histogram of the velocity magnitudes

A histogram of the velocity magnitudes is shown in Figure 7.8, which quantifies the velocity differences. The histogram shows that the average peak velocity of the experiment is 5 m/s and the average peak velocity of the simulation is approximately 15 m/s, although computed velocities as high as 68 m/s are observed. These high velocities correspond to the back-flow velocities located at the horizontal center of the cylinder. The back-flow velocities are only 12 m/s in the experiment.

### 7.3.4 Cylinder Velocity

The velocities of the large scale features are also examined to verify that the values are similar in the experiment and the simulation. The ve-

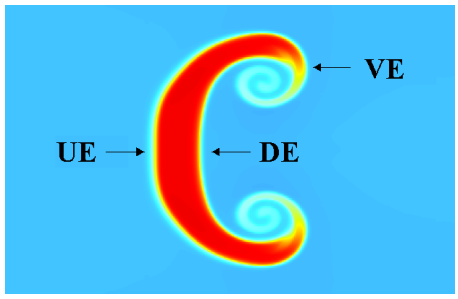


Figure 7.9: Location of the downstream edge (DE), the upstream edge (UE), and the vortex edge (VE) on the evolving cylinder

locities are determined by measuring the distance the feature has travelled downstream between two consecutive evolutionary images. Table 7.1 shows the experimental and computational velocities of the upstream, downstream, and vortex edges of the cylinder, which are defined in Figure 7.9. We observe that the experimental values are approximately 8% larger than the computational values. There are at least two possible causes for the higher velocities observed in the experiment. First, if the Mach number in the experiment is slightly greater than Mach 1.2, the incident shock wave will impart a larger velocity on the $SF_6$ gas cylinder. Second, if the experimental cylinder has a smaller density relative to the computational cylinder i.e., a smaller peak concentration of $SF_6$ gas, it will travel downstream faster than the computational cylinder. We consider these possibilities in our attempt to resolve the differences between the measured and computed velocity values.

| | Experiment | Simulation |
|---|---|---|
| Upstream Edge (m/s) | 85.1 | 78.9 |
| Downstream Edge (m/s) | 81.8 | 76.3 |
| Vortex Edge (m/s) | 96.3 | 90.7 |

Table 7.1: Velocity of the evolving cylinder

## 7.4 Possible Causes of the Differences

The quantitative disagreement between the experiment and the simulation leads us to speculate on possible causes of the differences. Both computational and experiment causes are considered.

### 7.4.1 Computational Causes

The main computational area to examine is the numerical implementation of physics in the RAGE code. It is important to recognize the code's limitations, including neglected quantities and missing physics, so an accurate interpretation of the computational results can be made.

First we examine the assumptions made in the RAGE code. RAGE solves the Euler equations derived from the conservation of mass, momentum, and energy. The effects of heat conduction and physical viscosity are neglected in all calculations. The Euler equations are solved numerically using a directionally-split second-order Godunov scheme. RAGE also does not have the capability to model mass diffusion. We computed the diffusion

length scale for our problem and determined that mass diffusion was not significant during the experimental time of observation.

Another numerical issue concerns the zoning used in this problem. As discussed in Section 5.2.1, a study of mesh refinement was performed to examine the accuracy of the computational results shown in the previous sections. The simulation was performed using a level seven mesh, which corresponds to a fine zone size of 0.01 cm. We observed little difference in the height and width measures of the evolving cylinder for levels seven and higher. Also the circulation after shock passage varied by less than 1% between two consecutive levels of refinement. This shows that the vorticity deposition due to the shock/cylinder interaction is relatively unaffected by mesh refinement. However, the amount of late time circulation will be affected by small scale structures that develop with increasing levels of refinement. In this analysis we found that both the late time circulation and the center velocity between the two vortex cores increased by approximately 10% compared to the previous level of refinement. An increase in these values is expected since more vorticity will be deposited at higher levels of refinement due to the interaction of pressure waves with small scale structures. As discussed in Section 6.5, the observed velocities of a vortex pair are proportional to the circulation and therefore will also increase with higher levels of refinement. Note the fine mesh size of 0.01 cm used in our simulation matches the resolution of the CCD cameras used to acquire the experimental data.

We also performed a simulation to examine the results with a uniform

fine mesh i.e., no adaptive-mesh refinement (AMR). We observed that the cylinder evolution and the quantitative measurements were equivalent to the results obtained with adaptive-mesh refinement. Therefore we have some confidence in the AMR capability implemented in the RAGE code.

There are also some concerns regarding the implementation of the inflow and outflow boundary conditions used in the RAGE code. These boundary conditions are specified for the left and right ends of the domain. To avoid any adverse effects from these boundary conditions, we set a large length for the computational domain and locate the shock and cylinder in the middle of the domain. This prevents reflected waves and the left and right boundary conditions from affecting the evolution of the cylinder.

We must also keep in mind that there will be aspects of nature not captured in the code. Validation efforts are important because they tend to reveal physics that may not be modeled. For example, previous efforts showed the necessity of a mix model and prompted its addition to the RAGE code. We note that this model is still in a prototype stage and is not ready yet for production use. We need to continue to ask the question, what other physics may be missing from the RAGE code?

### 7.4.2 Experimental Causes

To perform a thorough job of code validation, we must also consider experimental causes for the observed differences. Two important issues relate to the implementation of Particle Image Velocimetry (PIV) in the experi-

ment and the limitation of PIV to late time. For the results shown in the previous section, glycol droplets were only added to the $SF_6$ gas. If we examine the experimental velocity field shown in Figure 7.7, we observe some vectors with the wrong direction located at the right edge of the back-flow region and at the bottom middle of the field. These velocity errors occur because few particles exist in areas containing only air, as observed from the PIV image. The sparseness of particles makes large interrogation boxes necessary because eight to ten particles must be contained in a box for accurate cross-correlation to occur. Also the large box size will tend to average out fluctuations in the velocity. This is evident by examining the profile of the velocity magnitude histogram shown in Figure 7.8, which exhibits a sharp drop off in the occurrences of high velocities. Based on these issues, improvements were made to the PIV implementation in the experiment, allowing us to obtain a higher resolution velocity field in which the air velocity is also measured. The effect of these improvements is discussed in Section 7.6.

Presently, velocity measurements can only be acquired at late time. We believe that much insight into the velocity differences could be gained by performing PIV at early time, but unfortunately we are restricted by the shock tube configuration. Early time PIV would require a redesign of the shock tube to enable the PIV camera to obtain an unobstructed view of the cylinder. Also since the glycol droplets would tend to be clumped together at early time, we would need to consider ways, such as using a background seeding, to distinguish groups of particles. Early time PIV will be a future

capability of this shock tube.

There are also some concerns regarding the characterization of the initial conditions. These concerns are prompted by the asymmetry observed in the experimental initial conditions and the lack of asymmetry observed in the corresponding experimental images. The evidence of qualitative differences between the experimental and computational images also raise some questions, particularly regarding the peak $SF_6$ concentration and the air/$SF_6$ gradient in the initial conditions. With the present imaging technique we are unable to determine the peak concentration of $SF_6$ gas in the experimental initial conditions. We only know the relative intensity of the pixels in the image. Previous analysis of the gas curtain experiments estimated the peak to correspond to approximately 60% $SF_6$ gas [47]. The simulation shown in the previous sections assumed a peak concentration of 100% $SF_6$ gas. We examine the effect of smaller peak concentrations in Section 7.5.1.

Another concern is that the initial conditions may actually be more diffuse than they appear in the captured image. We know that the $SF_6$ gas will diffuse at a faster rate than the glycol droplets used to track the gas [46]. Therefore the particles imaged may not accurately represent the actual initial conditions of the $SF_6$ cylinder. This also might help to explain the smaller height and width values observed in the simulation, which incorporated the experimental initial conditions. The effect of diffusion on the cylinder evolution will be examined computationally by examining different density gradients at the air/$SF_6$ interface. This is discussed in Section

7.5.2. We also obtain new images of the experimental initial conditions as discussed in Section 7.10, which support the claim that the initial conditions are actually more diffuse than imaged.

There is also the possibility that there are aspects of the experiment that we do not completely understand. This is based on the previous shock-accelerated $SF_6$ gas cylinder experiments performed by Jacobs [21]. Jacobs imaged the interaction of a Mach 1.095 shock wave with a cylinder of $SF_6$ gas using planar laser induced fluorescence. No velocity measurements were acquired in these experiments. If we compare the images and account for the different Mach number, we find that Jacobs observed more roll-up inside the vortices than seen in our shock tube experiments; his images were more comparable to our computational results. These observed differences may be due to our imaging technique, to variations in the initial conditions observed in each experiment, or to the physical effect of the larger Mach number.

## 7.5 Computational Study

Based on the above discussion, a computational study was performed to try to resolve the quantitative differences observed between the experimental data and the computational results. As discussed in Chapter 6, the vorticity deposition that occurs during the shock/cylinder interaction and the subsequent evolution of the cylinder have a strong dependence on the initial conditions. Therefore we investigate the effect of varying the peak $SF_6$

concentration and the air/$SF_6$ gradient in the experimental initial conditions in the following sections.

### 7.5.1 Effect of Peak Concentration

We first examine the effect of varying the peak $SF_6$ concentration in the experimental initial conditions. As discussed in Section 7.4.2, the peak $SF_6$ concentration is not known with the current imaging system; only the relative intensities are known. Earlier analysis of the gas curtain experiments, which were performed using the same shock tube used here, employed planar laser Rayleigh scattering to acquire an initial conditions image and one dynamic image. With this technique, the peak $SF_6$ concentration was measured to be approximately 40%-60% [7]. A value of 60% was used in a computational study of the gas curtain experiments [2]. Qualitative agreement was achieved between the computational and experimental images of the gas curtain evolution. Due to the new gravity-driven flow system used in this study, we believe the peak concentration in the current experiments may be higher than 60%. We consider 100%, 80%, and 60% for the peak concentration of $SF_6$ gas in the experimental initial conditions.

We study the effect of varying the peak concentration on the qualitative images and on the quantitative measurements examined previously. The images of the evolving cylinder are qualitatively similar for each variation in the peak concentration and therefore not shown. Differences are observed in the quantitative measurements, particularly in the velocity measurements at

the last experimental time. Figure 7.10 shows the height and width of the evolving cylinder. We find that lowering the peak $SF_6$ concentration results in slightly smaller heights and widths. The values actually differ by less than 5% for a change of 20% in the peak concentration. The small variations may be caused by the deposition of smaller amounts of vorticity, which will effect the resulting size of the cylinder.

Figure 7.11 shows a histogram of the velocity magnitudes corresponding to the three peak concentrations. We observe that decreasing the peak concentration results in smaller velocity magnitudes. The most noticeable variation in the velocity corresponds to a decrease in the peak $SF_6$ concentration from 100% to 60%. We find that the peak velocity magnitude shifts from 15 m/s to 10 m/s and the large velocities observed in the back-flow area have decreased from 68 m/s to 55 m/s.

Figure 7.12 shows the circulation versus time for the three different peak $SF_6$ concentrations. The timing is set such that t=0 $\mu$s corresponds to the time when the shock has passed through the entire cylinder. The circulation is calculated over the lower half of the cylinder so the net circulation will be positive. As expected, we find that the circulation values decrease with smaller peak concentrations. We find that decreasing the peak from 100% to 80% results in a decrease of approximately 15% in the circulation. Decreasing the peak from 100% to 60% results in a decrease of approximately 30% in the circulation. We note that the circulation evolution is similar in each case, which shows that the qualitative development of the cylinder does not vary

a)

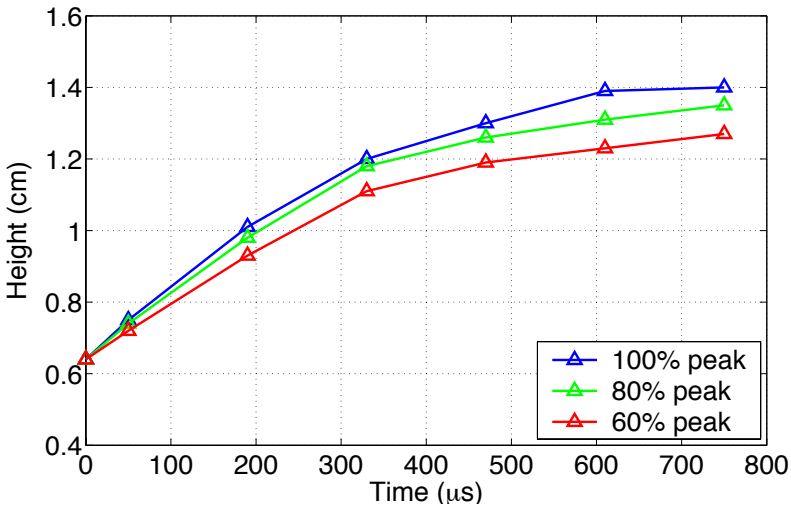


b)

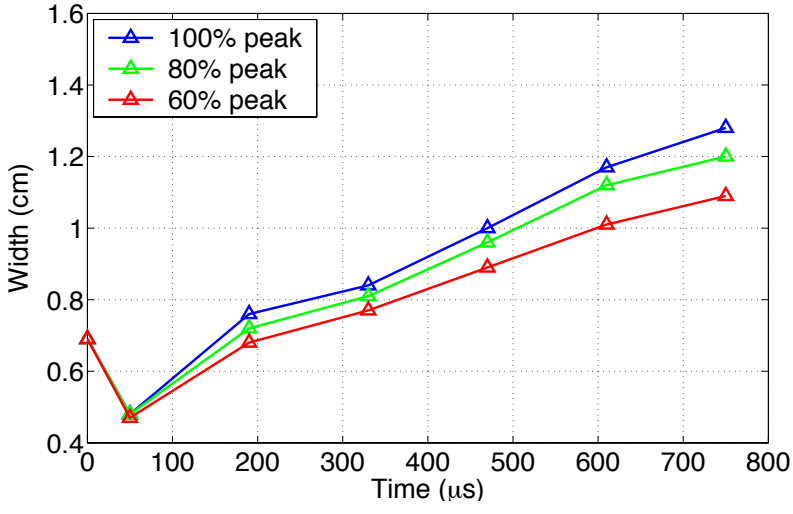


Figure 7.10: a) Height and b) width values for 100%, 80%, and 60% peak $SF_6$ concentrations

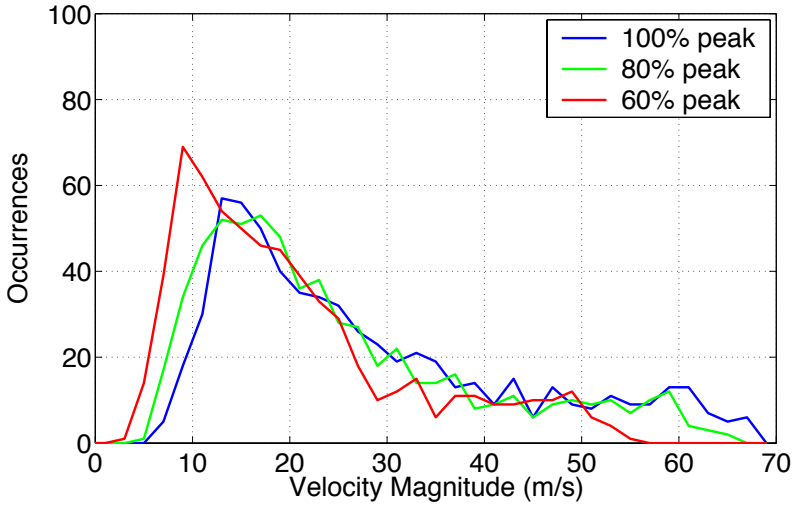


Figure 7.11: Histogram of the velocity magnitudes for 100%, 80%, and 60% peak $SF_6$ concentration

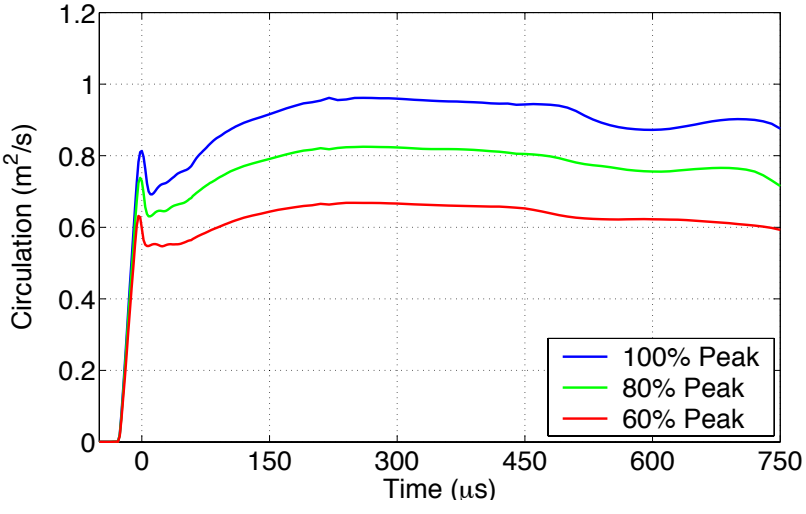


Figure 7.12: Circulation evolution for 100%, 80%, and 60% peak $SF_6$ concentration

much in each of the three cases.

In summary, we observe that decreasing the peak $SF_6$ concentration in the experimental initial conditions leads to smaller velocity magnitudes, caused by a decrease in the vorticity deposition due to the shock/cylinder interaction. For example, decreasing the peak concentration to 60% $SF_6$ gas, which is consistent with previous experimental estimates of the peak concentration, results in a decrease of 15 m/s or 20% in the back-flow velocity and a decrease of 30% in the net circulation value. Therefore an incorrect assumption for the peak concentration is one plausible cause of the observed differences between the measured and the computed velocity magnitudes.

### 7.5.2 Effect of Air/$SF_6$ Density Gradient

We also test the sensitivity of the computational results to the density gradient of the initial conditions. The image of the experimental initial conditions used in our initial simulation is shown in Figure 5.3. The corresponding concentration profile of $SF_6$ gas is determined by taking a horizontal slice through the center of the initial conditions image. The concentration profile has an approximate Gaussian distribution. Note that the concentration drops off sharply at the edges of the cylinder. As will be described in the following sections, we use this concentration profile to derive and examine two additional initial conditions, a sharp interface and a diffuse interface. The initial conditions of all three cases are shown in Figure 7.13.

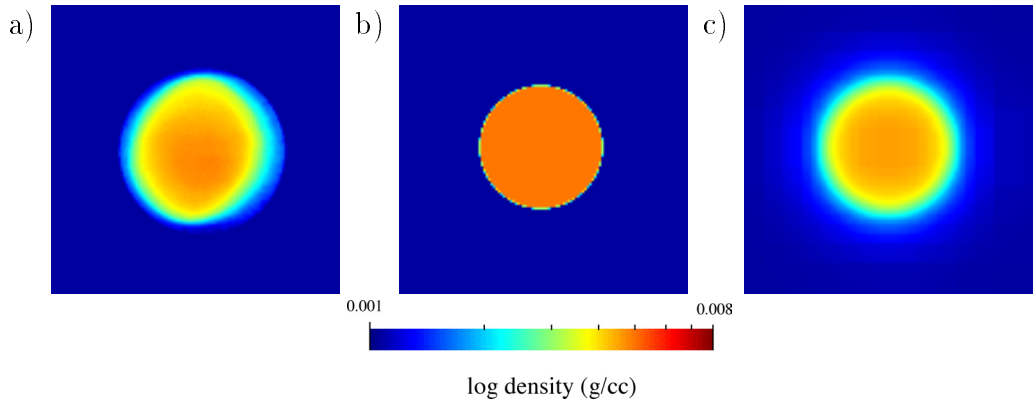


Figure 7.13: Images of the initial conditions for the a) experiment, b) sharp interface, and c) diffuse interface

### Sharp Interface

This simulation considers the effect of a sharp density gradient between the air and the $SF_6$ gas. The diameter of the $SF_6$ cylinder is chosen to equal the length between the 50% concentration levels in the experimental concentration profile shown in Figure 5.3b. The initial conditions are constructed by modeling a perfectly symmetric cylinder of pure $SF_6$ gas surrounded by pure air. No mixed material initially exists in this simulation, except at the boundary between the $SF_6$ gas cylinder and the ambient air.

### Diffuse Interface

The diffuse interface simulation is modeled by computationally approximating the concentration profile shown in Figure 5.3b. A symmetric experimental concentration profile is first constructed by taking the mirror image

of the right side to construct the left side of the profile. The right side is mirrored because the attenuation of laser light through the left side of the cylinder has a small but noticeable effect on the imaging of the initial conditions.

A diffuse initial conditions option was added to the RAGE code for the purpose of this study. The diffusion profile is constructed by specifying the percentage of material to diffuse and the number of diffusion iterations to perform. This procedure models a Gaussian distribution and is dependent on the mesh size specified in the problem. Using one-dimensional RAGE simulations, we iterate until the diffusion profile from the simulation closely matches the experimental concentration profile. In this model, we have initially mixed air and $SF_6$ gas, which more closely resembles the experimental initial conditions. A perfectly symmetric cylinder is also assumed.

### Qualitative and Quantitative Comparison

The resulting computational images for the diffuse and sharp interface simulations are shown in Figures 7.14 and 7.15, respectively. We compare these results with the previous experimental and computational images shown in Figures 7.3 and 7.4, respectively. We observe that the cylinder evolves much faster with an initially sharp interface. The images corresponding to this case are structurally different than the experimental images and the other two computational images at late time. The diffuse interface shows slower development than the sharp interface simulation and is more

Figure 7.14: Corresponding dynamic images obtained from the sharp simulation

Figure 7.15: Corresponding dynamic images obtained from the diffuse simulation

consistent with the evolution observed in the experimental images. It is interesting to note that the initially diffuse interface results in better agreement with the experiment than does the simulation in which the measured experimental initial conditions were imported. This observation gives evidence that the initial $SF_6$ cylinder may be more diffuse than captured in the experimental image.

We examine the quantitative measurements of length and velocity for the three simulations. Figure 7.16 shows little variation in the height and width values for the three simulations. Differences are late time are due to the cylinder "rolling-over" in the image and sharp cases, causing the height to increase slower and the width to increase faster than before. Note this phenomena does not occur in the experimental images or in the diffuse computational images. Figure 7.17 shows the velocity magnitudes for the three simulations. We observe similar values for the back-flow velocities and the peak velocity magnitude in all three cases. There are some variations in the shape of the histograms, which is mainly caused by the different structures observed in the computational images at 750 $\mu$s.

Figure 7.18 shows the circulation versus time for the three simulations. As in the previous section, t=0 $\mu$s corresponds to the time when the shock has passed through the entire cylinder. The circulation is calculated over the lower half of the cylinder producing a net positive circulation. Based on Figure 7.18 we observe that different amounts of circulation occur in each of the three simulations with the diffuse interface having the most and the

sharp interface having the least. We note that in addition to the density gradient, the circulation is dependent on the area of the cylinder. If we examine the height and width plots shown in Figure 7.16, we find that the diffuse interface has the largest dimensions and the sharp interface has the smallest. Therefore based on the density gradient in each case and the area of the initial cylinder, the largest circulation occurs in the diffuse case.

We note that all three simulations reach the same circulation value at t=75 $\mu$s and exhibit a similar circulation evolution. We note a decrease in the circulation for the sharp and image simulations occurring around 525 $\mu$s. This decrease corresponds to the time when the cylinder begins to "roll over", such that the cylinder elongates faster in the streamwise direction, instead of in the spanwise direction observed previously. This evolution creates negative vorticity, which decreases the net circulation. This "roll-over" effect is not observed in the diffuse simulation and therefore the net circulation remains fairly constant.

### 7.5.3 Comparison of Circulation

We also compare the circulation value obtained in the initially sharp interface case with the theoretical estimates given in Chapter 6. We compute the circulation predictions from the theories of Rudinger and Somers (RS), Picone and Boris (PB), and Samtaney and Zabusky (SZ). These theories estimate the circulation of a cylinder with a sharp interface at the time when the shock has completely passed through the cylinder i.e., t= 0 $\mu$s in our

a)

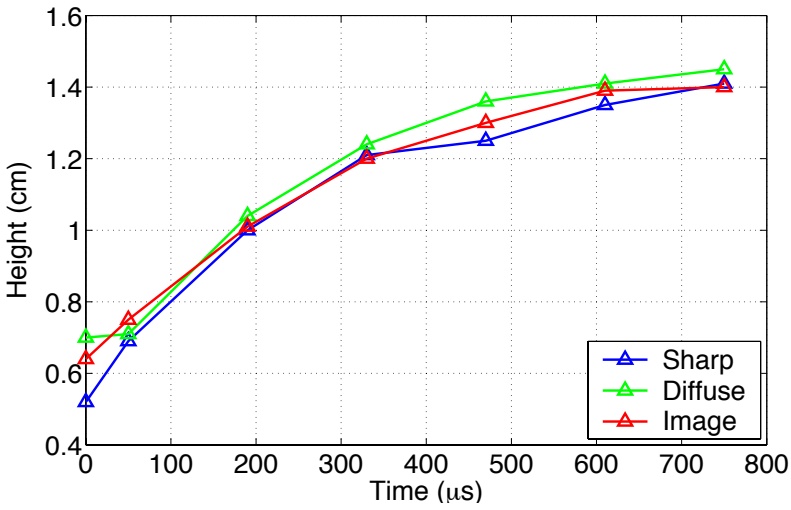


b)

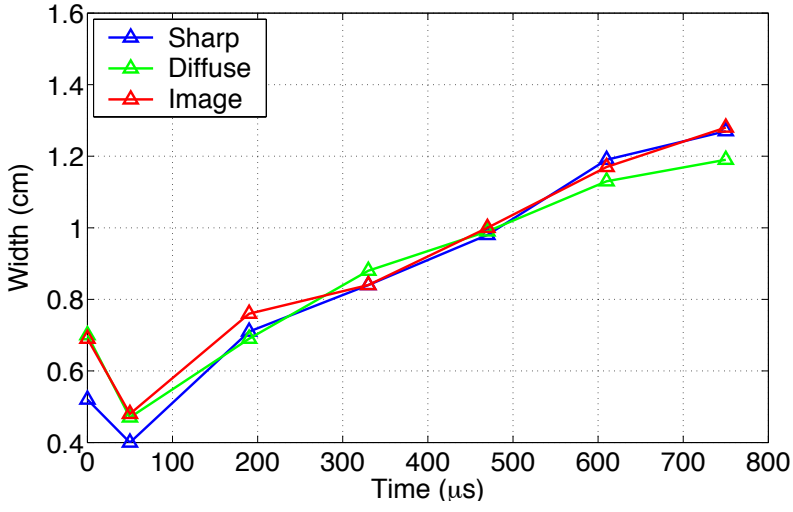


Figure 7.16: a) Height and b) width values for the image, diffuse, and sharp density gradients

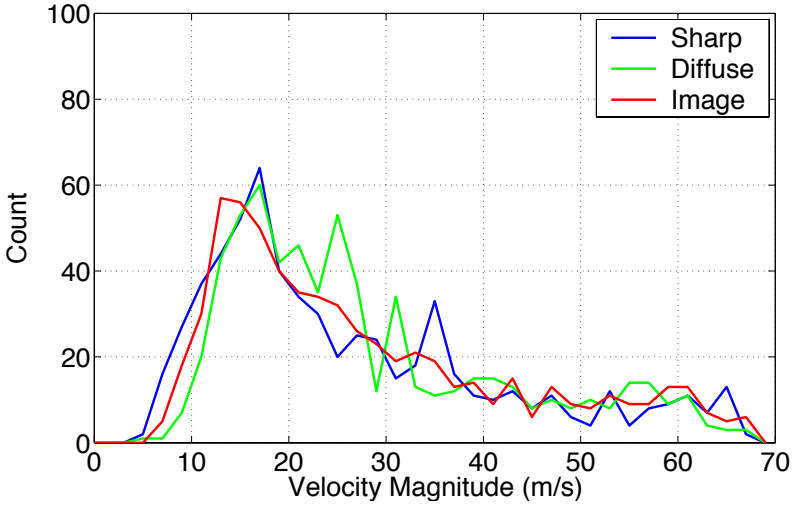


Figure 7.17: Histogram of the velocity magnitudes for image, diffuse, and sharp density gradient

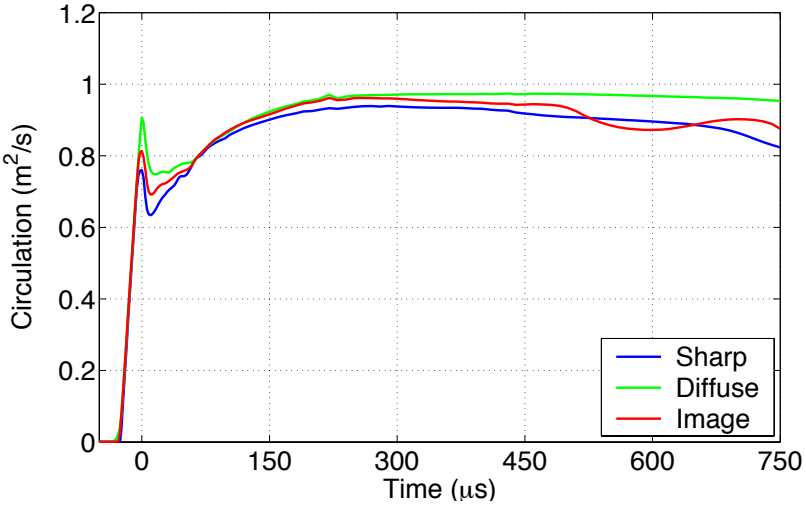


Figure 7.18: Circulation evolution for the image, diffuse, and sharp density gradient

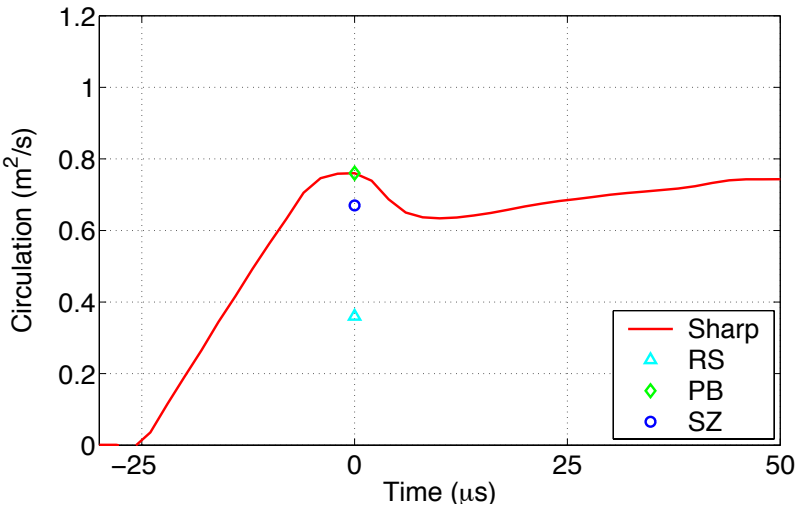


Figure 7.19: Circulation comparison for the sharp interface simulation and the theoretical predictions of Rudinger and Somers (RS), Picone and Boris (PB), and Samtaney and Zabusky (SZ)

timing notation. The simulation models an initially sharp cylinder of radius $r_0 = 0.255$ cm, which corresponds to half the measured length between the 50% concentration levels in the profile of the experimental initial conditions.

Figure 7.19 shows the computational and theoretical estimates of the circulation after shock passage. We observe that the theory of Rudinger and Somers greatly underpredicts the circulation value. The theory of Picone and Boris accurately predicts the amount of circulation, while the theory of Samtaney and Zabusky underpredicts the observed amount by 12%.

These results are consistent with the comparison of simulation and theory presented in Zabusky and Samtaney [49]. Zabusky and Samtaney exam-

ine the same three theoretical predictions for Mach numbers ranging from 1.0 to 2.0 and for density ratios between the cylinder gas and the surrounding gas of 3, 6, and 15. For our case, the density ratio is approximately 5. If we examine their results for Mach 1.2 and for the density ratios of 3 and 6, we observe that our computational results exhibit the same relative agreement with the theoretical predictions. For density ratio of 3, PB and SZ are approximately the same and underpredict the simulation result. For a density ratio of 6, PB slightly overpredicts and SZ slightly underpredicts the computational value. The general agreement between the simulation and the theoretical estimates of Picone and Boris, and Samtaney and Zabusky give us some confidence in the vorticity deposition modeled in the RAGE code.

## 7.6 High-Resolution Particle Image Velocimetry

As a result of the disagreement observed between the measured and computed velocity magnitudes, improvements were made to the implementation of PIV in the shock tube experiments. Table 7.2 summarizes the experimental differences between the old and the new acquisition methods. In the old method, glycol droplets were only added to the $SF_6$ gas. Errors were observed in the resulting velocity field due to the sparseness of droplets in some areas containing $SF_6$ gas. Errors were also observed due to the lack

of droplets in the surrounding air, which prevented velocity measurements in the air itself. In the new method, glycol droplets are added to the background air in addition to the $SF_6$ gas. This enables us to obtain accurate velocity measurements in all areas of the PIV frame. Vector vectors are now obtained every 187 $\mu$m compared to every 537 $\mu$m obtained previously. This increase in resolution is due to both the acquisition of higher resolution imaging cameras and the seeding of the air and $SF_6$ gas, which allow smaller interrogation boxes to be used in the analysis of the PIV frame.

| **Old Method** | **New Method** |
|---|---|
| glycol droplets added to $SF_6$ gas | glycol droplets added to $SF_6$ gas & air |
| 1134 x 468 intensified CCD camera | 1024 x 1024 unintensified CCD camera |
| two images on one frame | two images on separate frames |
| single-frame cross correlation | two-frame cross correlation |
| velocity vectors every 537 $\mu$m | velocity vectors every 187 $\mu$m |

Table 7.2: Differences between the old and new PIV methods

Figures 7.20 and 7.21 show the PIV images used for interrogation in the old and new methods, respectively. The PIV frame shown in Figure 7.20 corresponds to 1134 by 468 pixels with a resolution of 16 $\mu$m/pixel. The PIV frames shown in Figure 7.21 corresponds to 1024 by 1024 pixels with a resolution of 11.7 $\mu$m/pixel. The old PIV method results in a double-pulsed image on one frame, which captures most of the cylinder. Note that no

particles are contained in the air, which corresponds to the black areas in the frame. The new PIV method results in two images each on a separate frame, both of which capture approximately half of the evolved cylinder. We note that different concentrations of particles are visible in the air and in the $SF_6$ gas.

The major drawback of this new method is that we are unable to obtain good quality images of the cylinder evolution, since the laser light scatters off the glycol droplets added to both the $SF_6$ gas and the background air. Previously, the evolutionary images were acquired by the scattering of laser light off the droplets added only to the $SF_6$ gas. Due to the reproducibility of this experiment, this issue is not a major concern. We have observed the same evolution of the cylinder in over 50 experiments. In future experiments we will determine the proper number of droplets to add to the $SF_6$ gas and the air to obtain both evolutionary images and velocity measurements from each experiment.

## 7.7 Frame of Reference

It remains to be determined, how do we compare the computed and measured velocity fields in a systemic manner? We first match the location of the cylinder in the simulated PIV frame with the location in the experimental PIV frame. Recall that the dimensions of the experimental cylinder are larger than the computational cylinder at the last experimental time. Therefore to

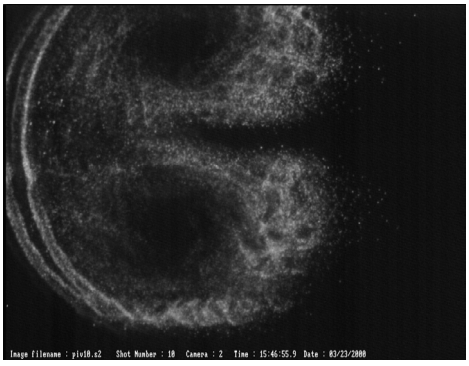

Figure 7.20: Old Method: PIV image used for interrogation

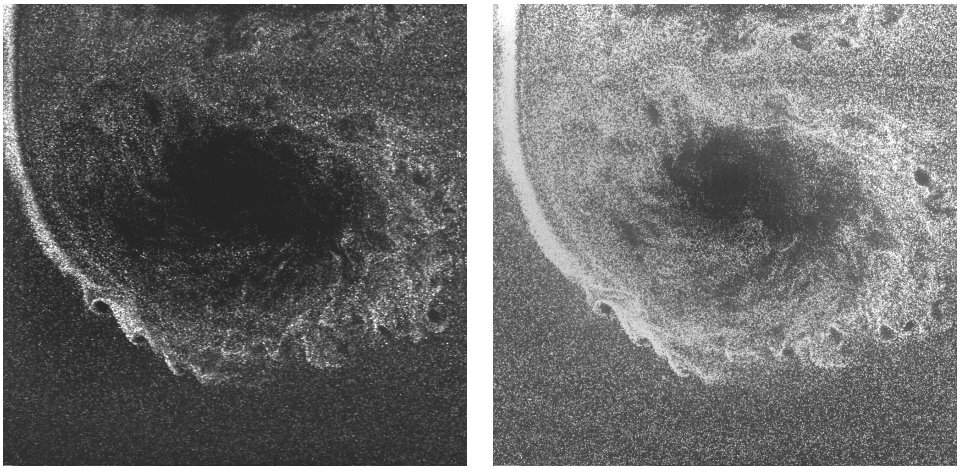

Figure 7.21: New Method: Two PIV images used for interrogation

determine the corresponding simulated PIV frame, we match the upstream edge and the back-flow region of the cylinder with the location of the same features in the experimental PIV frame. This creates a consistent simulated PIV frame, which is independent of the actual size of the cylinder.

We must also account for the fact that the experiment and the simulation are performed in different frames of reference. As explained in Section 5.1, the cylinder evolution in the simulation is examined in the center of mass frame. This means the velocity of the shocked air is approximately zero after the shock/cylinder interaction. The experimental velocities are determined in the center of gravity frame, in which the velocity of the shocked air is approximately 100 m/s. We need to subtract a velocity from the measured field in order to compare it to the computed field. In the previous analysis, the mean convective velocity of the PIV frame was subtracted from the measured velocity field. This value is not equivalent to the mean convective velocity of the surrounding air i.e., subtracting this value does not put the computed and measured velocity fields in the same frame of reference.

Unfortunately, the mean convective velocity of the shocked air in the experiment can not be determined with certainty due to the following reasons. In the simulation, we model a perfect Mach 1.2 shock wave, while an approximate Mach 1.2 shock wave is produced in the experiment. We have no way of accurately measuring the resulting velocity of the shocked air. We note that this velocity can not be determined using the frame captured for PIV analysis. The vortex cores induce a velocity in the air residing close

to the cylinder. Therefore an accurate measurement of the mean convective velocity of the shocked air is not possible using PIV. Another measure must be used.

Based on the discussion in Chapter 6, we know at late time the cylinder evolves into a vortex pair. The analytic vortex model showed that the vortex core and center velocities are directly proportional to the circulation of each core and indirectly proportional to the spacing between the two cores. Therefore any variations in the circulation or vortex spacing between the experiment and the simulation will produce differences in the observed velocities. We choose to set the vortex core as a stationary point in both the computed and measured velocity fields. This allows us to view the velocities in each field relative to a stationary point. We determine the streamwise component of the velocity at the location of the vortex core in both fields. Note the spanwise component of the vortex core velocity is zero. The experimental and computational vortex core velocities are then subtracted from the measured and the computed velocity fields, respectively. This produces a consistent frame of reference, in which the vortex core is stationary in both fields.

The key to this analysis is determining the exact location and velocity of the vortex core. The vortex core velocity can easily be determined in the simulation. Using the computational pressure images, the location of the vortex core is determined. The corresponding streamwise velocity at this point is then subtracted from the computed velocity field. The vortex

core velocity is more difficult to determine in the experiment. First the experimental velocity field is smoothed to dampen any small fluctuations that occur in the field. This procedure makes the location of the vortex core more evident. The location is noted and the streamwise velocity of the vortex core in the actual, not smoothed, velocity field is measured. This value is then subtracted from the measured velocity field.

In summary the following methodology is used to compare the measured and computed velocity fields:

- Match the location of the upstream edge and the back-flow region in the simulated PIV frame with the observed view in the experimental PIV frame.
- Determine the location of the vortex core in the simulation by examining pressure images and in the experiment by applying a smoothing technique to the measured velocity field.
- Determine the streamwise component of the vortex core velocity in both the measured and computed fields.
- Subtract the vortex core velocity from each corresponding velocity field to obtain a frame of reference in which the vortex core is stationary.
- Compare the direction and the magnitude of the velocity vectors in the measured and computed velocity fields.

Recall the initial velocity comparison shown in Figure 7.7. The velocity field corresponding to our initial simulation was computed in the center of mass frame. To accurately compare these results with the new measured velocity fields, we need to subtract the vortex core velocity from the computed field. The streamwise component of the vortex core velocity was measured to be approximately 12 m/s in this simulation. Therefore by changing the frame of reference, we decrease the peak velocities observed in the computed field.

An inconsistent frame of reference in addition to variations in the experimental initial conditions help to explain the quantitative differences observed between the measured and computed velocity fields. Changing the reference frame results in a decrease of 12 m/s or 17% in the computed back-flow velocity. Also decreasing the peak concentration to 60% $SF_6$ gas results in a decrease in the computed back-flow velocity of 17 m/s or 22%. Combining these results we observe a decrease in the computed back-flow velocity of 27 m/s or 39%, which means that the observed back-flow velocity is now approximately 43 m/s. Additional simulations were performed to acquire velocity measurements that incorporate the findings of our study. We present the improved experimental velocity measurements acquired using high-resolution PIV in Section 7.8 and then compare this data with the new computed velocities in Section 7.9.

## 7.8 New Measured Velocity Fields

We examine the measured velocity fields obtained by the new PIV method implemented in the shock tube experiments. The field of view of the experimental PIV frame, the direction and magnitude of the velocity vectors, and the corresponding vorticity field are all determined. Two characteristic data sets corresponding to shots 14 and 16 taken on 10/29/01 are shown in Figures 7.22 and 7.23, respectively. The same shock tube configuration was used to gather data in these experiments. Only the PIV acquisition method was modified.

The experimental PIV frames in Figures 7.22a and 7.23a capture the lower half of the evolved cylinder. Note only one of the two acquired PIV frames is shown. The corresponding velocity fields in Figures 7.22b and 7.23b exhibit the expected direction of the velocity vectors, including a large back-flow velocity in the center of the cylinder and the structure of roll-up inside the vortex core. Larger velocities are obtained with the new PIV method; this is evident by examining the velocity magnitudes shown in Figures 7.22c and 7.23c. The back flow velocity is now approximately 35-40 m/s, compared to 12 m/s measured with the old PIV method. The experimental error bars for the new measured velocity field are $\pm$ 1.5 m/s. Note that high velocities are measured near the top and bottom of the vortex core with the highest velocities occurring in the back-flow region. Also note that the magnitude of the vortex core velocity is approximately zero, since the velocity of the

vortex core has been subtracted from the velocity field. The vorticity fields in Figures 7.22d and 7.23d show the expected positive vortex core and the characteristic vortex double layer that was observed in the computational vorticity fields shown in Section 6.4.

Variations in the shape of the initial conditions lead to differences in the measured velocity and vorticity values. We observe larger velocities in shot 16, especially on the bottom edge of the cylinder where secondary vortices are observed in the corresponding vorticity field. These vortices are less evident in the vorticity field corresponding to shot 14. The main difference between shot 14 and 16 is that the initial conditions for shot 14 are elliptical, while the initial conditions for shot 16 are circular. The correlation between circular initial conditions and the presence of distinct secondary vortices has also been observed in other experiments.

We compare quantitative measurements of the velocities obtained in five different experiments. We subtract the corresponding streamwise component of the vortex core velocity to obtain a consistent frame of reference in each of the five fields. Table 7.3 shows the measured values of the vortex core velocity, the center velocity, and the peak velocity magnitude, which is determined from the histogram of the velocity magnitudes. Notice that there is little variation in the values of the vortex core velocity, implying that the shock speed is fairly consistent in all five experiments. Also note that the value of the center velocity varies between 33 and 41 m/s, which is approximately three times larger than the value obtained previously.

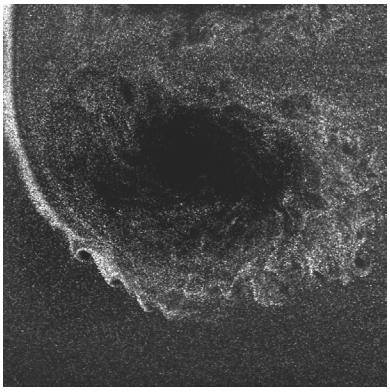

a) PIV Image

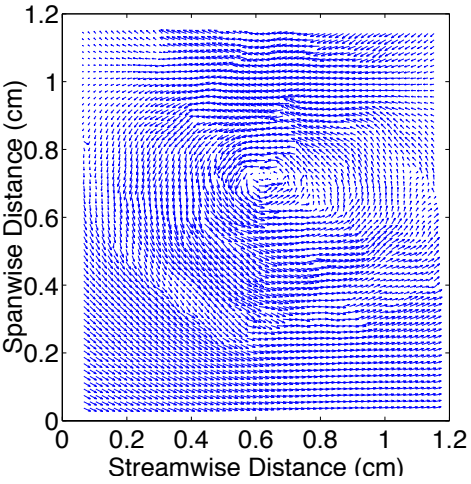


b) Velocity Field

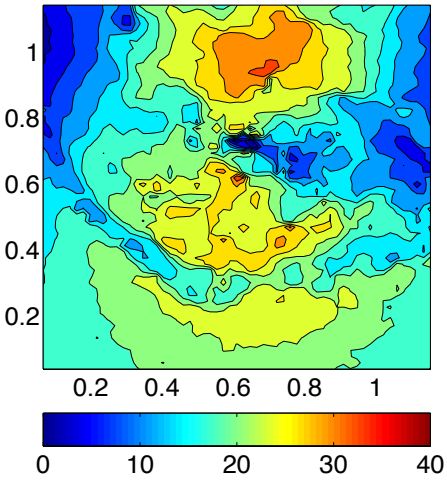


c) Velocity Magnitudes (m/s)

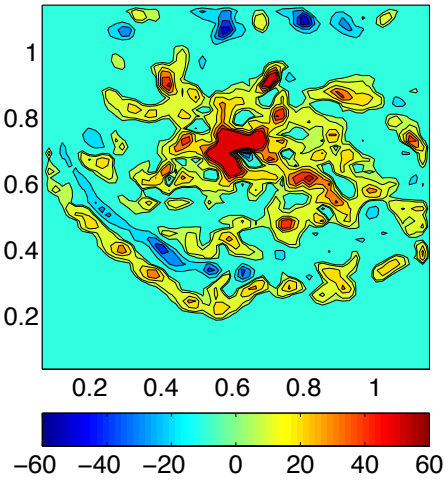


d) Vorticity Values (1/s)

Figure 7.22: Experimental data determined from the PIV image corresponding to shot 14 taken on 10/29/01

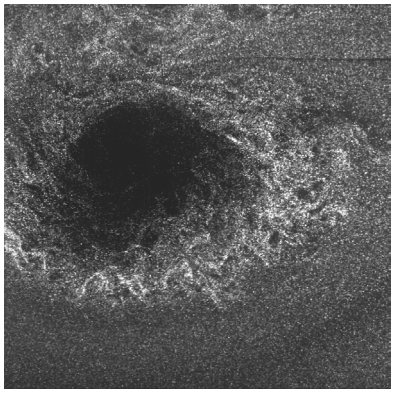

a) PIV Image

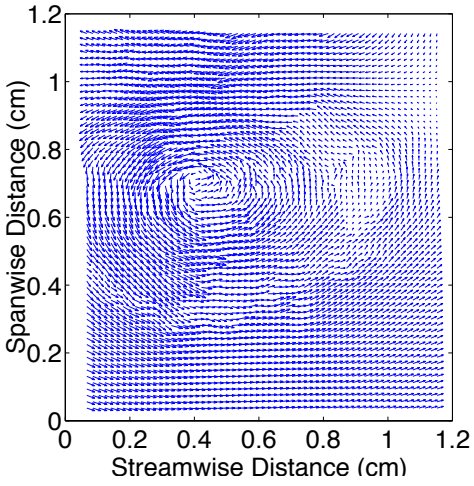


b) Velocity Field

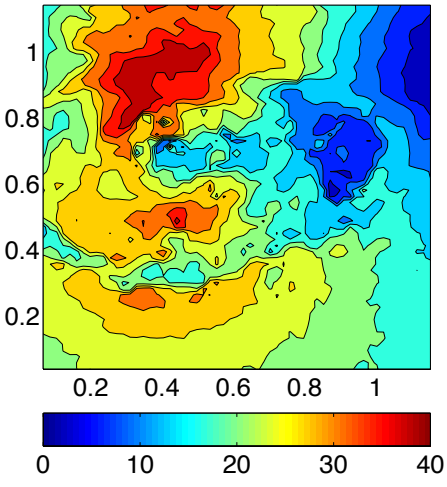


c) Velocity Magnitudes (m/s)

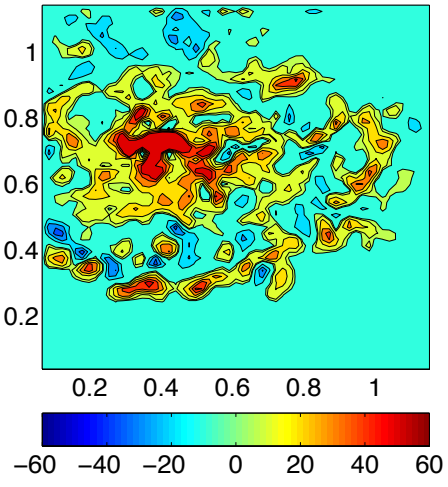


d) Vorticity Values (1/s)

Figure 7.23: Experimental data determined from the PIV image corresponding to shot 16 taken on 10/29/01

| Shot | $U_{core}$ (m/s) | $U_{center}$ (m/s) | $U_{peak}$ (m/s) |
|---|---|---|---|
| 10/29/01 14 | 95 | 34 | 19 |
| 10/29/01 15 | 94 | 33 | 17 |
| 10/29/01 16 | 95 | 41 | 24 |
| 10/29/01 22 | 95 | 40 | 26 |
| 11/29/01 18 | 93 | 38 | 19 |

Table 7.3: Experimental values of the subtracted vortex core velocity, the center velocity between the vortex cores, and the peak velocity magnitude

| Date/Shot | $\Gamma^+$ ($cm^2/s$) | $\Gamma^-$ ($cm^2/s$) | $\Gamma$ ($cm^2/s$) |
|---|---|---|---|
| 10/29/01 14 | 7218 | -1350 | 5868 |
| 10/29/01 15 | 6971 | -1512 | 5460 |
| 10/29/01 16 | 8664 | -1553 | 7111 |
| 10/29/01 22 | 8041 | -1280 | 6761 |
| 11/29/01 18 | 6746 | -1477 | 5269 |

Table 7.4: Experimental values for the positive, negative, and net circulation for the lower half of the cylinder

We also compute the circulation over the lower half of the cylinder in the same five experiments. Table 7.4 shows the measured positive, negative, and net circulation values. Note that these values are measured at the experimental time of 750 $\mu$s, and therefore can not be compared with theoretical predictions. We observe that the maximum negative circulation is approximately 16-22% of the maximum positive circulation. Also we note that the net circulation values range between 5269 and 7111 cm$^2$/s in the five different experiments. We show that these circulation values are related to the observed center velocity in each experiment.

We compare the measured center velocity with the value predicted under the assumption that the cylinder evolves into a vortex pair at late time. As discussed in Section 6.5, the analytic vortex pair model predicts that the center velocity will be equal to:

$$U_{center} = \frac{3\Gamma_{core}}{2\pi a} \tag{7.1}$$

where $\Gamma_{core}$ is the circulation of the vortex core and $a$ is the vertical distance between the two vortex cores. Note that the experimental PIV frame only captures the lower half of the cylinder. Therefore based on the evolutionary images, we assume that the cylinder is symmetric, implying that each vortex core has an equal, but opposite, circulation and that the vertical distance from the center of one vortex core to the back-flow region is equal to $a/2$. Table 7.5 shows the measured values for the parameters $a$ and $\Gamma_{core}$, along with the predicted values of the center velocity. The measured values were

presented in Table 7.3. Good agreement is achieved between the predicted and measured center velocities.

Note that the analytic prediction will be affected by the accuracy of the measurement of the vortex spacing determined from the PIV image and by the definition of the vortex core used to calculate the circulation. The definition of the vortex core region is based on judgement, since the positive vorticity in the core region spreads outward and is not concentrated to a small area. A systemic definition for the vortex core region is used to determine the circulation in all five experiments. The model presented shows the qualitative effect of the vortex spacing and the circulation on the resulting center velocity. For example, shot 18 taken on 11/29/01 has a similar vortex core circulation as shot 14 taken on 10/29/01, but it also has a smaller vortex spacing. Therefore shot 18 has a larger center velocity than does shot 14.

| Shot | a (cm) | $\Gamma_{core}$ ($cm^2/s$) | $U_{center}$(m/s) |
|---|---|---|---|
| 10/29/01 14 | 0.62 | 4476 | 34 |
| 10/29/01 15 | 0.60 | 4052 | 32 |
| 10/29/01 16 | 0.62 | 5336 | 41 |
| 10/29/01 22 | 0.64 | 4999 | 37 |
| 11/29/01 18 | 0.54 | 4472 | 40 |

Table 7.5: Estimated experimental jet velocity using the analytical expression for the velocity between a vortex pair

## 7.9 New Computed Velocity Fields

Images of the experimental initial conditions were obtained for shots 14 and 16 taken on 10/29/01. In both of these experiments, we are able to view the first image of the cylinder evolution before scattered laser light prevents further observation of the $SF_6$ gas cylinder. We use the dimensions of this first image to help construct a modified concentration profile for the experimental initial conditions.

Based on our computational study and on previous analysis of the gas curtain experiments, we believe that the experimental initial conditions are actually more diffuse than imaged and have a peak concentration of 60% $SF_6$ gas. To construct a modified profile in accord with this assertion, we initially import the experimental initial conditions into the simulation and assume a peak concentration of 100% $SF_6$ gas. Then we use the smear routine in RAGE to diffuse the $SF_6$ gas radially outward to produce a concentration profile with a peak concentration of 60% $SF_6$ gas, which also matches the height and width of the cylinder observed in the experimental image at 50 $\mu$s. The measured and modified concentration profiles for shots 14 and 16 are shown in Figure 7.24 and 7.25, respectively. The measured profile is acquired by taking a horizontal slice through the imaged experimental initial conditions and assuming a peak concentration of 60% $SF_6$ gas. This profile has a top hat shape and decreases sharply at the edges of the cylinder. The modified profile has a Gaussian shape and falls off more gradually. In

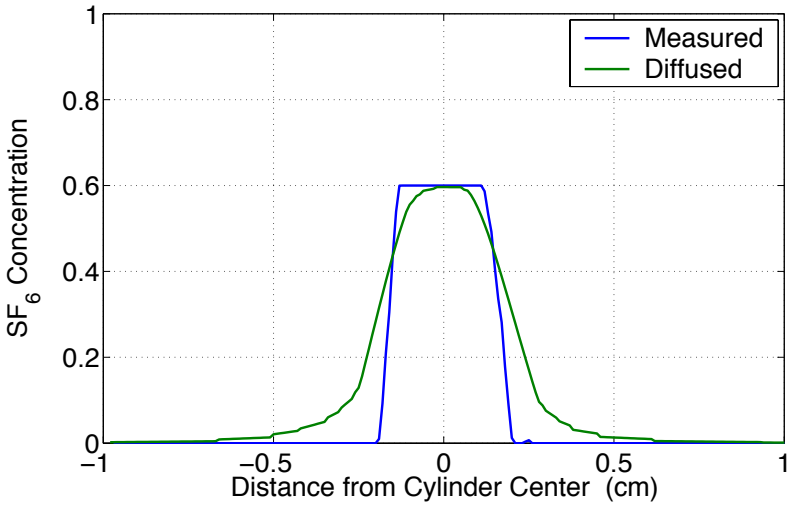


Figure 7.24: Experimental initial conditions for shot 14

Section 7.10 we obtain a better characterization of the experimental initial conditions, which validates the amount of diffusion applied to construct these modified initial conditions.

Using the modified initial conditions, additional simulations were performed using the same setup and resolution as our previous simulations. Since the experiment is reproducible and dynamic images corresponding to shots 14 and 16 are not available, we compare the new computational images with the experimental images in Figure 7.3. The computational images for shot 14 and shot 16 are shown in Figure 7.26 and 7.27, respectively. We obtain good qualitative agreement with large scale structures observed in the experimental images and are also able to reproduce the early-time evolution

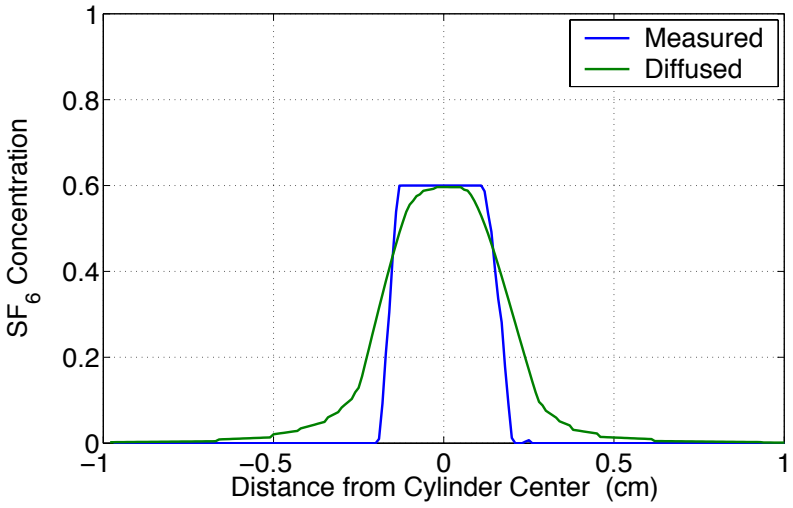


Figure 7.25: Experimental initial conditions for shot 16

of the cylinder. The rate of the vortex core roll-up in the computational images is comparable to the rate observed in the experimental images; this was not the case previously. At late time the large scale structure of the cylinder is reproduced in the computational images, but the small scale structures observed on the edges of the cylinder resulting from a secondary instability are less evident. Higher resolution simulations result in increased detail in the vortex core region, but still do not exhibit small scale structures on the edge of the cylinder. The lack of these small scale structures in the simulation will be investigated in a future study.

We attempt to compare the height and width of the evolving cylinder in the computational images with the height and width observed in the

Figure 7.26: Computational images of the cylinder evolution for shot 14

Figure 7.27: Computational images of the cylinder evolution for shot 16

experimental images. Note that although the cylinder evolution is similar in all experiments, differences do exist in the dimensions of the evolving cylinder due to variations in the initial conditions. Therefore since we do not have an accurate representation of the experimental initial conditions, we can not expect to achieve good agreement with the height and width measured from the experimental images. We do note that the dimensions of the cylinder appear to grow at the same rate, although the actual measured and computed height and width values differ.

The quantitative measurements of velocity and vorticity are also examined at the experimental time of 750 $\mu$s. Figures 7.28 and 7.29 show the

direction and magnitude of the velocity field and the corresponding vorticity field for the simulations of shots 14 and 16, respectively. In the two computed velocity fields initially analyzed in the center of mass frame, the vortex core velocity is approximately 12 m/s. This velocity corresponds to 93 m/s in the center of gravity frame, which is consistent with the observed experimental vortex core velocities given in Figure 7.3 . This implies that the shock speed and the rate of the vortex core roll-up are comparable in the simulation and the experiment.

Figures 7.28a and 7.29a show the simulated PIV frames, which are constructed by matching the location of the left edge and back-flow region of the cylinder with the same features in the corresponding experimental PIV frames. Note that the velocity fields in Figures 7.28b and 7.29b exhibit the expected directions of the velocity vectors. Figures 7.28c and 7.29c, which show the location of the velocity magnitudes, both exhibit a similar distribution of velocities as observed in the corresponding experimental fields. A vertical line-out centered at the vortex core results in a similar velocity magnitude profile in the simulation and in the experiment. The vorticity fields in Figures 7.28d and 7.29d show the characteristic vortex double layer, which was also observed in the measured vorticity fields. The vorticity residing on the bottom edge of the computed cylinder is relatively smooth, showing less evidence of a secondary instability. Note the small scale vortices visible in the measured vorticity fields are not observed in the corresponding computed vorticity fields.

a) Simulated PIV Image

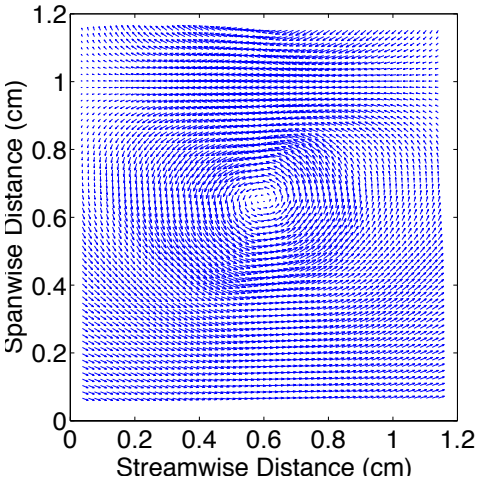


b) Velocity Field

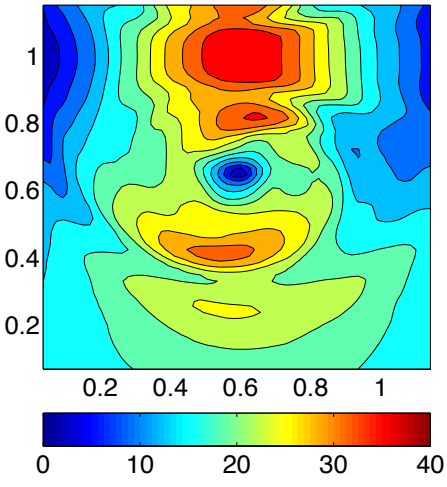


c) Velocity Magnitudes (m/s)

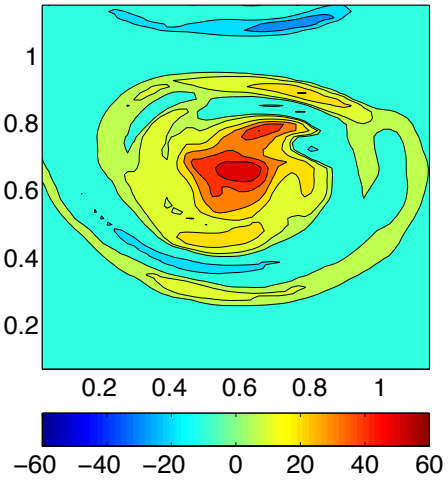


d) Vorticity Values (1/s)

Figure 7.28: Computational results determined using the experimental initial conditions corresponding to shot 14 taken on 10/29/01

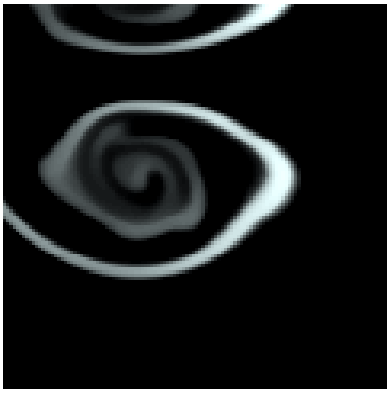

a) Simulated PIV Image

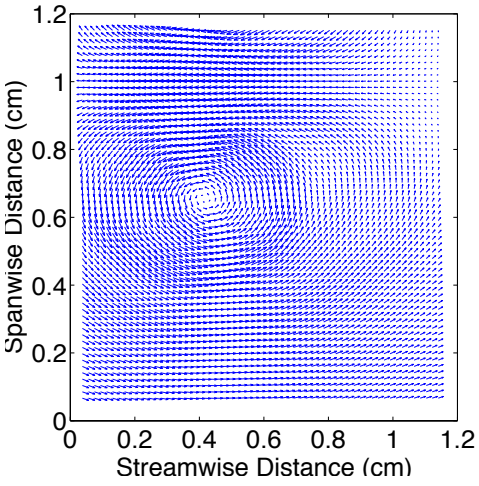


b) Velocity Field

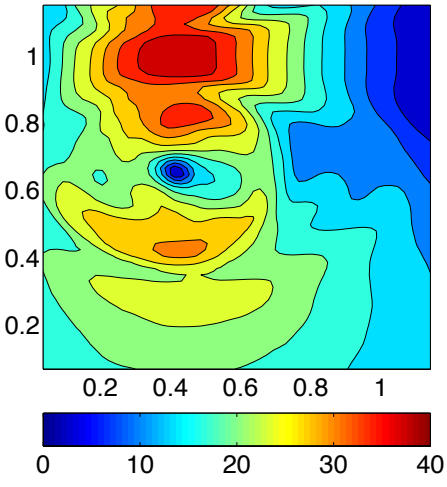


c) Velocity Magnitudes (m/s)

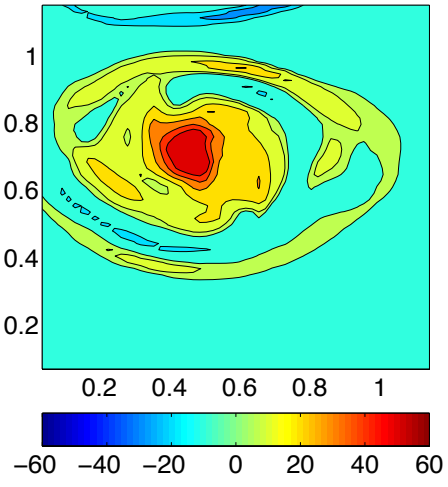


d) Vorticity Values (1/s)

Figure 7.29: Computational results determined using the experimental initial conditions corresponding to shot 16 taken on 10/29/01

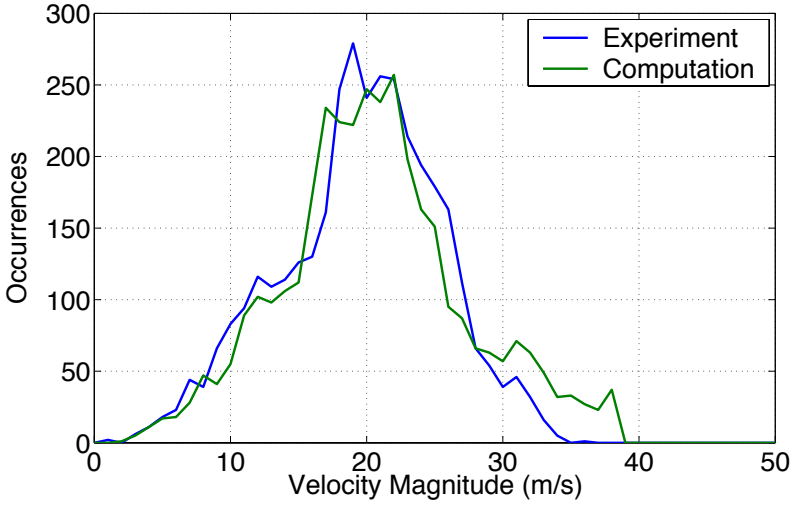


Figure 7.30: Shot 14: Computational and experimental histograms of the velocity magnitudes

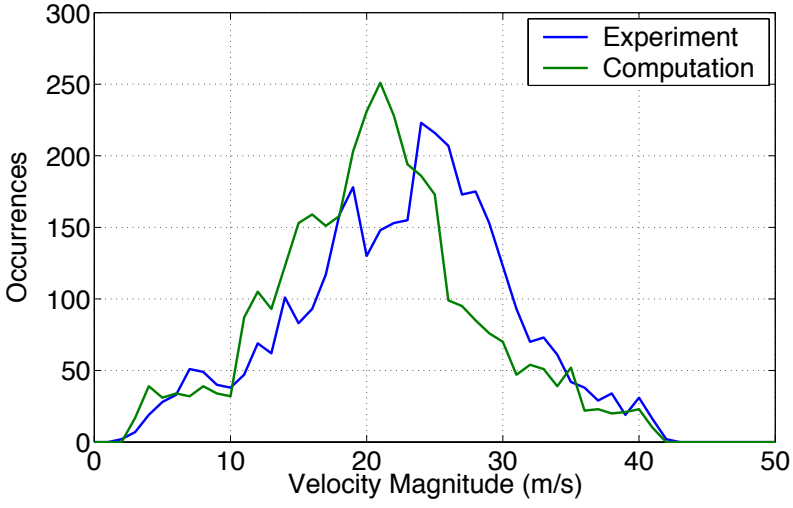


Figure 7.31: Shot 16: Computational and experimental histograms of the velocity magnitudes

| Shot | a (cm) | $\Gamma_{core}$ ($cm^2/s$) | $U_{center}$(m/s) |
|---|---|---|---|
| 10/29/01 14 | 0.66 | 5479 | 40 |
| 10/29/01 16 | 0.66 | 5725 | 41 |

Table 7.6: Estimated computational jet velocity using the analytical expression for the velocity between a vortex pair

Figures 7.30 and 7.31 show the histograms for the measured and computed velocity magnitudes corresponding to shots 14 and 16, respectively. The largest velocities occur in the back-flow region of the cylinder and form the tails of the velocity histograms. Note the back-flow velocity is also referred to as the center velocity. We note that the histograms are remarkably similar in shape and show good agreement between the measured and computed velocity magnitudes. For shot 14 the center velocity is approximately 34 m/s in the experiment and 38 m/s in the simulation. This leads to a difference of 4 m/s or approximately 10% between the measured and computed center velocities. We also observe an average peak velocity magnitude of 19 m/s in the experiment and 22 m/s in the simulation. For shot 16 we observe the same center velocity of 41 m/s in both the experiment and the simulation. We also observe that the average peak velocity magnitude is 24 m/s in the experiment and 21 m/s in the simulation. The occurrence of larger velocities in the experiment can be explained by examining the measured velocity magnitude and vorticity fields shown in Figure 7.23. We observe large

velocities and small scale vortices on the bottom edge of the cylinder caused by a secondary instability. This instability does not occur in the simulation, so smaller velocities are observed in the same region of the computed velocity field. Thus the presence of a secondary instability leads to larger velocities in the experiment. Note that overall only small differences, approximately 10%- 15%, exist between the measured and computed velocity magnitudes in contrast to the large differences observed previously.

We also compare the observed center velocity in the simulation with the value predicted from the analytic vortex pair model. We measure the vortex spacing using the pressure images and compute the circulation over the defined vortex core. The predicted values are given in Table 7.6. Recall that we observed a center velocity of 38 m/s and 41 m/s in the simulations of shots 14 and 16, respectively. Therefore we achieve good agreement with the analytic predictions.

## 7.10 Experimental Initial Conditions

The diffuse profiles constructed in the previous section were based on the results of the computational study, which examined the effect of varying the initial conditions. We achieved good agreement with the measured velocities by diffusing the experimental initial conditions, which were imaged by illuminating fog particles added to the $SF_6$ gas. We know that the $SF_6$ gas diffuses faster than the fog particles used to track the gas. It was be-

lieved that this effect was not significant during the experimental time of observation. We examine how the diffusion lag between the $SF_6$ gas and the fog particles effects the imaged experimental initial conditions.

For the purpose of this investigation, planar laser Rayleigh scattering (PLRS) was implemented in the gas shock tube to obtain an accurate representation of the initial $SF_6$ gas cylinder. With this technique no fog particles are added to the $SF_6$ gas or to the surrounding air. PLRS directly images the concentration of $SF_6$ gas by illuminating the $SF_6$ and the surrounding air with large amounts of laser light. The $SF_6$ gas scatters about six times more light than the surrounding air [7]. As with our previous imaging technique, the peak concentration of $SF_6$ gas can not be determined. Future experimental analysis will include estimating the peak $SF_6$ concentration in the experimental initial conditions.

A total of ten images of the initial $SF_6$ gas cylinder were obtained using PLRS. Each image was constructed by taking the difference between the PLRS image of the $SF_6$ cylinder surrounded by air and the PLRS image of only the background air. The "Dust and Scratch" filter in Photoshop was then applied to the resulting image to remove illuminations caused by dust particles residing in the shock tube.

Figures 7.32a and 7.32b show representative images of the experimental initial conditions obtained using PLRS and the fog technique, respectively. Both images were taken on the same day with the same shock tube configuration; therefore differences in the profiles can not be attributed to different

experimental conditions. Note the PLRS image appears larger and smoother than the image obtained using the fog technique. The fog image actually appears grainy because individual fog particles are visible at this resolution. Figure 7.33 shows the concentration profiles acquired by taken a horizontal slice through the center of the $SF_6$ gas cylinder in the averaged PLRS and fog images; these images correspond to the average of the ten realizations obtained from each technique. Note that the noise in the fog concentration profile is due to the resolution of individual fog particles. Also note that the profiles correspond to pixel intensities since the peak concentration of $SF_6$ gas is unknown. We observe significant differences in the shape of the PLRS and fog profiles. The fog profile drops off suddenly, while the PLRS profile gradually decreases to 0% $SF_6$ gas. We also observe that the PLRS cylinder is approximately 4 mm larger in diameter than the fog cylinder. This helps to explain the quantitative differences observed in the height and width of the evolving cylinder in the experiment and the simulation. The PLRS images supports the computational evidence that the experimental initial conditions are actually more diffuse than imaged using the fog technique.

PLRS images were also acquired at a different height inside the test section to examine possible three-dimensional effects. The previous images were taken at 2.0 cm below the inlet nozzle; all experimental data shown in this thesis has been acquired at this height. The additional PLRS images were obtained at 3.5 cm below the inlet nozzle, which is approximately half the height of the test section. Figures 7.34a and 7.34b shows the PLRS

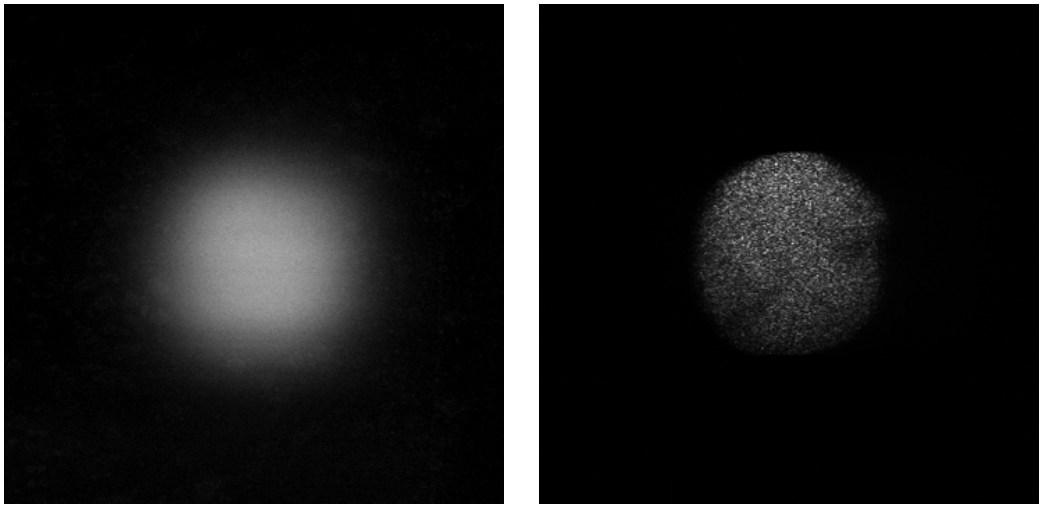

a) PLRS b) Fog

Figure 7.32: Experimental initial conditions acquired 2 centimeters below the inlet nozzle

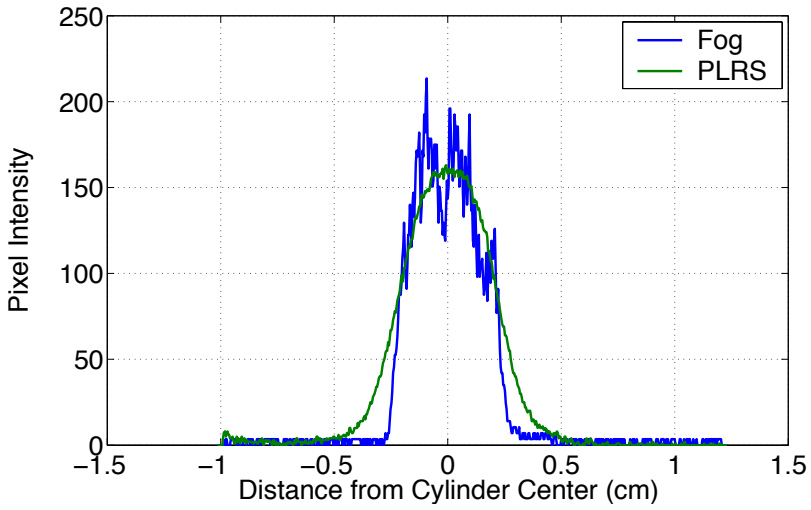


Figure 7.33: Profiles corresponding to the PLRS and fog images

and fog images acquired at this height, respectively. There is obvious differences in the cylinder size and shape compared to the images obtained at a height of 2.0 cm below the inlet nozzle. This confirms that there are also three-dimensional effects influencing the evolution of the cylinder. With the acquisition of more PLRS images at different heights, an approximate perturbation in the vertical direction can be determined. Three dimensional simulations incorporating this perturbation will be the subject of a future study.

It is of interest to compare a simulation incorporating the PLRS image with previous experimental data. Unfortunately, the flow rate of the $SF_6$ gas was increased to obtain the PLRS images. Therefore since the experimental

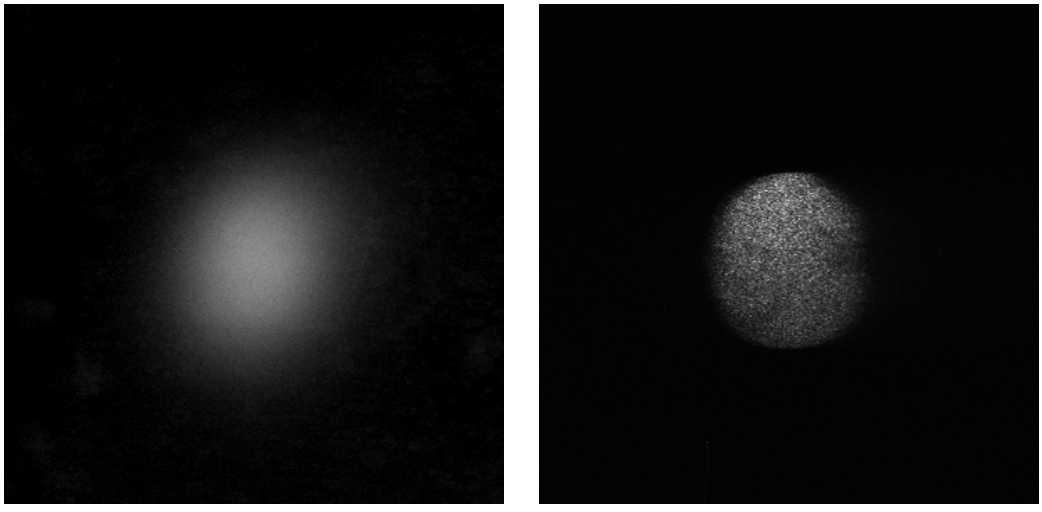

a) PLRS b) Fog

Figure 7.34: Experimental initial conditions acquired 3.5 centimeters below the inlet nozzle

conditions have changed, a comparison of previous experimental data with a simulation incorporating the PLRS image would not be meaningful. We do compare the concentration profile from the PLRS image with the computational concentration profiles constructed in the previous section. Figures 7.35 and 7.36 show the profile from the PLRS image and the profiles corresponding to the computational initial conditions in the simulations of shots 14 and 16, respectively. The PLRS profile has been scaled to match the peak $SF_6$ concentration set in the two computed profiles. The agreement between the profiles is remarkable considering that the simulations were performed prior to the acquisition of this new experimental data. The observed agreement validates the amount of diffusion applied to construct the computational initial conditions in Section 7.9.

The PLRS images confirm that the diffusion lag between the $SF_6$ gas and the fog particles effects the imaging of the experimental initial conditions. We note that adding fog particles to the flow is necessary to obtain multiple evolutionary images and velocity measurements using Particle Image Velocimetry. Therefore we need to determine a way to convert the acquired fog image into a corresponding PLRS image that accurately represents the experimental initial conditions.

Unfortunately experimental unknowns prevent us from determining an analytic expression that quantifies the experimental initial conditions. The initial $SF_6$ gas cylinder is affected by mass diffusion and the $SF_6$ jet velocity. Note the velocity in the gas curtain experiments was estimated to be on the

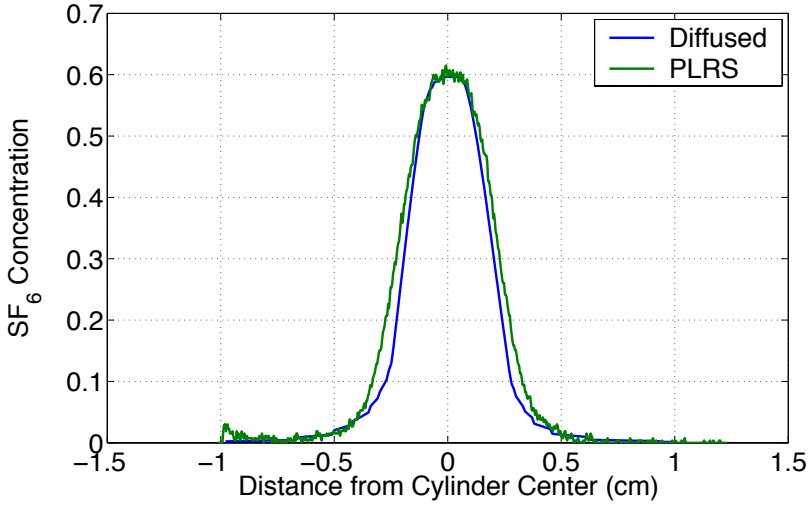


Figure 7.35: Concentration profiles corresponding to the PLRS image and the computational initial conditions for shot 14

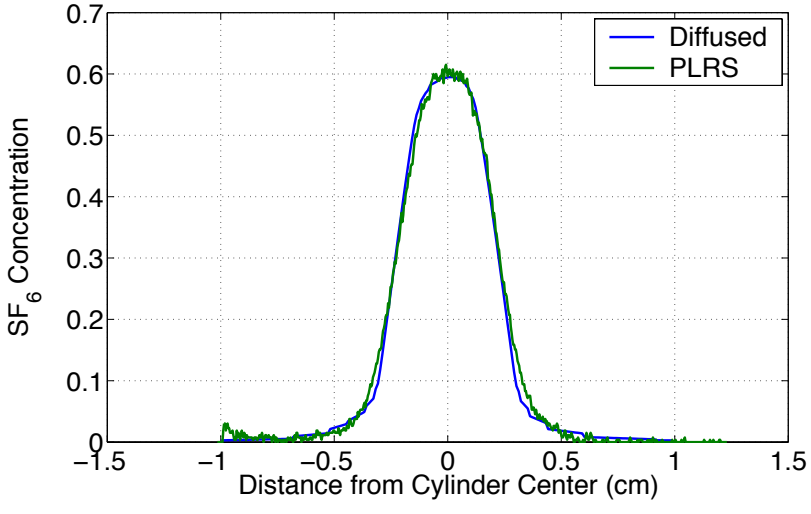


Figure 7.36: Concentration profiles corresponding to the PLRS image and the computational initial conditions for shot 16

order of 10 cm/s [47]. To model the velocity effect, we need to measure the velocity profile of the $SF_6$ gas as it enters the test section of the shock tube through the inlet nozzle. We will attempt to acquire this data once early-time PIV is possible.

We examine the effects of mass diffusion for a stationary $SF_6$ gas cylinder to show the PLRS profile can not be modelled by mass diffusion alone. The jet velocity will dampen the effect of mass diffusion, leading to a smaller than expected cylinder diameter. We use the parameters corresponding to the actual experimental conditions to construct an idealized mass diffusion profile. The radius of the inlet nozzle is approximately 0.4 cm and the $SF_6$ gas cylinder is imaged at a height of 2.0 cm below this nozzle. If we assume an initial velocity of 10 cm/s, the $SF_6$ gas cylinder will diffuse radially outward for approximately 0.2 seconds before it is imaged.

We begin by determining the diffusion constant for a binary system composed of air and $SF_6$ gas. The following expression, which is derived from the kinetic theory of gases, is used to estimate the molecular diffusivity of the air/$SF_6$ system. The expression is [51]:

$$D_{air/SF_6} = \frac{0.0018583T^{3/2}}{P(\sigma_{air/SF_6})^2\Omega_{air/SF_6}}\sqrt{\frac{1}{M_{air}} + \frac{1}{M_{SF_6}}} \tag{7.2}$$

where $D_{air/SF_6}$ is the diffusivity in $cm^2/s$, T is the temperature in degrees Kelvin, P is the pressure in atmospheres, $\sigma_{air/SF_6}$ is the Lennard-Jones force constant in Angstroms, $\Omega_{air/SF_6}$ is a "collision integral", which is dimensionless, and $M_{air}$ and $M_{SF_6}$ are the molecular weights of air and $SF_6$, respec-

| T(oK) | P (atm) | $\sigma_{air/SF_6}$ (Å) | $\Omega_{air/SF_6}$ | $M_{air}$ | $M_{SF_6}$ |
|---|---|---|---|---|---|
| 293 | 0.7921 | 4.4195 | 1.0410 | 29.0651 | 146.0504 |

Table 7.7: Values used to calculate the diffusion constant $D_{air/SF_6}$

tively. Table 7.7 shows the values of the parameters used to calculate the diffusion constant. We determine $D_{air/SF_6} = 0.1176$ cm$^2$/s. Note the local atmospheric conditions at Los Alamos were used to calculate this value.

The concentration profile resulting from the diffusion of a cylinder is examined in Crank [9]. Crank determined that for a cylinder of radius $a$ with initial concentration C defined by:

$$C = \begin{cases} C_0 & \text{for } 0 \leq r \leq a \\ 0 & \text{for } r > a \end{cases}$$

the concentration profile at radius r and time t is given by:

$$C(r,t) = \frac{C_0}{2Dt} exp\left(\frac{-r^2}{4Dt}\right) \int_0^a exp\left(\frac{-r'^2}{4Dt}\right) I_0\left(\frac{rr'}{2Dt}\right) r'dr' \qquad (7.3)$$

where D is the diffusion constant and $I_0$ is the modified Bessel function of the first kind of order zero. This expression must be evaluated numerically to determine the concentration profile. We calculate the integral using Simpson's Rule and compute the polynomial fit for $I_0$ using the algorithm given in "Numerical Recipe's in C" [38].

We determine the idealized diffusion profile by setting the initial radius of the $SF_6$ gas cylinder to 0.4 cm and then allowing the cylinder to diffuse

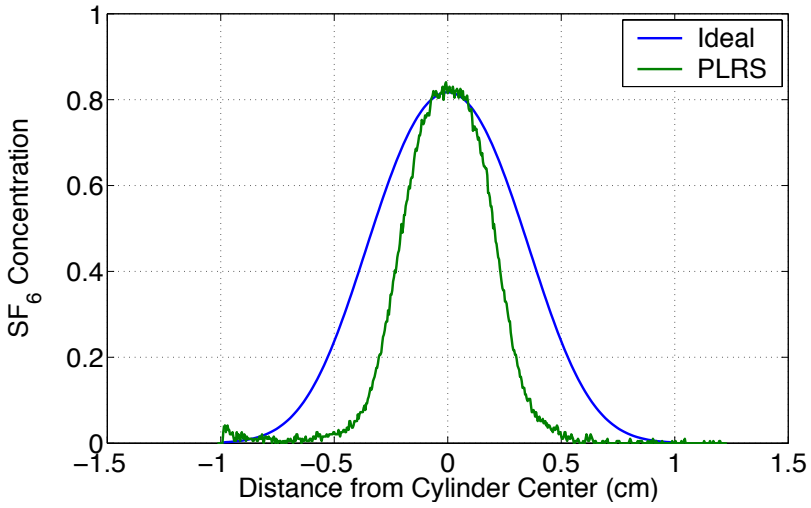


Figure 7.37: Comparison the PLRS profile with the idealized diffusion profile

for 0.2 seconds. Figure 7.37 shows the resulting diffusion profile along with the measured PLRS profile. The PLRS profile has been scaled to match the peak concentration observed in the idealized diffusion profile. Note that the idealized profile has a radius of approximately 0.8 cm, compared to 0.5 cm observed in the PLRS profile. In order to match the PLRS profile, we must diffuse a cylinder of radius 0.25 cm for 0.05 seconds. Note these values are inconsistent with the experimental conditions. Therefore the effect of mass diffusion does not independently explain the resulting PLRS profile. We need to experimentally measure the velocity distribution of the $SF_6$ gas in order to determine an analytic expression that accurately quantifies the experimental initial conditions.

# Chapter 8

# Conclusion

In this thesis we presented an experimental and computational study of the evolution of an $SF_6$ gas cylinder surrounded by air when accelerated by a planar Mach 1.2 shock wave. This thesis was the first code validation study of a shocked flow to use two-dimensional velocity field data for comparison. We showed that RAGE simulations incorporating the two-dimensional image of the experimental initial conditions led to good qualitative agreement with the experimental concentration images. Comparing length measurements of the evolving cylinder and velocity vectors at the last experimental time led to quantitative differences, particularly between the measured and the computed velocity magnitudes.

We performed a computational study which examined the effect of varying the peak concentration of $SF_6$ gas and the air/$SF_6$ gradient in the experimental initial conditions. We concluded that the differences observed

between the measured and computed velocity magnitudes were the result of an inaccurate characterization of the experimental initial conditions. Quantitative agreement with experimental velocity measurements was achieved by setting the peak $SF_6$ concentration to 60% and diffusing the experimental initial conditions to match the dimensions of the first experimental concentration image observed at 50 $\mu$s after shock passage.

Images of the initial $SF_6$ cylinder acquired using planar laser Rayleigh scattering (PLRS) support this claim. The data showed that the diffusion lag between the $SF_6$ gas and the fog particles used to track the gas effects the imaging of the experimental initial conditions. The initial $SF_6$ gas cylinder is actually more diffuse than imaged using the fog particles. Remarkable agreement was also observed between the concentration profiles from the PLRS image and from the computationally modified experimental initial conditions. This validates the diffused initial conditions used in the simulations that led to good quantitative agreement between the measured and computed velocity magnitudes.

The computational and experimental studies performed in this thesis played a major role in improving and understanding the RAGE code and the shock tube experiments. This has led to increased confidence in both the computations and the experiments.

# Bibliography


[1] AEA Technology, Oxfordshire, UK. *VISIFLOW System User Manual*, 1997.

[2] R. M. Baltrusaitis, M. L. Gittings, R. P. Weaver, R. F. Benjamin, and J. M. Budzinski. Simulation of shock-generated instabilities. *Phys. Fluids*, 8(9):2471–2483, September 1996.

[3] R. F. Benjamin. Experimental observations of shock stability and shock-induced turbulence. In *Proceedings of the First International Workshop on the Physics of Compressible Turbulent Mixing*, Princton, NJ, 1988. Also in Lawrence Livermore Laboratory Report CONF-8810234, Jan. 1992.

[4] D. Besnard, F. H. Harlow, R. M. Rauenzahn, and C. Zemach. Turbulence transport equations for variable-density turbulence and their relationship to two-field models. La-12303-ms, Los Alamos National Laboratory, 1992.

[5] D. Besnard, G. Jourdan, E. Valerio, and D. Zeitoun. Shock wave induced mixing: experimental results and numerical modeling. In *Proceedings of the 21st International Symposium on Shock Waves*, pages 1–6, Great Keppel Island, Australia, 1997.

[6] J. M. Budzinski. *Planar Rayleigh Scattering Measurements of Shock Enhanced Mixing*. PhD thesis, California Institute of Technology, 1992.

[7] J. M. Budzinski, R. F. Benjamin, and J. W. Jacobs. Influence of initial conditions on the flow patterns of a shock-accelerated thin fluid layer. *Phys. Fluids*, 6(11):3510–3512, November 1994.

[8] A. Burrows, J. Hayes, and B. A. Fryxell. On the nature of core-collapse supernova explosions. *Astrophys. J.*, 450:830–850, September 1995.

[9] J. Crank. *The Mathematics of Diffusion.* Oxford University Press, New York, 2nd edition, 1975.

[10] G. Dimonte, C. E. Frerking, M. Schneider, and B. Remington. Richtymer-Meshkov instability with strong radiatively driven shocks. *Phys. Plasmas*, 3(2):614–630, February 1996.

[11] G. Dimonte and M. Schneider. Turbulent Richtmyer-Meshkov instability experiments with strong radiatively driven shocks. *Phys. Plasmas*, 4(12):4347–4357, December 1997.

[12] M. Farge. Wavelet transforms and their applications to turbulence. *Annu. Rev. Fluid Mech.*, 24:395–457, 1992.

[13] B. Fryxell, E. Müller, and D. Arnett. Hydrodynamics and nuclear burning. Rep. no. 449, Max-Plank-Institut für Astrophysik, 1989.

[14] M. L. Gittings. SAIC's adaptive grid Eulerian hydrocode. In *Defense Nuclear Agency Numerical Methods Symposium*, 1992.

[15] J. Glimm, M. J. Graham, X. L. Li, J. Grove, T. M. Smith, D. Tan, F. Tangerman, and Q. Zhang. Front tracking in two and three dimensions. *Computers Math. Applic.*, 35(7):1–11, April 1998.

[16] J. W. Grove. Applications of front tracking to the simulation of shock refractions and unstable mixing. *Appl. Num. Math.*, 14(1-3):213–237, April 1994.

[17] J. W. Grove, R. Holmes, D. H. Sharp, Y. Yang, and Q. Zhang. Quantitative theory of Richtmyer-Meshkov instability. *Phys. Rev. Lett.*, 71(21):3473–3476, November 1993.

[18] J. F. Haas and B. Sturtevant. Interaction of weak shock waves with cylindrical and spherical gas inhomogeneities. *J. Fluid Mech.*, 181:41–76, 1987.

[19] J. F. Hawley and N. J. Zabusky. Vortex paradigm for shock-accelerated density-stratified interfaces. *Phys. Rev. Lett.*, 63(12):1241–1244, 1989.

[20] R. L. Holmes, G. Dimonte, B. Fryxell, M. L. Gittings, J. W. Grove, M. Schneider, D. H. Sharp, A. L. Velikovich, R. P. Weaver, and Q. Zhang. Richtmyer-Meshkov instability growth: experiment, simulation and theory. *J. Fluid Mech.*, 389:55–79, June 1999.

[21] J. W. Jacobs. The dynamics of shock accelerated light and heavy gas cylinders. *Phys. Fluids A*, 5(9):2239–2247, September 1993.

[22] J. W. Jacobs, D. G. Jenkins, D. L. Klein, and R. F. Benjamin. Nonlinear growth of the shock-accelerated instability of a thin fluid layer. *J. Fluid Mech.*, 295:23–42, 1995.

[23] J. W. Jacobs, D. L. Klein, D. G. Jenkins, and R. F. Benjamin. Instability growth-patterns of a shock-accelerated thin fluid layer. *Phys. Rev. Lett.*, 70(5):583–586, February 1993.

[24] B. Jun, T. W. Jones, and M. L. Norman. Interaction of Rayleigh-Taylor fingers and circumstellar cloudlets in young supernova remnants. *Astrophys. J.*, 468:L59–L63, September 1996.

[25] J. Kane, R. P. Drake, and B. A. Remington. An evaluation of the Richtymer-Meshkov instability in supernova remnant formation. *Astrophys. J.*, 511:335–340, January 1999.

[26] L. A. Marschall. *The Supernova Story.* Plenum Press, New York, 1988.

[27] E. E. Meshkov. Instability of the interface of two gases accelerated by a shock wave. *Izv. AN SSR. Mekhanika Zhidkosti i Gasa*, 4(5):151–157, 1969.

[28] C. Mügler and S. Gauthier. Two-dimensional Naiver-Stokes simulations of gaseous mixtures induced by Richtmyer-Meshkov instability. *Phys. Fluids*, 12(7):1783–1798, July 2000.

[29] S. Nakai and H. Takabe. Principles of inertial confinement fusion: Physics of implosion and the concept of inertial fusion energy. *Rep. Prog. Phys*, 59(9):1071–1131, 1996.

[30] Y. Nakamura, A. Leonard, and P. R. Spalart. Vortex simulation of an invscid sheer layer. In *Proceedings of the AIAA/ASME 3rd Joint Thermophsyics, Fluids and Heat Transfer Conference*, 1982.

[31] National Center for Supercomputing Applications, University of Illinois at Urbana-Champaign. *HDF Users Guide*, February 1996. Version 4.0.

[32] J. M. Pasachoff. *Comtemporary Astronomy.* W. B. Saunders Co., Philadelphia, 1977.

[33] J. M. Picone and J. P. Boris. Vorticity generation by asymmetric energy deposition in a gaseous medium. *Phys. Fluids*, 26(2):365–382, February 1983.

[34] J. M. Picone and J. P. Boris. Vorticity generation by shock propagation through bubbles in a gas. *J. Fluid Mech.*, 189:23–51, 1988.

[35] J. M. Picone, E. S. Oran, J. P. Boris, and T. R. Young Jr. Theory of vorticity generation by shock wave and flame interactions. In *Dynamics of Shock Waves, Explosions, and Detonations*, pages 429–448, New York, 1984. American Institute of Aeronautics and Astronautics, Inc.

[36] F. Poggi, M. Thorembey, and G. Rodriguez. Velocity measurements in turbulent gaseous mixtures induced by Richtmyer-Meshkov instability. *Phys. Fluids*, 10(11):2698–2700, November 1998.

[37] L. Prandtl and O. G. Tietjens. *Fundamentals of Hydro- and Aeromechanics.* McGraw-Hill Book Company, Inc., New York, 1934.

[38] W. H. Press, S. A. Teukolsky, W. T. Vetterling, and B. P. Flannery. *Numerical Recipes in C: The Art of Scientific Computing.* Cambridge University Press, New York, 2nd edition, 1992. Reprinted 1999.

[39] K. Prestridge, P. M. Rightley, P. Vorobieff, R. F. Benjamin, and N. A. Kurnit. Simultaneous density-field visualization and PIV of a shock-accelerated gas curtain. *Exp. in Fluids*, 29(4):339–346, October 2000.

[40] K. Prestridge, P. Vorobieff, P. M. Rightley, and R. F. Benjamin. Validation of an instability growth model using particle image velocimetry measurements. *Phys. Rev. Lett.*, 84(19):4353–4356, May 2000.

[41] J. J. Quirk and S. Karni. On the dynamics of a shock-bubble interaction. *J. Fluid Mech.*, 318:129–163, July 1996.

[42] M. Raffel, C. E. Willert, and J. Kompenhans. *Particle Image Velocimetry: A Pratical Guide.* Springer-Verlag, 1998.

[43] Lord Rayleigh. Investigation of the character of the equilibrium of an incompressible heavy fluid of varible density. *Proc. Lond. Math Soc.*, 14:170–177, 1883. Reprinted in The Scientific Papers of Lord Rayleigh, vol. II, Cambridge University Press, Cambridge, England 1900.

[44] B. A. Remington, J. Kane, R. P. Drake, S. G. Glendinning, K. Estabrook, R. London, J. Castor, R. J. Wallace, D. Arnett, E. Liang, R. McCray, A. Rubenchik, and B. Fryxell. Supernova hydrodymanics experiments on the Nova laser. *Phys. Plasmas*, 4(5/pt.2):1994–2003, May 1997.

[45] R. D. Richtmyer. Taylor instability in shock acceleration of compressible fluids. *Comm. Pure Appl. Math.*, 13:297–319, 1960.

[46] P. M. Rightley, P. Vorobieff, and R. F. Benjamin. Evolution of a shock-accelerated thin fluid layer. *Phys. Fluids*, 9(6):1770–1782, June 1997.

[47] P. M. Rightley, P. Vorobieff, R. Martin, and R. F. Benjamin. Experimental observations of the mixing transition in a shock-accelerated gas curtain. *Phys. Fluids*, 11(1):186–200, January 1999.

[48] G. Rudinger and L. M. Somers. Behaviour of small regions of different gases carrried in accelerated gas flows. *J. Fluid Mech.*, 7:161–176, 1960.

[49] R. Samtaney and N. J. Zabusky. Circulation deposition on shock-accelerated planar and curved density-stratified interfaces: models and scaling laws. *J. Fluid Mech.*, 269:45–78, June 1994.

[50] D. H. Sharp. An overview of Rayleigh-Taylor instability. *Physica D*, 12:3–18, 1984.

[51] A. H. P. Skelland. *Diffusional Mass Transfer*. John Wiley & Sons, Inc., New York, 1974.

[52] J. A. Smith, D. Coles, A. Roshko, and A. J. Prasad. A description of the GALCIT 6-inch shock tube. Galcit report fm-67-1, California Institute of Technology, 1967.

[53] M. J. Steinkamp, M. L. Gittings, R. P. Weaver, and F. H. Harlow. Implementation of a mix model into RAGE. Technical Report LA-UR-01-0572, Los Alamos National Laboratory, 2001.

[54] J. M. Stone, J. Xu, and L. G. Mundy. Formation of 'bullets' by hydrodynamical instabilities in stellar outflows. *Nature*, 377, September 1995.

[55] G. I. Taylor. The instability of liquid surfaces when accelerated in a direction perpendicular to their planes. *Proc. R Soc. London A*, 201:192–196, 1950.

[56] E. Valerio, G. Jourdan, L. Houas, and D. Zeitoun. Modeling of Richtmyer-Meshkov instability-induced turbulent mixing in shock-tube experiments. *Phys. Fluids*, 11(1):214–225, 1999.

[57] P. Vorobieff, P. M. Rightley, and R. F. Benjmain. Power-law spectra of incipient gas-curtain turbulence. *Phys. Rev. Lett.*, 81(11):2240–2243, September 1998.

[58] R. P. Weaver, M. L. Gittings, and M. R. Clover. The parallel implementation of RAGE: a 3D continuous adaptive mesh refinement shock code. In Imperial College, editor, *Proceedings of the 22nd International Symposium on Shock Waves*, pages 671–676, London, UK, 1999.

[59] Y. Yang, Q. Zhang, and D. H. Sharp. Small amplitude theory of Richtmyer-Meshkov instability. *Phys. Fluids*, 6(5):1856–1873, May 1994.

[60] N. J. Zabusky and S. Zhang. Shock-planar curtain interactions in two dimensions: Emergence of vortex double layers, vortex projectiles, and decaying stratified turbulence. *Phys. Fluids*, 14(1):419–422, January 2002.

[61] Q. Zhang and S. Sohn. Nonlinear theory of unstable fluid mixing driven by shock wave. *Phys. Fluids*, 9(4):1106–1124, April 1997.


Los Alamos NM 87545